Quantum Effects in a One-Dimensional Magnetic Gravitational Trap for Ultracold Neutrons

A. I. Frank[1], * and V. G. Nosov[2]

[1] Frank Laboratory of Neutron Physics, Joint Institute for Nuclear Research, Dubna, Moscow region, 141980 Russia
* e-mail: frank@nf.jinr.ru
[2] Russian Research Centre Kurchatov Institute, pl. Akademika Kurchatova 1, Moscow, 123182 Russia
Received February 24, 2004

The problem of storing ultracold neutrons over a plane magnetic mirror in the presence of gravity is considered. For neutrons with a definite polarization, the sum of the magnetic and gravitational potentials can have a minimum and, hence, form a magnetic gravitational trap. For low energies of vertical motion, the neutron state in this well is quantized. The possibility of accomplishing the corresponding quantum gravitational experiment is analyzed. © 2004 MAIK "Nauka/Interperiodica".

PACS numbers: 03.75.Be

Ultracold neutrons and a quantum gravitational experiment. Shortly after the discovery of ultracold neutrons (UCNs), it has become possible to operate with neutrons whose energies are so low that the quantum effects become significant even in the interaction of UCNs with macroscopic objects. In particular, it was illustrated in [1], where the problem of storing UCNs on a horizontal mirror in the presence of the gravitational force was considered. The classical analysis of this problem is, obviously, correct only if $E_z \gg \hbar\omega_r$, where E_z is the energy of vertical motion and ω_r is the cyclic frequency of neutron reflections from the mirror. For low energies, this condition is not satisfied and the quantum approach is necessary.

The potential in the corresponding quantum problem has the shape of a triangular well bounded by the effective mirror potential $U_{ef} > E$ at $z < 0$ and by the gravitational potential $V_g = mgz$ at $z > 0$. The energy of vertical motion is quantized, and the spatial distribution of neutrons is determined by the Airy-type wave functions. The solution is characterized by the energy $\varepsilon_g \approx 0.6 \times 10^{-12}$ eV and length $l_g \approx 5.9 \times 10^{-4}$ cm constants. The energy quantization for UCNs stored on a plane was observed experimentally in [2].

Since the main parameters of the problem are determined by the gravitational acceleration, one can believe that the measurement of this effect can be quite suitable for studying the gravitational interaction of a neutron. In particular, Abele and Westphal [3] obtained an upper estimate for the hypothetical gravitational-like interaction between a neutron and a mirror, which was obtained from the comparison of experimental data [2] with theory.

In this paper, we discuss one more possibility of observing neutron quantum states in the gravitational field of the Earth.

UCN magnetic gravitational trap. Our proposal is that the Vladimirskiĭ magnetic mirror [4] can be used instead of a material mirror. Let the mirror magnetic system be placed in the $Z = 0$ plane and present a set of strip alternating currents flowing along the Y axis with spatial period d. It is known that, even at comparatively small distances from the conductors, magnetic field has the form [4]

$$B_z = B_m e^{-\gamma z}\cos(\gamma x), \quad e^{-2\gamma z} \ll 1, \quad z > 0, \qquad (1)$$
$$B_x = B_m e^{-\gamma z}\sin(\gamma x),$$

where $\gamma = 2\pi/d$. Such a field could be created over the entire half-space $z > 0$ by a current flowing in the $z = 0$ plane with the density distribution $j = (c/2\pi)B_m\sin(\gamma x)$.

If the neutron motion in a magnetic field is adiabatically slow [4], the spin vector remains parallel or antiparallel to the field. Therefore, the magnetic interaction potential of neutron has the form
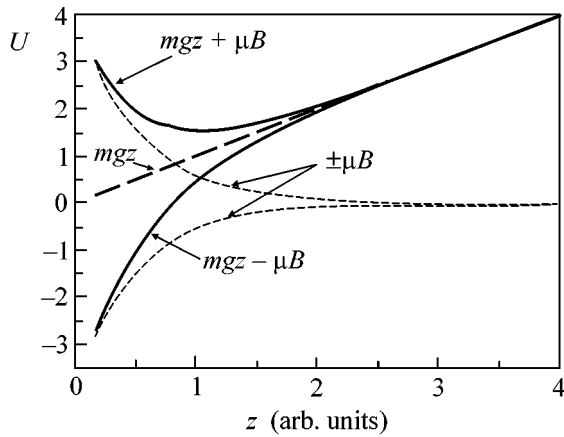
$$u_m = \pm\mu|B|, \quad |B(z)| = B_m e^{-\gamma z}, \qquad (2)$$

where μ is the neutron magnetic moment. With allowance for the gravitational force, the total potential is

$$U(z) = \pm\mu B_m e^{-\gamma z} + mgz. \qquad (3)$$

For one of the spin components, this potential has a minimum and forms a potential well (Fig. 1). At the minimum point, we have

$$u_m = +\mu|B|, \quad \gamma\mu B_m e^{-\gamma z} = mg \quad (z > 0), \qquad (4)$$

Fig. 1. Potential over the magnetic mirror for two spin components.

Fig. 2. Square of the absolute value of wave function for several lower states in a trap.

and the total force is zero. Equality (4) is the condition for the "magnetic suspender" at the point $z = L > 0$. Equation (4) can be rewritten as

$$\gamma = mg/\mu B_0, \tag{5}$$

where $B_0 = B_m e^{-\gamma L}$ is the field magnitude in the equilibrium plane $z = L$.

The presence of a potential well implies that a neutron with a sufficiently low vertical velocity can be trapped in it and oscillate near the equilibrium plane. For small values of the variable

$$\eta = z - L, \tag{6}$$

we obtain

$$U \approx mgL + \mu B_0 + \frac{1}{2}\mu B_0 \gamma^2 \eta^2 \tag{7}$$

to the second-order terms inclusively. The variable part of the potential

$$u(\eta) = \frac{1}{2}\mu B_0 \gamma^2 \eta^2 = C\eta^2 \tag{8}$$

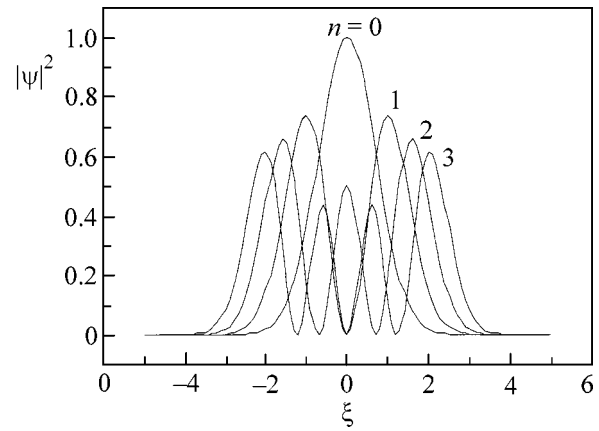determines the elastic constant C of the corresponding oscillator

$$C = \frac{m^2 g^2}{\mu B_0}. \tag{9}$$

The oscillation frequency near the equilibrium point is given by the formula

$$\omega = \sqrt{\frac{C}{m}} = \sqrt{\frac{mg^2}{\mu B_0}}, \tag{10}$$

and the amplitude η_0 is determined by the energy E_z of vertical motion:

$$E_z = \frac{1}{2}C\eta_0^2, \quad \eta_0 = \frac{1}{mg}\sqrt{2\mu B_0 E_z}. \tag{11}$$

The harmonic approximation adopted in these expressions is valid under the condition

$$\eta_0 \ll \gamma^{-1} \text{ or } E_z \ll \mu B_0. \tag{12}$$

The classical description of motion is valid if

$$E_z \gg \hbar\omega = \varepsilon, \quad \varepsilon = \hbar\sqrt{\frac{mg^2}{\mu B_0}}. \tag{13}$$

For lower neutron energies, the quantum description is necessary, and the problem reduces to the well-known problem of a linear oscillator (see, e.g., [5]). The energy spectrum and wave functions have the form

$$E_n = \left(n + \frac{1}{2}\right)\varepsilon, \tag{14}$$

$$\psi_n(\eta) = \left(\frac{m\omega}{\pi\hbar}\right)^{1/4}\frac{1}{\sqrt{2^n n!}}e^{-\frac{m\omega}{2\hbar}\eta^2}H_n\left(\eta\sqrt{\frac{m\omega}{\hbar}}\right), \tag{15}$$

respectively, where H_n are Hermitian polynomials.

Figure 2 shows the neutron spatial distributions near the equilibrium plane, as calculated by formula (15) for the first five levels ($n = 0$–4). The integral distribution obtained by summing up the densities from $n = 0$ to $n = N$ ($N = 3$–7) is shown in Fig. 3. The horizontal axis is the dimensionless coordinate $\xi = \kappa\eta$, where $\kappa = \sqrt{m\omega/\hbar}$.

Numerical estimates and possible realizations. All parameters of the problem are not fixed and depend strongly on the magnitude and geometry of a magnetic field. This is the main distinction from the case of UCN storage on the plane, where the effective potential is *a priori* specified. Let us take the magnetic-field magnitude B_0 as the parameter of the problem. The exponential decrease of the field and the equality of the magnetic and gravitational forces determine the exponent γ

given by Eq. (5). Thus, the potential shape proves to be determined.

Let us make some estimates. Let the magnetic field $B_0 = 0.5$ G, which corresponds to $\gamma^{-1} = 3 \times 10^{-3}$ cm. To create field with such damping, a current structure with a period of 0.2 mm is required. In this case, the frequency is $\omega = 576$ s^{-1}, which corresponds to the characteristic energy $\varepsilon \approx 3.8 \times 10^{-13}$ eV. This energy is lower than the magnetic energy $\mu B_0 = 3 \times 10^{-12}$ eV by an order of magnitude, so that the harmonicity condition is well fulfilled for lower levels. In order for the width of levels to be much less than the distance between them, the neutron residence time in the system must be $t \gg \hbar/\varepsilon$. For the longitudinal neutron velocity $V \approx 5$ m/s, typical for UCNs, this relation is valid for a mirror length of several centimeters. The spectrum of states is given by Eq. (14), and the constant $\kappa \approx 9.6 \times 10^2$ cm^{-1} determines the scale of spatial distribution. The distribution is given by Eq. (15), and the scale unit in Figs. 2 and 3 corresponds to $\kappa^{-1} = 10$ μm.

Finally, the distance L from the magnetic mirror to the equilibrium point can be chosen arbitrarily. As is seen in Fig. 3, the first ten states are localized in the region ±50 μm from the equilibrium plane. Taking $L = 100$ μm ($L\gamma \approx 3.3$), we find from Eq. (5) that the magnetic field on the mirror surface must be on the order of 15 G. The experimental parameters presented above are quite realistic.

Knowing $L\gamma$, one can estimate the accuracy of Eq. (1) for field distribution. If the sign of strip current reverses after a half of the period, the contribution from the higher harmonics to the magnitude of magnetic field with the aforementioned mirror parameters will be about 1%.

A neutron moving along the Y axis near the equilibrium plane is in a constant uniform magnetic field. For the other velocity direction, the neutron passes through regions with different field directions. Thus, in the neutron-fixed coordinate system, there is a magnetic field that rotates with frequency $\Omega = 2\pi V_x/d$, where V_x is the velocity X component. Therefore, the condition for the adiabatically slow motion [4] is formulated as

$$\omega_L \gg \Omega, \quad \omega_L = \frac{2\mu B_0}{\hbar}, \quad \Omega = \frac{2\pi V \sin\theta}{d}, \quad (16)$$

where ω_L is the Larmor frequency and θ is the angle between the velocity and the Y axis.

For the velocity $V = 5$ m/s, typical of UCNs, and the chosen B_0 value, condition (15) requires a quite good beam collimation $\theta \ll 0.05$. We note that the ratio ω_L/Ω is proportional to B_0^2, because the structure period $d = 2\pi/\lambda$ is proportional to B_0 according to Eq. (5).

The possibility of observing the quantum properties of the magnetic gravitational trap was demonstrated in [2], where the spatial distribution of neutrons stored on a material mirror was measured. The possibility of
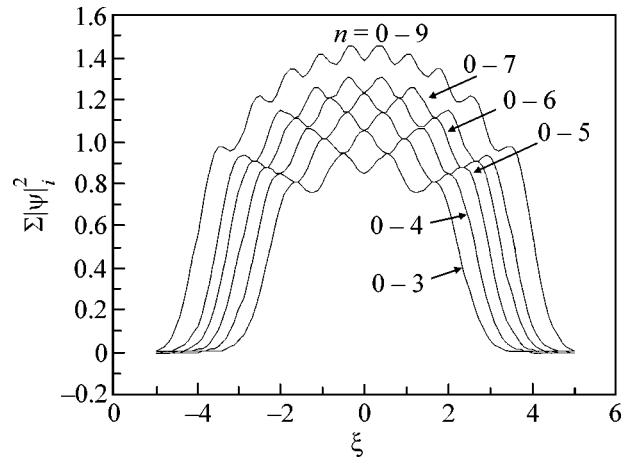

Fig. 3. Total neutron-density distribution on several lower levels.

observing the transitions between levels in an alternating magnetic field also seems to be promising.

In conclusion, we note that the illumination conditions in the experiment on the observation of gravitational levels in the magnetic gravitational trap are worse than those in the experiment discussed in [1, 2], which is caused both by a lower energy of the state and by the requirements on the beam collimation. However, this disadvantage is completely compensated by a much higher sensitivity of the spatial position of a trapped neutron to the gravitational acceleration. This sensitivity is due to the fact that the characteristic length constant $l_{gm} = \gamma^{-1}$ is inversely proportional to g, whereas $l_g \propto g^{-1/3}$ [1]. Moreover, the length constant l_{gm} [μm] $= 60 \times B_0$ [G] is much larger than l_g.

REFERENCES

1. V. I. Lushchikov and A. I. Frank, Pis'ma Zh. Éksp. Teor. Fiz. **28**, 607 (1978) [JETP Lett. **28**, 559 (1978)].

2. V. V. Nesvizhevsky, H. Börner, A. K. Petukhov, *et al.*, Nature **145**, 297 (2002); V. V. Nesvizhevsky, H. Börner, A. M. Gagarski, *et al.*, Phys. Rev. D **67**, 102002 (2003).

3. H. Abele and A. Westphal, ILL Annual Report (2002), p. 76, http://www.ill.fr/AR-02/site/areport/fset 73.htm; H. Abele, S. Baessler, and A. Wetphal, Lect. Notes Phys. **631**, 355 (2003).

4. V. V. Vladimirskiĭ, Zh. Éksp. Teor. Fiz. **39**, 1062 (1960) [Sov. Phys. JETP **12**, 740 (1960)].

5. L. D. Landau and E. M. Lifshits, *Quantum Mechanics: Non-Relativistic Theory* (Pergamon, Oxford).

Translated by R. Tyapaev

Wavelet Transform Analysis of the Chaotic Synchronization of Dynamical Systems

A. A. Koronovskiĭ and A. E. Hramov*

Saratov State University, Ural State Scientific Center Kolledzh, ul. Astrakhanskaya 83, Saratov, 410012 Russia
* e-mail: aeh@cas.ssu.runnet.ru

A new method for analyzing chaotic synchronization is proposed. It is based on the introduction of the family of phases for a chaotic signal using a continuous wavelet transform. The method is used to study the synchronization of two chaotic dynamical systems with ill-defined phases. © 2004 MAIK "Nauka/Interperiodica".

PACS numbers: 05.45.Xt; 02.30.Uu

Phase synchronization [1, 2] of systems in the chaotic dynamical regime is one of the most important phenomena in the modern theory of nonlinear oscillations. Phase synchronization was experimentally observed for radio generators [3], lasers [4], electrochemical oscillators [5], heart rate [6], gas discharge [7], etc. (see also reviews [2, 8, 9]). It is quite important to study the chaotic synchronization in the information transmission by the deterministic chaotic oscillations [10].

When describing and analyzing phase synchronization, one usually introduces the phase $\phi(t)$ of a chaotic signal [1, 2, 8, 9]. Phase synchronization means that the phases of chaotic signals are locked, whereas their amplitudes remain uncorrelated and chaotic. Phase locking leads to the coincidence of the signal frequencies. The frequency of a chaotic signal is defined as the average rate of phase variation $\langle \dot{\phi}(t) \rangle$.

At present, no universal method of introduction of the phase of chaotic signal exists that would be suitable for any dynamical systems. There are several methods of phase introduction that are suited to "good" systems with a simple topology of chaotic attractor. First, the phase $\phi(t)$ of a chaotic signal is introduced as the angle in the polar coordinate system on the (x, y) plane [11]:

$$\phi(t) = \arctan\frac{y(t)}{x(t)}. \tag{1}$$

In this case, all trajectories of the projection of chaotic attractor on the (x, y) plane must rotate about the origin of coordinates.

Second, to define the phase for a chaotic dynamical system, the analytical signal [1, 8]

$$\zeta(t) = x(t) + j\tilde{x}(t) = A(t)e^{j\phi(t)} \tag{2}$$

is introduced, where the function $\tilde{x}(t)$ is the Hilbert transform of the time realization $x(t)$:

$$\tilde{x}(t) = \frac{1}{\pi} \int_{-\infty}^{+\infty} \frac{x(\tau)}{t - \tau} d\tau. \tag{3}$$

Correspondingly, the phase $\phi(t)$ of chaotic signal $x(t)$ is determined from Eqs. (2) and (3).

Third, to define the phase of a chaotic signal, the surface of the Poincaré section [1, 2, 8] is used, and the phase is defined as

$$\phi(t) = 2\pi\frac{t - t_n}{t_{n+1} - t_n} + 2\pi n, \quad t_n \le t \le t_{n+1}, \tag{4}$$

where t_n is the time corresponding to the nth intersection of the phase trajectory and the surface of Poincaré section.

All these approaches give similar results for good systems [1, 2, 8, 9]. At the same time, they give contradictory results for systems with ill-defined phase (see, e.g., [2, 12, 13]). The traditional methods, as a rule, fail to reveal the presence of phase synchronization. For this reason, phase synchronization in such systems can be revealed by indirect measurements [12], in particular, by the calculation of Lyapunov exponents [2, 8, 14].

In this work, we consider a new method of revealing phase synchronization in dynamical systems with ill-defined phase. The behavior of such systems can be characterized by a continuous phase set defined on the basis of the following continuous wavelet transform [15] of the chaotic signal $x(t)$:

$$W(s, t_0) = \int_{-\infty}^{+\infty} x(t)\psi_{s, t_0}^*(t)dt, \tag{5}$$

where the asterisk means the complex conjugation and

$$\psi_{s, t_0}(t) = \frac{1}{\sqrt{s}} \psi_0\left(\frac{t - t_0}{s}\right) \qquad (6)$$

is the wavelet function obtained from the mother wavelet $\psi_{s, t_0}(t)$. The time scale s determines the width of the wavelet $\psi_0(t)$, where t_0 is the time shift of the wavelet function. We note that the notion of the time scale is used in the wavelet analysis instead of the notion of frequency in the Fourier analysis.

As the mother wavelet, we use the Morlet wavelet [15, 16]

$$\psi_0(\eta) = \frac{1}{\sqrt[4]{\pi}} \exp(j\omega_0\eta) \exp(-\eta^2/2). \qquad (7)$$

The wavelet parameter $\omega_0 = 2\pi$ ensures the relation $s \simeq 1/f$ between the time scale s and frequency f of the Fourier transform.

The wavelet surface

$$W(s, t_0) = |W(s, t_0)| e^{j\phi_s(t_0)} \qquad (8)$$

characterizes the behavior of the system for every time scale s at any time t_0. The quantity $|W(s, t_0)|$ characterizes the presence and the intensity of the corresponding time scale s at time t_0. It is also convenient to introduce the integral energy distribution over the time scales in the wavelet spectrum:

$$E(s) = \int |W(s, t_0)|^2 dt_0. \qquad (9)$$

The phase $\phi_s(t) = \arg W(s, t)$ also proves to be naturally defined for every time scale s. In other words, the behavior of each time scale s can be characterized using the associated phase $\phi_s(t)$.

Let us consider the behavior of two different coupled chaotic oscillators. If these oscillators are not in the phase-synchronization regime, their behaviors are asynchronous on all time scales s. As soon as the dynamical systems under consideration are synchronized on some time scales (e.g., upon an increase in the coupling parameter between the systems), the phase-synchronization regime arises. The time scales accounting for the greatest fraction of the wavelet-spectrum energy $E(s)$ are, obviously, synchronized first. The other time scales remain unsynchronized. In this case, phase synchronization leads to phase locking on the synchronized time scales s:

$$|\phi_{s1}(t) - \phi_{s2}(t)| < \text{const.} \qquad (10)$$

Here, $\phi_{s1, 2}(t)$ are the continuous phases of the first and second oscillators, respectively, corresponding to the synchronized time scales s.

The approach based on the continuous wavelet transform can successfully be applied to any dynamical systems, including systems with ill-defined phase. As
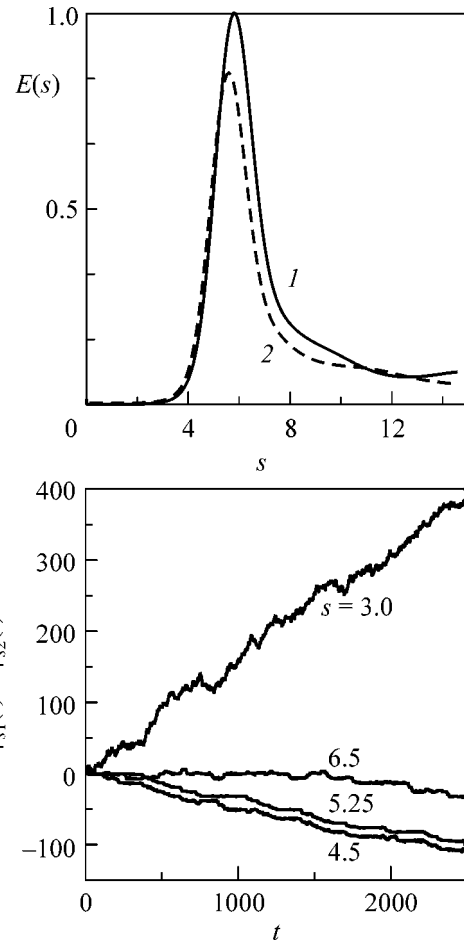

Fig. 1. Normalized energy spectrum $E(s)$ of the wavelet transform for the (*1*) first and (*2*) second Rössler systems, and the phase difference $\phi_{s1}(t) - \phi_{s2}(t)$ between two coupled Rössler systems with the coupling parameter $\varepsilon = 0.025$. The synchronization regime is absent.

an example, we consider the behavior of two different coupled Rössler systems [17] in the spiral-chaos regime:

$$\dot{x}_{1, 2} = -\omega_{1, 2} y_{1, 2} - z_{1, 2} + \varepsilon(x_{2, 1} - x_{1, 2}),$$

$$\dot{y}_{1, 2} = \omega_{1, 2} x_{1, 2} + a y_{1, 2} + \varepsilon(y_{2, 1} - y_{1, 2}), \qquad (11)$$

$$\dot{z}_{1, 2} = p + z_{1, 2}(x_{1, 2} - c),$$

where ε is the coupling parameter, $\omega_1 = 0.98$, $\omega_2 = 1.03$, $a = 0.22$, $p = 0.1$, and $c = 8.5$.

Figure 1 illustrates the behavior of two coupled Rössler systems for a small coupling parameter $\varepsilon = 0.025$. The energy spectra $E(s)$ of the wavelet transform for the first and second systems are different (Fig. 1). However, the maximum energy occurs at approximately the same time scale s for both cases. According to Fig. 1, the phase difference $\phi_{s1}(t) - \phi_{s2}(t)$ increases infinitely for all time scales. This means that the sys-
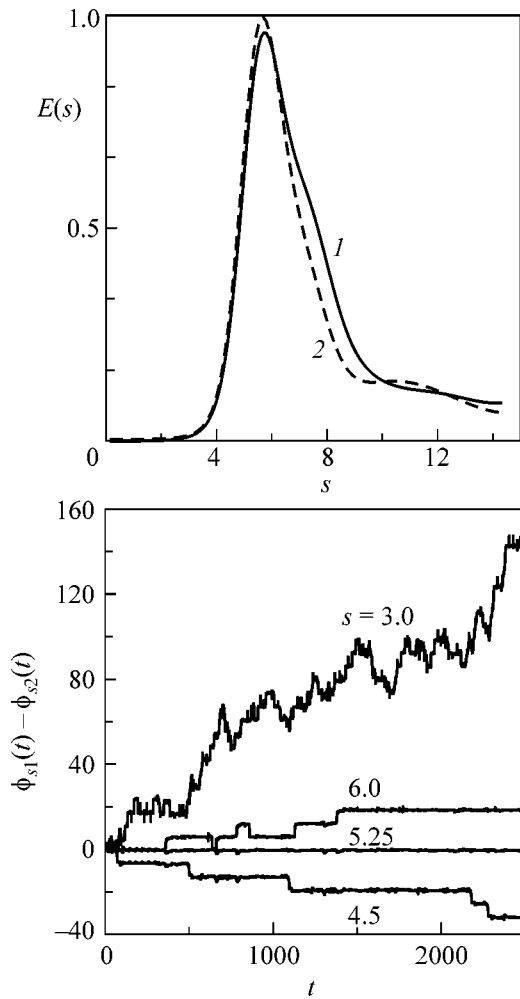
Fig. 2. The same as in Fig. 1 but for the coupling parameter $\varepsilon = 0.05$. Both systems are synchronized with each other on the time scales $s = 5.25$, and phase-synchronization regime prevails in the systems.

tems under consideration do not involve synchronized time scales. Therefore, the systems are unsynchronized.

As the coupling parameter increases, the systems are brought to the phase-synchronization regime (see, e.g., [11]). In particular, indirect measurements [12] show that two coupled Rössler systems with the coupling parameter $\varepsilon = 0.05$ are in the phase-synchronization regime. Figure 2 shows the phase difference $\phi_{s1}(t) - \phi_{s2}(t)$ for this case. It is seen that phase locking occurs at the time scale $s = 5.25$ corresponding to the maximum energy in the wavelet spectrum $E(s)$ (Fig. 2). Thus, two Rössler systems are synchronized with each other at the time scale $s = 5.25$ and, simultaneously, at close time scales. It is significant that strongly differing time scales (e.g., $s = 4.5$, 6.0, etc.) remain unsynchronized, and phase locking is not observed for these scales (see Fig. 2 and cf. Fig. 1).
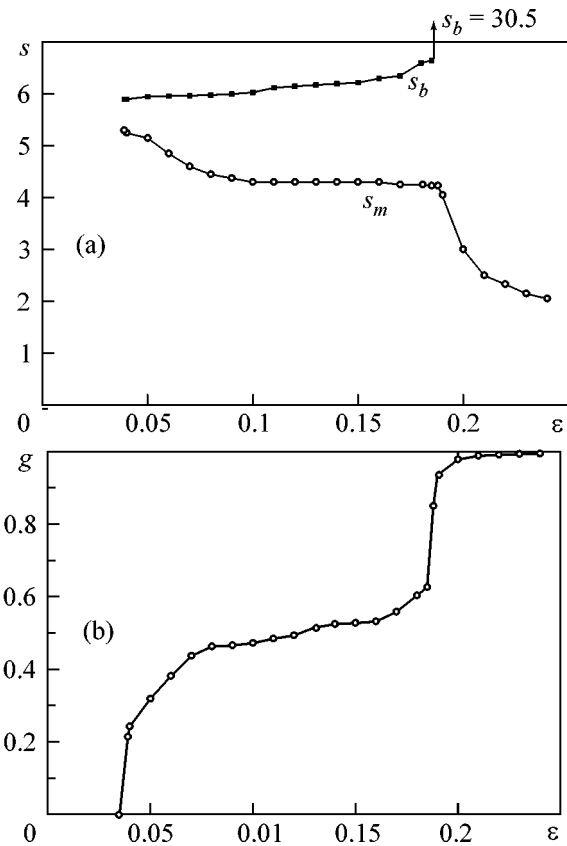
Fig. 3. (a) The upper s_b and lower s_m boundaries of the region of synchronized scales, and (b) the energy fraction γ falling on the synchronized scales for the Rössler system vs. the coupling parameter ε.

With a further increase in the coupling parameter, the hitherto unsynchronized time scales become synchronized. The number of time scales for which the phase locking occurs increases. At the same time, some time scales remain unsynchronized. With a further increase in the coupling parameter ϵ, the number of synchronized time scales increases, and, when all time scales are synchronized, the lag synchronization regime prevails in the system [18].

The above qualitative picture of time-scale synchronization is illustrated in Fig. 3a, in which the upper s_b and lower s_m boundaries of the scale range where synchronization condition (10) is met are shown as functions of the coupling parameter ε. The chaotic phase synchronization arises at $\varepsilon = 0.039$, when phase locking occurs in a certain scale range $\Delta s = (s_b - s_m)$. Further, with an increase in ε, the range Δs of synchronized scales expands until all scales become synchronized (lag synchronization regime).

It is convenient to characterize the degree of chaotic synchronization of two chaotic subsystems by the

energy fraction falling on the synchronized scales in the wavelet spectrum:

$$\gamma = \int_{s_m}^{s_b} E(s)ds / \int_0^\infty E(s)ds, \qquad (12)$$

where $E(s)$ is the integral energy distribution over scales (9) for the wavelet spectrum. The corresponding $\gamma(\varepsilon)$ dependence is shown in Fig. 3b. As is seen, the energy fraction falling on the synchronized scales of the chaotic oscillatory process increases with an increase in the coupling parameter. For the coupling parameter $\varepsilon = 0.039$ corresponding to the appearance of the phase synchronization regime, the energy fraction falling on the synchronized scales is $\gamma = 0.21$. For large coupling parameters ($\varepsilon > 0.2$), γ tends to unity, which means that the whole energy of chaotic oscillations falls on the synchronized scales, and, as was mentioned above, the lag synchronization regime prevails in the system.

In conclusion, several important comments are noteworthy. First, the traditional approaches (1)–(4) of revealing the phase-synchronization regime through the introduction of a phase of the chaotic signal can be used for the analysis of time series characterized by the Fourier spectrum with a pronounced main frequency f_0. In this case, the phase ϕ_{s0} introduced for the time scale $s_0 \simeq 1/f_0$ approximately coincides with the phase $\phi(t)$ introduced for the chaotic signal by the traditional method given by Eqs. (1)–(4). Indeed, since the other frequencies (or other time scales) do not make a tangible contribution to the Fourier spectrum, the phase $\phi(t)$ of the chaotic signal is close to the phase $\phi_{s0}(t)$ of the main frequency component f_0 (and, correspondingly, of the main time scale s_0). In this case, the average frequencies $\bar{f} = \langle\dot{\phi}(t)\rangle$ and $\bar{f}_{s0} = \langle\dot{\phi}_{s0}(t)\rangle$ must coincide with each other and with the main Fourier frequency f_0 (see [13]):

$$\bar{f} = \bar{f}_{s0} = f_0. \qquad (13)$$

If the chaotic time realization is characterized by the Fourier spectrum without a pronounced main spectral component, the traditional approaches given by Eqs. (1)–(4) do not apply. In this case, the behavior of the system must be considered at various time scales. However, such a consideration is impossible with the use of instantaneous phase $\phi(t)$ introduced for the chaotic signal by Eqs. (1)–(4). In contrast, the approach proposed above on the basis of continuous wavelet transform with the introduction of a continuous phase set can be successfully used for any type of chaotic signal.

This approach can also be used to analyze the experimental data, because it does not require any *a priori* information on the system under study. Moreover, the wavelet transform can reduce the noise effect in some cases [15, 19]. The above method can likely be useful and efficient for analyzing the time series generated by physical, biological, physiological, and other systems.

Thus, a new method for describing the chaotic synchronization is proposed. It is based on the continuous wavelet transform and analysis of the system dynamics on various time scales. This approach applies to any chaotic systems and experimental time series.

REFERENCES

1. M. G. Rosenblum, A. S. Pikovsky, and J. Kurths, Phys. Rev. Lett. **76**, 1804 (1996).

2. A. Pikovsky, M. Rosenblum, and J. Kurths, *Synchronization: a Universal Concept in Nonlinear Sciences* (Cambridge Univ. Press, Cambridge, 2001).

3. U. Parlitz, L. Junge, and W. Lauterborn, Phys. Rev. E **54**, 2115 (1996).

4. E. Allaria, F. T. Areochi, A. Di Garbo, and R. Meucci, Phys. Rev. Lett. **86**, 791 (2001).

5. I. Z. Kiss and J. L. Hudson, Phys. Rev. E **64**, 046215 (2001).

6. V. S. Anishchenko, A. G. Balanov, N. B. Janson, *et al.*, Int. J. Bifurcation Chaos Appl. Sci. Eng. **10**, 2339 (2000).

7. C. M. Ticos, E. Rosa, Jr., W. B. Pardo, *et al.*, Phys. Rev. Lett. **85**, 2929 (2000).

8. A. Pikovsky, M. Rosenblum, and J. Kurths, Int. J. Bifurcation Chaos Appl. Sci. Eng. **10**, 2291 (2000).

9. V. S. Anishchenko and T. E. Vadivasova, Radiotekh. Élektron. (Moscow) **47**, 117 (2002).

10. A. S. Dmitriev and A. I. Panas, *Dynamical Chaos. New Information Carriers for Communication Systems* (Fizmatlit, Moscow, 2002).

11. M. G. Rosenblum, A. S. Pikovsky, and J. Kurths, Phys. Rev. Lett. **78**, 4193 (1997).

12. M. G. Rosenblum, A. S. Pikovsky, and J. Kurths, Phys. Rev. Lett. **89**, 264102 (2002).

13. V. S. Anishchenko and T. E. Vadivasova, Radiotekh. Élektron. (Moscow) **49**, 123 (2004).

14. G. V. Osipov, B. Hu, C. Zhou, *et al.*, Phys. Rev. Lett. **91**, 024101 (2003).

15. A. A. Koronovskiĭ and A. E. Khramov, *Continuous Wavelet Analysis and Its Applications* (Fizmatlit, Moscow, 2003).

16. J. P. Lachaux, E. Rodriguez, M. Le Van Quyen, *et al.*, Int. J. Bifurcation Chaos Appl. Sci. Eng. **10**, 2429 (2000).

17. A. J. Lichtenberg and M. A. Lieberman, *Regular and Stochastic Motion* (Springer, New York, 1982; Mir, Moscow, 1984).

18. M. G. Rosenblum, A. S. Pikovsky, and J. Kurths, Phys. Rev. Lett. **78**, 4193 (1997).

19. V. A. Gusev, A. A. Koronovskiĭ, and A. E. Khramov, Pis'ma Zh. Tekh. Fiz. **29** (9), 61 (2003) [Tech. Phys. Lett. **29**, 775 (2003)].

Translated by R. Tyapaev

Stimulated Smith–Purcell Radiation

A. N. Aleĭnik, A. S. Aryshev*, E. A. Bogomazova, B. N. Kalinin, G. A. Naumenko, A. P. Potylitsyn, G. A. Saruev, and A. F. Sharafutdinov

Research Institute of Nuclear Physics, Tomsk Polytechnical University, pr. Lenina 30, Tomsk, 634050 Russia
*e-mail: alar@chair12.phtd.tpu.edu.ru
Received February 17, 2004

The design of free-electron lasers (FELs) based on submillimeter-range undulators involves difficulties associated with the fabrication of undulators with a very small period. To do this also requires accelerators with high-energy electron beams (>50 MeV). It should also be taken into account that these facilities use precision and expensive magnetic systems. In some works, an alternative FEL mechanism based on the use of the Smith–Purcell radiation (SPR) was considered. To realize the feedback in such an FEL, one must use a basically different cavity scheme. This work reports the results of experimental study on the stimulated SPR in a "transverse" cavity. © 2004 MAIK "Nauka/Interperiodica".

PACS numbers: 41.60.-m; 41.75.Fr

Free-electron lasers (FELs) based on the undulator radiation generated upon the electron-beam passage through a periodic magnetic structure [1, 2] have gained wide acceptance [3, 4]. The design of submillimeter FELs based on a compact electron amplifier and undulator involves problems associated with the fabrication of a small-period undulator, complexity and expensiveness of its magnetic system, and the necessity of using an amplifier with a low electron-beam emittance. For this reason, a search for the alternative mechanisms in engineering FELs becomes evident. For instance, the possibility of using the Smith–Purcell radiation (SPR) in FELs was considered in [5–7]. The SPR [8] is a diffraction radiation of electrons flying in vacuum near a periodic structure. Such a device with a continuous electron beam (orotron) is less expensive and more compact than traditional FELs [9]. When using the SPR, it is necessary to use a "transverse" cavity, because the radiation is generated at large angles to the electron beam.

The idea of using a preliminary bunched electron beam for the fabrication of so-called broadband millimeter FEL evolved several years ago and was experimentally tested in [10], where a coherent continuous synchrotron radiation of a bunched electron beam was accumulated in a conventional ("longitudinal") optical cavity to stimulate radiation from the subsequent bunches. A broadband stimulated transient far-IR radiation was also observed in [11].

In [12], an FEL based on the SPR generated by electrons with energy $E_{e^-} = 10$ keV flying near the standard "bulk" grating was studied experimentally. The feedback was effected by a transverse cavity that included the target and reflecting gratings. As was demonstrated in [13, 14], the use of a "plane" grating consisting of periodically arranged conducting strips separated by nonconducting spacers noticeably improves the generation efficiency. Moreover, the SPR from a plane grating is maximal in the plane perpendicular to its surface, in contrast to the SPR from a bulk grating, where the radiation has a two-mode azimuthal distribution. This allows the use of a comparatively simple scheme for the cavity.

In our experiment, the SPR was generated on a plane periodic target consisting of conducting strips applied to a dielectric. To a first approximation, one can assume that the target consists of ideally conducting strips separated by vacuum gaps. This allows the estimation of the radiation energy per electron for our geometry [13]:

$$W_{sp} = W_{ss} F_{\text{strip}} F_N,$$

where W_{ss} is the intensity of diffraction radiation from a semi-infinite plane,

$$W_{ss} = \frac{\alpha}{4\pi^2} \frac{\exp\left(-\frac{4\pi h}{\gamma \lambda}\right)}{1 - \cos\theta},$$

$$F_{\text{strip}} = 4\sin^2\left(\frac{\pi a}{\lambda}(\cos\theta - 1/\beta)\right),$$

$$\beta = \sqrt{1 - \frac{1}{\gamma^2}}, \quad \gamma \text{ is the Lorentz factor,}$$

$$F_N = \frac{\sin^2\left(\frac{N_s \varphi_0}{2}\right)}{\sin^2\left(\frac{\varphi_0}{2}\right)}, \quad \varphi_0 = \frac{2\pi d}{\lambda}(\cos\theta - 1/\beta).$$

Here, $\alpha = 1/137$ is the fine structure constant, a is the strip width, d is the grating period, λ is the SPR wavelength, β is the electron velocity, and θ is the observation angle.

The dependence of the SPR wavelength on the observation angle (Fig. 1) was calculated for the following geometry: $\theta = 90°$, $\gamma = 12$, $d = 12.7$ mm, and $a = d/2$; $k = 1, 3$ is the diffraction order. This figure demonstrates that the radiation wavelength strongly depends on the observation angle. In the experiment, we chose $\theta = \pi/2$, which corresponds to $\lambda = d$. For several strips (in our case, $N_s = 12$), the SPR line broadens to $\Delta\lambda/\lambda \approx 0.17$ [15].

If the radiation wavelength λ of the bunched relativistic electron beam is comparable to or larger than the bunch length L_b, all bunch electrons radiate coherently. In this case, the radiation intensity is proportional to N_e^2 (N_e is the number of electrons in the bunch).

If the electron-beam cross-sectional size σ_x satisfies the condition $\sigma_x \ll \gamma\lambda$, the intensity of the coherent SPR (CSPR) can be expressed through the longitudinal formfactor as

$$W_{coh} = N_e^2 \left| f_z\left(\frac{2\pi\sigma_z}{\lambda\beta}\right) \right|^2 W_{SP},$$

where f_z is the longitudinal geometric factor [10, 11].

For example, one has $|f_z|^2 > 0.5$ for the Gaussian longitudinal distribution with $\sigma_z/\lambda < 0.13$ (σ_z is the bunch longitudinal size taken equal to triple standard deviation). Therefore, the estimate for the CSPR power from a single macropulse of duration 2–6 μs is ~0.6 W for our accelerator [15].

A periodic target consisting of $0.35 \times 50 \times 0.03$-mm copper strips applied with the period $d = 12.7$ mm to a glass textolite substrate can be used simultaneously as a radiation oscillator and a cavity mirror. In our experiment, the SPR with a wavelength coinciding with the grating period is generated in the direction perpendicular to the electron beam ($\theta = 90°$). Thus, the feedback cavity should be arranged perpendicular to the electron beam. If the strip width is equal to one-half of the grating period, the reflection coefficient of the grating will be close to unity for the wavelengths $\lambda \approx d$ [16]. Consequently, one can use the grating as a cavity mirror. The resonance condition for this cavity is the following: $2L = k\lambda$, where L is the cavity length and k is an integer. For the resonance between bunches to occur, it is necessary that the condition $\lambda_{RF} = m \times 2L$ be met, where λ_{RF} is the wavelength of the high-frequency system (i.e., the distance between bunches) and m is an integer. Taking into account the Smith–Purcell condition $\lambda = d$ for $\theta = \pi/2$, we can obtain the system of equations for the target and cavity parameters:

$$2L = k\lambda, \quad \lambda_{RF} = m \times 2L, \quad \lambda = d.$$
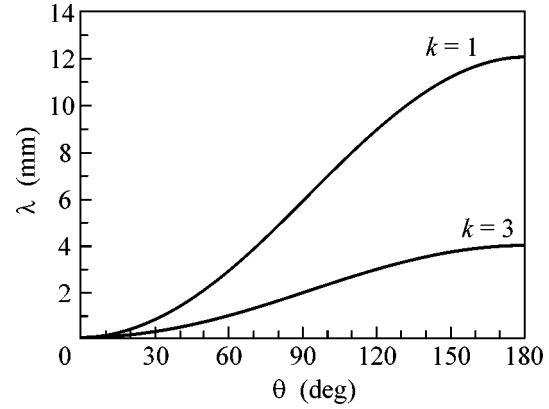
Fig. 1. Dependence of the SPR wavelength on the observation angle; $\theta = 90°$, $\gamma = 12$, $d = 12.7$ mm, and $a = d/2$; $k = 1, 3$ is the diffraction order.
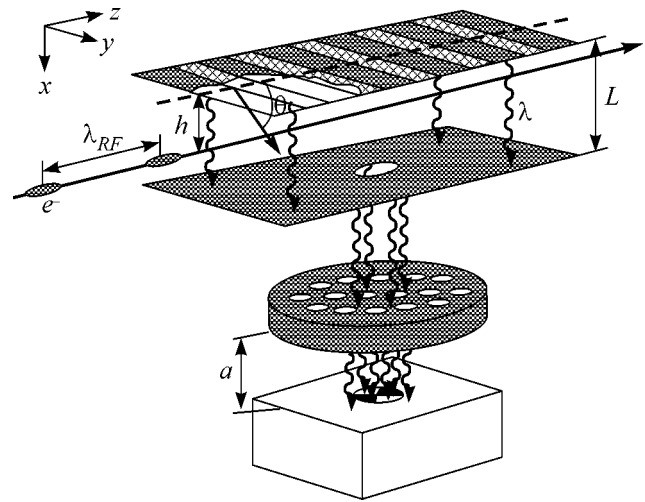

Fig. 2. Geometry of the experiment.

Experiment (Fig. 2) was conducted on the microtron of the Research Institute of Nuclear Physics, Tomsk Polytechnic University. The microtron parameters are described in [15, 17]. A microtron beam with an energy of 6.1 MeV consists of macrobunches following with a repetition rate of 8 Hz. Each macrobunch consists of 10^4 microbunches of length $L_b \approx 6$ mm and contains 10^8 electrons. The distance $\lambda_{RF} = 114$ mm between the bunches is determined by the microtron high-frequency system.

The cavity was placed in a vacuum chamber. The cavity mirror had two degrees of freedom for measuring the parameter L and tuning the overlap between the target and mirror. The following cavity parameters were chosen: $m = 1$ and $k = 9$, so that $d = 12.7$ mm and $L = 57$ mm. The lower mirror had a hole with a diameter of 10 mm for feeding the stimulated radiation into a
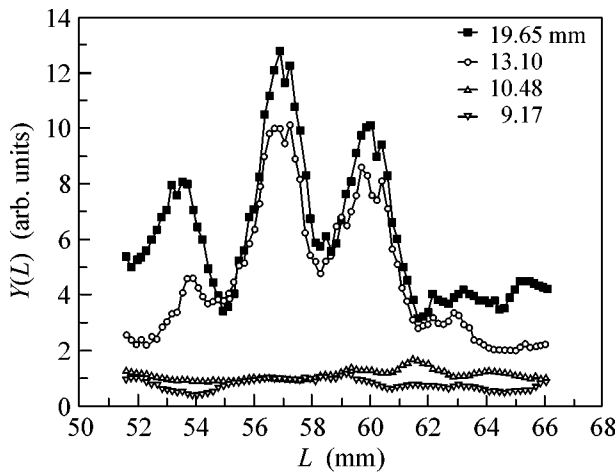
Fig. 3. Dependence of the stimulated CSPR on the cavity length *L*.
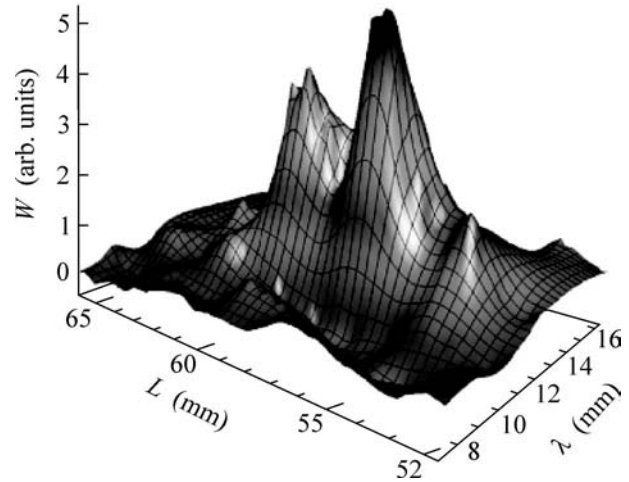
Fig. 4. Dependence of the stimulated CSPR intensity on the wavelength and the parameter *L*.

detector. The distance from the cavity mirror to the detector window was 60 cm. Estimates showed that the influence of the near zone can be ignored under the conditions of our experiment. To measure the background at each point, a controlled "shutter" was used. The statistical error of measurements was less than 5%.

The spectral range of the CSPR is determined by the length of an electron bunch (~6 mm). The radiation was recorded by a detector based on a broadband antenna with a preamplifier of the output signal. The sensitivity band of the detector lies in the range $\lambda = (1–20)$ mm, its sensitivity is ≈ 1.3 V/W, and the diameter of its entrance window is 10 mm.

Measurements were made using six wave filters with diameters $D_c = 5, 6, 7, 8, 10,$ and 15 mm. The critical wavelength of a filter is related to its diameter by $\lambda_c = 1.7 D_c$ [18].

The stimulated CSPR (the coherence was confirmed by the current dependence; see [17]) into the aperture of a $1/2\gamma$ detector was studied experimentally for different filters (different λ_c) and different distances L between the mirror and the target. The radiation output,

$$Y(\lambda_c, L) = \int_{\lambda_{min}}^{\lambda_c} W(\lambda, L) d\lambda,$$

was determined under the assumption that the filter transmission capacity ε can be approximated by the theta function $\theta(\lambda_c - \lambda)$, where λ_{min} is the detector detection limit ($\lambda_{min} < \lambda_c$). This formula can be used to reproduce the dependence of the stimulated SPR intensity on the wavelength and the parameter L:

$$W(\lambda, L) = \frac{\partial Y(\lambda, L)}{\partial \lambda}.$$

In Fig. 3, the experimentally determined $Y(L)$ functions are shown for different values of parameter λ_c.

One can see that the CSPR output markedly (by at least a factor of six) increases for the wavelengths $\lambda > 10.48$ mm under the resonance conditions. Estimates show that the CSPR linewidth is equal to approximately 17 mm, and, hence, the minimal radiation wavelength is $\lambda_{min} \approx 11.6$ mm, in good agreement with the experiment. The three peaks on the curves for the L dependence correspond to the resonances of different orders. The separation $\Delta L = 3$ mm $\approx \lambda/4$ between the peaks (in contrast to the experiment [10], where $\Delta L \approx \lambda/2$) is caused by the fact that the phase does not change upon the reflection from the grating (see [16]). The measurement results are evidence of recording the stimulated CSPR. The function $W(\lambda, L)$ is shown in Fig. 4. The peak in the curve for the λ dependence corresponds to the peak in the CSPR spectrum and arises, as expected, at the point coinciding with the lattice parameter.

Note in conclusion that we have used a strict dependence of the radiation wavelength on the CSPR observation angle in our experiment. The grating period and the cavity length were chosen so that the resonance conditions were met. The CSPR output was measured using wave filters. Contrary to the experiment in [10], where a 30-fold enhancement of the output radiation intensity was detected for the stimulated coherent synchrotron radiation under the resonance conditions, we have obtained an approximately sixfold enhancement, probably because the background could not be fully excluded and due to a low Q factor of the "grating–mirror" cavity. Contrary to the experiments in [10, 11], the stimulated CSPR provides a monochromatic output radiation with a wavelength determined by the grating period, cavity geometry, and bunch length.

REFERENCES

1. H. Motz, J. Appl. Phys. **22**, 527 (1951).

2. J. M. J. Madey, J. Appl. Phys. **42**, 1906 (1971).

3. C. A. Brau, *Free Electron Lasers* (Academic, San Diego, 1990).

4. J. M. Ortega *et al.*, Nucl. Instrum. Methods Phys. Res. A **375**, 618 (1996).

5. A. Gover, Appl. Phys. **16**, 121 (1978).

6. J. M. Wachtel, J. Appl. Phys. **50**, 49 (1979).

7. A. Doria, G. P. Gallerano, E. Giovenale, *et al.*, Nucl. Instrum. Methods Phys. Res. A **475**, 318 (2001).

8. S. J. Smith and E. M. Purcell, Phys. Rev. **92**, 1069 (1953).

9. F. S. Rusin and G. D. Bogomolov, Izv. Vyssh. Uchebn. Zaved., Radiofiz. **11**, 756 (1968).

10. Y. Shibata, K. Ishi, S. Ono, *et al.*, Nucl. Instrum. Methods Phys. Res. B **145**, 49 (1998).

11. H.-C. Lihn, P. Kung, C. Settakorn, and H. Wiedemann, Phys. Rev. Lett. **76** (22), 4163 (1996).

12. V. Baryshevsky, K. Batrakov, A. Gurinovich, *et al.*, Nucl. Instrum. Methods Phys. Res. A **483**, 21 (2002).

13. J. H. Brownell, J. Walsh, and G. Doucas, Phys. Rev. E **57**, 1075 (1998).

14. A. P. Potylitsyn, Nucl. Instrum. Methods Phys. Res. B **145**, 60 (1998).

15. A. N. Aleĭnik, A. S. Aryshev, B. N. Kalinin, *et al.*, Izv. Vyssh. Uchebn. Zaved., Fiz. **1**, 85 (2004).

16. L. A. Vaĭnshteĭn, *The Theory of Diffraction. Microwave Electronics* (Radio i Svyaz', Moscow, 1995).

17. A. N. Aleĭnik, A. S. Aryshev, B. N. Kalinin, *et al.*, Pis'ma Zh. Éksp. Teor. Fiz. **76**, 397 (2002) [JETP Lett. **76**, 337 (2002)].

18. K. Hanke *et al.*, *Beam Diagnostics Using Coherent Transition Radiation at CLIC Test Facility*, CLIC Note 298 (1996).

Translated by V. Sakun

Narrow-Directed Fast-Ion Flow Generation from Targets Irradiated by a Picosecond Laser Pulse

A. A. Andreev[1], V. P. Andrianov[2], V. G. Borodin[3], V. M. Komarov[3], V. A. Malinov[3], N. V. Nikitin[3], A. V. Serdyukov[3], A. V. Charukhchev[3], V. N. Chernov[3], K. Yu. Platonov[4], *, A. V. Bessarab[5], S. G. Garanin[5], A. A. Gorbunov[5], and N. A. Suslov[5]

[1] *All-Russia Scientific Center, Vavilov State Optical Institute, Birzhevaya liniya 12, St. Petersburg, 199034 Russia*
[2] *Research Institute of Pulse Technology, Moscow, 115304 Russia*
[3] *Research Institute for Complex Testing of Optoelectronic Devices, Sosnovyĭ Bor, Leningrad region, 188540 Russia*
[4] *St. Petersburg State Technical University, ul. Politekhnicheskaya 29, St. Petersburg, 195434 Russia*
*e-mail: platonov@quark.stu.neva.ru
[5] *Russian Federal Nuclear Center, Institute of Experimental Physics, Arzamas-16, Nizhni Novgorod region, 607190 Russia*
Received February 11, 2004; in final form, March 4, 2004

The proton and deuteron yields from thin targets irradiated by a picosecond laser pulse with an average radiation intensity of $\leq 4 \times 10^{18}$ W/cm^2 at the target were measured in the megaelectron-volt energy range. A ring structure was observed for the outgoing ions, and the angular ion-beam divergence was found to be extremely small (0.5°). The fast-ion generation mechanism allowing for the appearance of ring structure is discussed, and the characteristic energies and spatioangular ion-beam distribution are estimated. © *2004 MAIK "Nauka/Interperiodica".*

PACS numbers: 52.50.Lp

Laser plasma produced by ultrashort laser pulses with an intensity of $I_L \geq 10^{18}$ W/cm^2 is a source of intense ion flows in the megaelectron-volt energy range [1–6]. The study of the expansion parameters for such ions would be helpful in gaining information about the ion acceleration mechanisms and the ways of controlling the energetic and spatial parameters of ions, which will allow, hence, the implementation of the idea of designing laser-plasma ion accelerators. Moreover, these ions can be used in various applications, including radiography and initiation of a "fast ignition" by light ions in laser thermonuclear synthesis.

The generation of high-energy protons by a pulse of duration $t_L = 130$ fs and $I_L \approx 10^{18}$ W/cm^2 was studied in [7]. The maximal energy of the forward-emitted protons was found to be $\varepsilon_{i\,max} = 2.2$ MeV. For $I_L \approx 2 \times 10^{18}$ W/cm^2 and $t_L \approx 2$–4 ps, $\varepsilon_{i\,max} = 4.2$ MeV [6], and $\varepsilon_{i\,max} \approx 18$ MeV for $I_L \approx 5 \times 10^{19}$ W/cm^2 [8] and a relatively long (0.4 ns) laser pulse. Common to these works was that the experiments were carried out with a comparatively high heating-pulse contrast and, correspondingly, for a small scale of plasma-density inhomogeneity.

In this work, the spectra of protons emitted from the face side of a Be target were measured and the spatial distribution of ions emitted from its rear side was studied for an average laser intensity at the target surface of $(1–4) \times 10^{18}$ W/cm^2.

The experiments were carried out on a PROGRESS-P picosecond laser [9, 10] with a radiation wavelength of 1.054 μm, energy $\varepsilon_L \leq 8$ J, and a pulse duration of 1.2–2 ps. The radiation was focused by an off-axis parabolic mirror with f/1.4 (the laser beam diameter was 145 mm). The target was set at an angle of ~30° with the focused *p*-polarized beam. In the experiments, the power contrast of the amplified luminescence pulse did not exceed 10^{-8}, and the prepulse intensity measured by a single-pulse autocorrelator 10–100 ps before the main pulse showed that its intensity was lower than the detection threshold of the technique used ($\leq 10^{-3}$). The scheme of the experiment is shown in Fig. 1.

Calibrated CR-39 track detectors were used to detect charged particles. The ion energy spectra were measured using cassettes with a set of holes covered by Ta, Al, and Cu filters of different thickness (1.6–300 μm) to span the proton energy interval of 0.2–35 MeV. Some of the detectors were placed on the side of the irradiated surface near the normal to the target at angles $\varphi = 0°$ and $30°$ at a distance of 15–25 cm from the focal point. The detectors were arranged in this way because the fast ions with energies above 100 keV were mainly emitted within a comparatively narrow cone ($\pm 20°$) near the normal at both face and rear target sides [11]. One of the detectors was placed at a distance of 3 cm behind the target. Be (12 μm), Ti, and TiD$_x$ (30 μm) foils were user as targets.

Analysis of the experimental data shows that the main fraction of protons emitted from the target rear side have energies within 0.7–2.3 MeV. At the same time, the energy of the main particle flow from the target face side, i.e., in the direction of focusing optics, is 0.3–1.5 MeV. The presence of protons in the targets that initially did not contain hydrogen was caused by the deposition of water vapor and hydrocarbon compounds on them. In the experiments with the Be target, a ring structure was observed for emitted ions behind the target (Fig. 3).

Let us now discuss the experimental results in more detail. In the course of interaction between an intense laser pulse and the target, most of the fast electrons penetrate through the thin target and fly out from its rear side. The electric field arising on the rear side of the foil upon electron escape accelerates ions. The electric field also arises on the face side of the foil, but it is caused by the ponderomotive pressure that forces electrons through ions in a skin layer. Therefore, ions are accelerated on both sides of the target. It is shown in [12] that, if the foil thickness is much smaller than the mean free path of fast electrons, the ion flow behind the target is mainly formed by the ions accelerated at the rear side of the target, so that the ion acceleration essentially depends on the coefficient K_e of laser-energy conversion into the fast-electron energy and on the electron energy ε_{eh}. The number of fast electrons can be estimated as $N_{eh} = K_e \varepsilon_L / \varepsilon_{eh}$, where ε_L is the pulse energy and $K_e \approx 0.03 + \eta I_{18}/(30 + I_{18})$ ($I_L \leq 10^{18}$ W/cm^2, $t_L \leq$ 1 ps [4]), where $\eta \approx 0.2 + (0.1 + 0.06L/\lambda_L)I_{18}/(15 + I_{18})^{0.8}$ is the absorption coefficient [11], I_{18} is the laser intensity in units of 10^{18} W/cm^2, and L is the plasma-density inhomogeneity scale determined by the prepulse. The mean energy of fast electrons is [13] $\varepsilon_{eh} \approx m_e c^2(\sqrt{1 + I_{18}(\lambda_L/1.2\mu m)^2} - 1)$. These formulas are valid in the intensity interval 10^{18}–10^{20} W/cm^2 and for the pulse durations $t_L \leq 1$ ps. For the maximal experimental intensity $I_L = 4 \times 10^{18}$ W/cm^2 and $L = 8$ μm, one has $K_e \approx 0.08$, $\varepsilon_{eh} \approx 0.5$ MeV, and $N_{eh} \approx 8 \times 10^{12}$. The energy spectrum of hot electrons at the face side of the target (30 μm) is shown in Fig. 2. The mean energy is $T_{eh} \approx 0.4$ MeV, which corresponds to the above estimate for energy ε_{eh}. The ordinate in Fig. 2 is the electron-flow density in a detector with an entrance hole of diameter 30 μm; the detector is placed at a distance of 3 cm from the target at an angle of 80° to its face side. Assuming that the electron angular distribution is uniform, we find that the number of electrons emitted from the face side of the target is ~10^{10}. A more detailed numerical simulation [17] of electron escape from the face side showed the presence of weak maxima at the take-off angles of 50°–80°; this does not affect, by the order of magnitude, our estimate of the total number of emitted electrons.
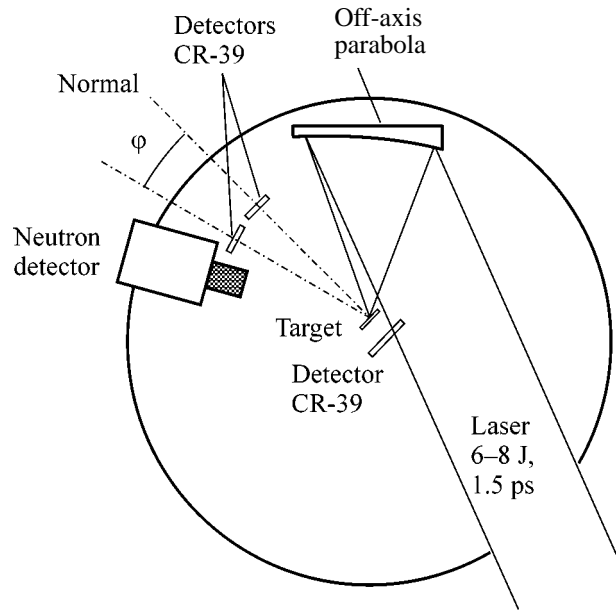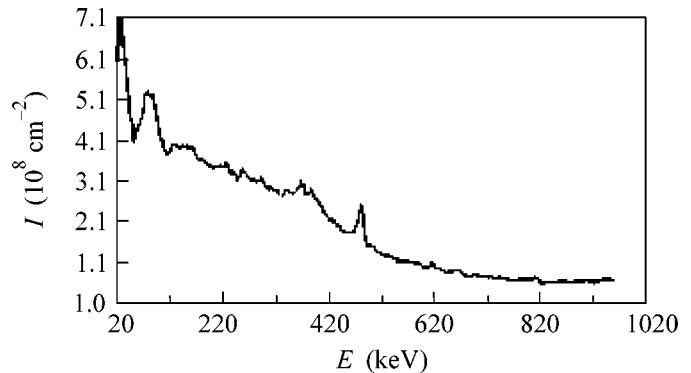

Fig. 1. Scheme of the experiment.

Fig. 2. Energy dependence of the number of fast electrons per detector unit area. A detector with an entrance hole of diameter 30 μm is situated at a distance of 3 cm at an angle of 80° to the face side of a Ti (30 μm) target.

Inasmuch as the foil thickness is smaller than the electron mean free path, electrons propagate inside the target within a cone with angle ≤10°, so that the electron-beam radius can be estimated as ~R_L. The beam self-magnetic field has a substantial effect on the electron flow in target plasma, because the beam current far exceeds the Alfvén current, ~$eN_{eh}/t_L \gg m_e c^3/e$. Such a beam can propagate only in the presence of a backward current that compensates its self-magnetic field [12].

The spatial electron-charge distribution in vacuum on the rear side of the foil plays the key part in the explanation of the experimental ion-beam characteristics. After the electron flow passes through the foil

0.5 mm
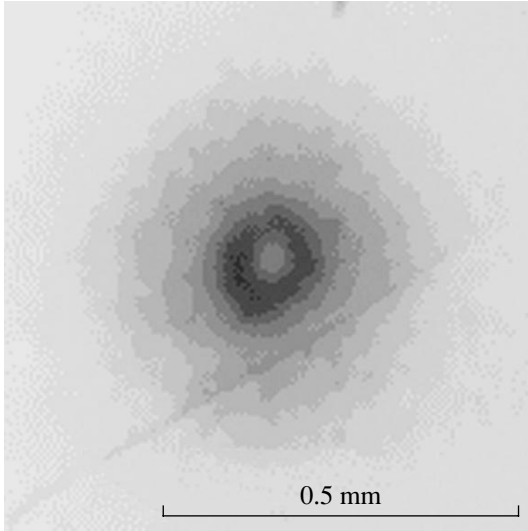
Fig. 3. Spatial distribution of ions emitted from the target rear surface. The pattern is recorded on a film screen situated 3 cm behind the target.

boundary, its propagation in vacuum in the form of a flow becomes impossible. Indeed, the maximal distance h at which the electron beam of radius R can move away from the foil surface can be estimated by equating the electrostatic energy $e^2 N_{eh}^{(1)2}/2R$ ($N_{eh}^{(1)} = \pi R^2 h n_{eh}$) of a beam segment outside the foil and its kinetic energy $N_{eh}^{(1)} \varepsilon_{eh}$, to obtain $h \approx \varepsilon_{eh} R c t_L / e^2 N_{eh}$. One also has $n_{eh} \approx N_{eh}/\pi R^2 c t_L$. The beams self-magnetic field $H_{max} \approx 2\pi e n_{eh} R v_{eh}/c$ is not compensated in vacuum by the back current, and, hence, it prevents the Coulomb expansion. However, the Lorentz factor is $\gamma_e \approx 1$ for $\varepsilon_{eh} = 0.5$ MeV, so that the corresponding decrease in forces by a factor of $2\gamma_e^2$ can be ignored. The quantity h can be regarded as the largest distance for which one may apply the term "electron beam" to electrons moving away from the surface. In actuality, due to the attraction by surface ions, the mean distance at which electrons can move away is equal to the Debye radius $r_d \lesssim h$ of fast electrons ($r_d = v_{eh}/\omega_{ph}$, where $v_{eh} \sim c$ and $\omega_{ph} \approx (4\pi e^2 n_{eh} c^2/\varepsilon_{eh})^{1/2}$). Therefore, due to the presence of radial repulsive forces and the inflow of new electrons from the target, the electron cloud and the positive charge at the back surface of the target will spread.

To describe the structure $n_{eh}(r, t)$ of electron cloud over the surface ($z > 0$), we use the system of hydrodynamical equations for electrons. We assume that ions are fixed, i.e., $n_i(z) = n_0 \theta(-z)$ and the geometry of the system is cylindrical, and the presence of an electron source with radius R_L and current density $j = e c n_{eh}(0)$ at the surface ($z = 0$) will be taken as a boundary condition. The electric field and the velocity have the radial and z components. We estimate the fields assuming that

r_d and R_L are the characteristic scales along the z and radial coordinates, respectively. Then, $E_z \approx \varepsilon_{eh}/er_d$ and $E_r \approx \varepsilon_{eh}/eR_L$. The magnetic field has only the azimuthal component that is created not only by the axial (along z) but also by the radial current. Evidently, H_φ and E_r are zero at the center of the spot, reach maximum at $r \approx R_L$, and then decrease. The vortex electric-field component can be ignored compared to the ambipolar component, because $\tilde{E}_z \approx (R_L/ct_L)H_\varphi \ll H_\varphi, E_z$. Let us consider electron dynamics in the given fields. The field E_z decelerates electrons, while the field E_r spreads them over the surface. When spreading, electrons are brought into the region where the magnetic field H_φ is maximal. Since $r_H = v_r m_e c/eH_\varphi \approx r_d$, the electron will be "captured" by the magnetic field, and its radial motion will slow down. The Lorentz-force component $F_z = e v_r H_\varphi/c$ in a magnetic field H_φ tends to pull electrons away from the surface, while the component $F_r = -e v_z H_\varphi/c$ brings them back to the center. According to numerical calculations [12, 14], an electron ring should then arise, under which the ions are accelerated by the field $E_z + v_r H_\varphi/c$ with a maximum at $r \approx R_L$, to reproduce the ring structure if the electron-ring lifetime is comparable with the ion acceleration time. When moved to vacuum, ions are brought to the region of radial forces from the electron cloud disposed over the surface. The typical ion-emission angles can be estimated from the electron-density distribution. A well-defined ion ring structure in the detector (Fig. 3) is evidence that the electron-ring radius does not change appreciably during the ion acceleration. For this reason, the radial force acting on an electron in the region of maximal magnetic field $\max H_\varphi = H_\varphi^{(m)} \approx -(4\pi e/c) n_{eh}^{(m)} R_L v_z$ can be set zero; i.e., $F_r = -e v_z H_\varphi/c + eE_r \approx 0$. The electron concentration $n_{eh}^{(m)}$ in the region of maximal magnetic and electric fields can now be estimated as

$$n_{eh}^{(m)} \approx \frac{\varepsilon_{eh}}{4\pi e^2 R_L^2} \frac{c^2}{v_z^2} = \frac{\varepsilon_{eh} n_c}{mc^2 (k_L R_L)^2}\left(\frac{c}{v_z}\right)^2. \quad (1)$$

For $v_z \approx 0.3c$ (taken from [14]) and our parameters, $n_{eh}^{(m)} \approx n_{eh}$. The radial force from the electron cloud with concentration n_{eh} at the center of the ring tightens the ion ring into a beam. By contrast, electrons with concentration $n_{eh}^{(m)}$ situated in the region of the ring stretch the ion ring and, hence, defocus the ion beam. The resulting angular divergence depends on the total radial force. The corresponding equation of motion for fast ions in the transverse direction can be written as

$$m_i dv_l/dt \approx 2\pi Z e^2 R_b (n_{eh}^{(m)} - n_{eh}) \quad (2)$$

$(R_b \sim R_L$ is the ion-ring radius). The typical ion-emission angle estimated from Eq. (2) is

$$\theta_i \; = \; v_l/v_i \approx Ze^2\pi r_d R_b(n_{eh}^{(m)} - n_{eh})/\varepsilon_i. \qquad (3)$$

In the experiments with a Be target, we observed an ion ring with a radius of 0.2 mm. The distance between the target and detector was equal to 3 cm (Fig. 3). This restricted the exit angle to $\theta_i \leq 1°$. Thus, the radial forces acting on the ions during the acceleration were compensated ($n_{eh}^{(m)} \approx n_{eh}$). This explains the extremely low angular divergence of ions in our experiments.

Note that the ring structure of emitted ions was observed in [15] for a 1-ps pulse with an intensity of 5×10^{19} W/cm^2 incident on a 125-μm Al foil. In that work, the ion ring structure was explained by the deflection of ions accelerated at the face side of the foil and passed through it interacting with the electron-beam self-magnetic field. In our case of a lower intensity, this explanation cannot be considered satisfactory. Indeed, the gyroradius ratio of proton and electron is $m_i c^2 v_i/m_e \varepsilon_{eh} v_e \approx 10^2$ for a 0.5-MeV electron and a 2-MeV proton. Even if the electron deflection angle in a magnetic field is $\propto 60°$, the proton deflection will not exceed $0.6°$. Let us now estimate the characteristic scattering angle for a proton in a 12-μm Be foil. The tracks of 5000 3-MeV protons counted by the Monte Carlo method are presented in Fig. 4. Protons flew out from a fixed point at the face side of the target and passed, with scattering, through the foil, after which their tracks were traced up to a distance of 3 cm behind the target. With allowance for the scale in Fig. 4, the proton-beam width at the detector was equal to 1.5 mm. It is practically impossible to distinguish the rings with a width of ~0.1 mm (Fig. 3) for this scattering. Thus, we can assert that the ion ring structure is formed at the rear side of the foil. In [12], a similar conclusion was drawn on the basis of three-dimensional numerical PIC simulation. Note that such an explanation for the ring structure of escaping ions is absent in [12]. The inhomogeneous hydrogen distribution at the target surface is an alternative but, in our opinion, less probable cause for the formation of ring structures. In this case, it is necessary that the maximum of initial distribution lie at the center of the laser spot and that the inhomogeneity scale be much smaller than the spot diameter [19]. Note also that a narrow-directed (one-dimensional) fast-ion expansion was observed upon the incidence of a relativistic electron beam from an accelerator [20]. In our case, laser pulse plays the role of accelerator.

The transverse inhomogeneity in the electron-charge distribution and the transverse component of the ambipolar field exist only during the laser pulse. After the pulse, the electron density is leveled off. However, the ion acceleration in the longitudinal direction is continued, because the longitudinal-field relaxation time (ion acceleration time) exceeds the pulse duration, by estimates, at least twofold. To estimate the maximal
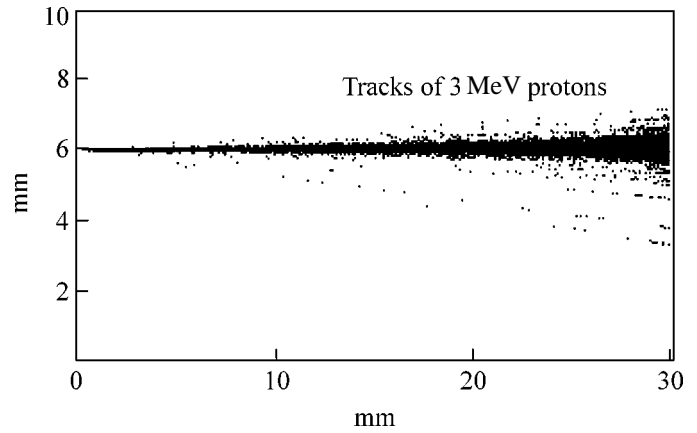
Fig. 4. Tracks of 5000 3-MeV protons incident on a 12-μm Be target at zero initial angle. Shown are the tracks from the entrance point at the target to the end point at the screen situated 3 cm behind the target.
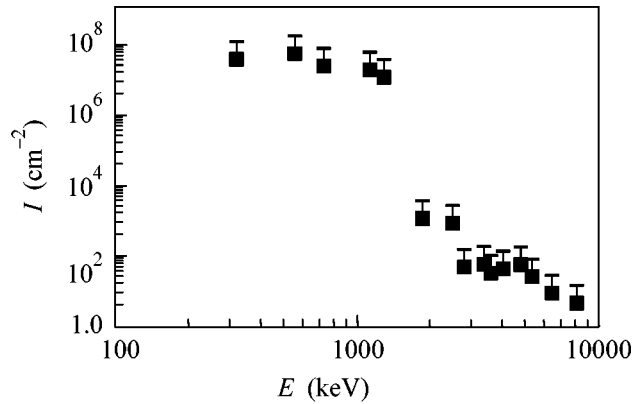
Fig. 5. Energy spectrum ((number of protons)/keV) of protons emitted from the face side of a 12-μm Be target.

energy of a fast ion, we use the well-known solution [16, 18]

$$\varepsilon_{i\;max} \approx 2Z\varepsilon_{eh}(\ln(2\omega_{pi}t_L))^2. \qquad (4)$$

The relation $\varepsilon_i \sim I_{18}^{0.5}$ that follows from Eq. (4) is corroborated by the numerical calculations and the experimental data [13]. The ions with energy exceeding (4) are few in number, so that the ion spectrum sharply breaks at energy (4) (so-called cutoff). Expression (4) for $Z = 1$ yields an estimate of 2.5 MeV, which corresponds to the maximal proton energy (2.3 MeV) at the rear side of the foil. The experimental energy spectrum of light ions at the face side of the target is shown in Fig. 5. The energy cutoff is clearly seen at 1.5 MeV. The fact that the ion energy at the face side is lower than energy (4) can be explained by the plasma-boundary smearing due to the prepulse, as a result of which the ambipolar field and the ion acceleration time decrease.

At times $t \gg R_b/v_i$ after charge relaxation, an extended plasma bunch is formed. On the way from the target to the detector, the angular distribution of emitted ions changes because of the plasma-cloud expansion by virtue of the Coulomb and thermal repulsion. The ion-beam emittance $\varepsilon_\mu(x) = R(x)dR/dx$ at distance x is given by the formula [14]

$$\varepsilon_\mu(x)$$
$$\approx R(x)\sqrt{4(J + c_s^2/v_i^2)\ln(R(x)/R(0)) + R'^2(0)}, \quad (5)$$

where $J = ZeJ_i(1 - K)/m_i v_i^3 \gamma_i^3$, $dR/dx|_{x=0} \approx v_{\perp i}/v_{\|i} \approx \theta_i$, $\gamma_i \approx 1$ is the ion Lorentz factor, $K = n_{eh}/Zn_i \leq 1$, $c_s = \sqrt{T_\perp/m_i}$, $J_i = Zen_iv_i\pi R_b^2$, and $R(0) = R_b$. Experimentally, the distribution of a fast-ion beam with a diameter of ≤ 0.6 mm was detected at a distance of 3 cm from the foil, which corresponds to the emittance of $\leq 0.1\pi$ mm mrad. Then, assuming that the beam charge is compensated ($K \approx 1$) and the initial exit angle is $\theta_i = 0$, one finds from Eq. (5) that the transverse ion temperature is restricted by $T_\perp \leq 200$ eV.

It is seen from the experimental results presented in this work that, under the action of an intense ($\geq 2 \times 10^{18}$ W/cm^2) laser pulse on the foil, light ions are accelerated to energies of ~2 MeV. The ion flow with an energy of ~2 MeV behind the target was much greater than the backflow of the same particles from the target. A high-intensity proton beam with an energy of ≥ 1.2 MeV and a very small divergence $\theta_i < 1°$ have been observed. This is likely caused by the fact that the interior part of a tubular ion beam is enriched with electrons and also that hydrogen is distributed inhomogeneously at the target surface. The theoretical estimates of ion energies and exit angles are close to their experimental values, suggesting that the ions are generated at the rear side of the foil.

REFERENCES

1. F. N. Beg, A. R. Bell, A. E. Dangor, *et al.*, Phys. Plasmas **4**, 447 (1997).

2. K. Krushelnick, E. L. Clark, M. Zepf, *et al.*, Phys. Plasmas **7**, 2055 (2000).

3. S. P. Hatchett, C. G. Brown, T. E. Cowan, *et al.*, Phys. Plasmas **7**, 2076 (2000).

4. M. H. Key, M. D. Cable, T. E. Cowan, *et al.*, Phys. Plasmas **5**, 1966 (1998).

5. A. Maksimchuk, S. Gu, K. Flippo, *et al.*, Phys. Rev. Lett. **84**, 4108 (2000).

6. A. P. Fews, P. A. Norreys, F. N. Beg, *et al.*, Phys. Rev. Lett. **73**, 1801 (1994).

7. S. Okihara, Y. Sentoku, K. Sueda, *et al.*, J. Nucl. Sci. Technol. **39**, 1 (2002).

8. M. Zepf, E. I. Clark, F. Beg, *et al.*, Phys. Rev. Lett. **90**, 064801 (2003).

9. V. Yu. Bychenkov, V. Rozmus, A. Maksimchuk, *et al.*, Fiz. Plazmy (Moscow) **27**, 1076 (2001) [Plasma Phys. Rep. **27**, 1017 (2001)].

10. V. G. Borodin, V. M. Komarov, V. A. Malinov, *et al.*, Kvantovaya Élektron. (Moscow) **29**, 101 (1999).

11. A. A. Andreev, V. M. Komarov, A. V. Charukhchev, *et al.*, Zh. Éksp. Teor. Fiz. **121**, 266 (2002) [JETP **94**, 222 (2002)].

12. A. Pukhov, Phys. Rev. Lett. **86**, 3562 (2001).

13. S. C. Wilks, A. B. Langdon, T. E. Cowan, *et al.*, Phys. Plasmas **8**, 542 (2001).

14. A. A. Andreev, T. Okada, K. Platonov, *et al.*, Laser Part. Beams (2003) (in press).

15. E. L. Clark, K. Krusheinick, J. Davies, *et al.*, Phys. Rev. Lett. **84**, 670 (2000).

16. P. Mora, Phys. Rev. Lett. **90**, 185002 (2003).

17. A. A. Andreev, Zh. Éksp. Teor. Fiz. **116**, 1184 (1999) [JETP **89**, 632 (1999)].

18. V. F. Kovalev, V. Yu. Bychenkov, and V. T. Tikhonchuk, JETP **95**, 226 (2002).

19. S. V. Bulanov, T. Esirkepov, F. F. Kamenets, *et al.*, Fiz. Plazmy (Moscow) **28**, 1059 (2002) [Plasma Phys. Rep. **28**, 975 (2002)].

20. Yu. M. Gorbulin, S. A. Dan'ko, Yu. G. Kalinin, *et al.*, Fiz. Plazmy (Moscow) **6**, 109 (1980) [Sov. J. Plasma Phys. **6**, 62 (1980)].

Translated by V. Sakun

Some Features in the Behavior of the Density of Superconducting Condensate in Superconductors

A. E. Karakozov[1], E. G. Maksimov[2, *], and A. V. Andrianova[3]

[1] *Vereshchagin Institute of High-Pressure Physics, Russian Academy of Sciences, Troitsk, Moscow region, 142090 Russia*
[2] *Lebedev Physical Institute, Russian Academy of Sciences, Moscow, 119991 Russia*
*e-mail: maksimov@lpi.ru
[3] *Physics Department, Moscow State University, Moscow, 119992 Russia*
Received January 30, 2004

The correlation between the density $\rho_s(T \longrightarrow 0)$ of superconducting condensate and the superconducting transition temperature T_c in underdoped HTSC systems is considered. It is shown that the linear relation between $\rho_s(0)$ and T_c observed in some experiments can easily be interpreted in the framework of the conventional Bardeen–Cooper–Schrieffer (BCS) model without invoking any exotic superconductivity models. © 2004 MAIK "Nauka/Interperiodica".

PACS numbers: 74.20.Fg; 74.25.Ha

Although high-temperature superconductivity in cuprates was discovered by Bednorz and Müller over 17 years ago [1], a consistent and generally accepted theory of this phenomenon has not been developed as yet. A considerable number of researchers involved in the theoretical studies consider cuprate compounds as systems with properties radically differing in every respect from those of traditional superconducting materials [2]. A critical analysis of the actual difference between the properties of cuprates and ordinary metals was given by one of the authors in the review [3], where it was rather convincingly proved that the properties of the normal state of optimally doped cuprates differ, if at all, from the properties of conventional metals quantitatively rather than qualitatively. In that review, the behavior of underdoped compounds was practically not considered, although it was noted that, at first glance, it could differ strongly from the properties of ordinary metals.

One such property of underdoped compounds, which is often treated as the clearest evidence of their substantial difference from standard metals [4], is the linear relation discovered by Uemura *et al.* [5, 6] between the density $\rho_s(T \longrightarrow 0)$ of the superconducting condensate and the superconducting transition temperature T_c:

$$\rho_s(0) = AT_c, \qquad (1)$$

where A is a certain quantity exhibiting a weak dependence on the doping level x. Relation (1), often referred to as the Uemura diagram in the literature, led to a large number of assumptions concerning the physical nature of this phenomenon. Among these assumptions, we can mention the existence of Bose–Einstein condensation of real electron pairs in underdoped compounds [6, 7],

the presence of strong superconducting fluctuations [8, 9], holon condensation in the model of spin and charge separation [8, 10], and so on.

In this brief communication, we will prove that relations analogous to the Uemura diagram may hold not only in the models of exotic superconducting systems but also in superconductors described by the Bardeen–Cooper–Schrieffer (BCS) model. The necessary condition for this is the existence of a mechanism destroying the superconductivity. For superconductors with *s* pairing, such a mechanism has been well known for a long time [11] and is associated with the addition of magnetic impurities. In BCS superconductors with *d* pairing, the potential scattering from ordinary nonmagnetic impurities plays the same role [12]. The density ρ_s of superconducting electrons is usually determined in terms of λ (inverse square of the magnetic-field penetration depth), because
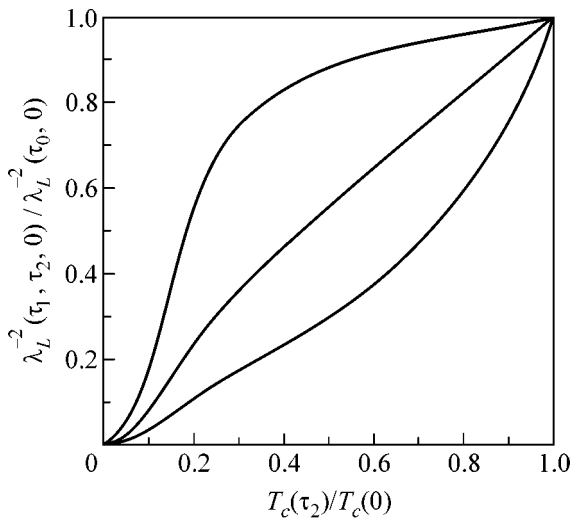
$$\rho_s(T) \sim \lambda^{-2}(T). \qquad (2)$$

In the BCS model, the quantity $\lambda^{-2}(T)$ can be written for both types of pairing in the form [12]

$$\lambda^{-2}(T) = \frac{\omega_{pl}^2}{4\pi}\int_0^\infty d\omega \tanh\frac{\omega}{2T}\left\langle \mathrm{Re}\left\{\frac{\tilde{\Delta}_\varphi^2(\omega)}{\tilde{\varepsilon}_\varphi^3(\omega)}\right\}\right\rangle, \qquad (3)$$

$$\tilde{\varepsilon}_\varphi = \sqrt{\tilde{\omega}_\varphi^2(\omega) - \tilde{\Delta}_\varphi^2(\omega)}, \qquad (4)$$

where ω_{pl} is the plasma frequency. Functions $\tilde{\Delta}_\varphi(\omega)$ (superconducting order parameter) and $\tilde{\omega}_\varphi(\omega)$ (frequency renormalized due to the interaction with impurities) satisfy the BCS equations with impurities; the

Fig. 1. The density $\rho_s(\tau_1, \tau_2, 0) = \lambda^{-2}(\tau_1, \tau_2, 0)/\lambda^{-2}(\tau_0, 0)$ of superconducting condensate at zero temperature versus the superconducting transition temperature $T_c(\tau_2)/T_c(0)$ in a BCS superconductor with magnetic impurities.

angular brackets stand for the averaging over the angle φ. In pure superconductors, we have

$$\tilde{\omega}_\varphi(\omega) = \omega, \tag{5}$$

$$\tilde{\Delta}_\varphi(\omega) = \begin{cases} \Delta(T) \\ \Delta(T)\cos 2\varphi \end{cases} \quad \text{for } s \text{ and } d \text{ pairing.} \tag{6}$$

(In expression (6), the simplest form of $\tilde{\Delta}_\varphi(\omega)$ is used for d pairing in a quasi-two-dimensional BCS superconductor with a cylindrical Fermi surface.)

Let us first consider the correlation between $\rho_s(0)$ and T_c in a superconductor with magnetic impurities in the BCS model. For a BCS superconductor with ordinary s pairing in the presence of magnetic and nonmagnetic impurities, functions $\tilde{\Delta}_\varphi(\omega)$ and $\tilde{\omega}_\varphi(\omega)$ satisfy the equations [11]

$$\tilde{\omega} = \omega + i\frac{1}{2}\left(\frac{1}{\tau_1} + \frac{1}{\tau_2}\right)\frac{\tilde{\omega}}{\sqrt{\tilde{\omega}^2 - \tilde{\Delta}^2}}, \tag{7}$$

$$\tilde{\Delta} = \Delta + i\frac{1}{2}\left(\frac{1}{\tau_1} - \frac{1}{\tau_2}\right)\frac{\tilde{\Delta}}{\sqrt{\tilde{\omega}^2 - \tilde{\Delta}^2}}, \tag{8}$$

while quantity Δ is self-consistently defined by the standard BCS equation,

$$\Delta = N(0)V \int\limits_0^{\omega_D} d\omega \tanh\frac{\omega}{T} \mathrm{Re}\left\{\frac{\tilde{\Delta}}{\sqrt{\tilde{\omega}^2 - \tilde{\Delta}^2}}\right\}, \tag{9}$$

where V is the BCS s interaction, $N(0)$ is the density of states at the Fermi surface, $1/\tau_1$ is the reciprocal relax-

ation time associated with the potential scattering from ordinary impurities, and $1/\tau_2$ is the reciprocal relaxation time associated with the exchange scattering from magnetic impurities with spin flip. The system of Eqs. (7), (8) with the substitution $\tilde{\Delta} = (\tilde{\omega}/\omega)\bar{\Delta}$ can be reduced to the Abrikosov–Gor'kov algebraic equations [11]

$$\bar{\Delta} = \Delta - i\frac{1}{\tau_2}\frac{\bar{\Delta}}{\sqrt{\omega^2 - \bar{\Delta}^2}}, \tag{10}$$

$$\tilde{\omega} = \omega + i\frac{1}{2}\left(\frac{1}{\tau_1} + \frac{1}{\tau_2}\right)\frac{\omega}{\sqrt{\omega^2 - \bar{\Delta}^2}}, \tag{11}$$

where Δ is defined as

$$\Delta = N(0)V \int\limits_0^{\omega_D} d\omega \tanh\frac{\omega}{2T} \mathrm{Re}\left\{\frac{\bar{\Delta}}{\sqrt{\omega^2 - \bar{\Delta}^2}}\right\}. \tag{12}$$

It follows from these equations that the elastic scattering from impurities does not affect Δ and T_c.

Figure 1 shows the calculated curves describing the correlation between the quantities λ^{-2} and T_c in this model. The middle curve in the figure corresponds to the case of an initially "dirty" superconductor, for which the reciprocal time $1/\tau_0$ of electron relaxation at impurities satisfies the condition

$$\frac{1}{\tau_0} \gg \Delta_0(0) > 2\frac{1}{\tau_2}, \tag{13}$$

where $\Delta_0(0)$ is the energy gap in a pure superconductor at zero temperature. In this case, in the "gap" concentration region of magnetic impurities $[\tau_2\Delta(\tau_2, 0)]^{-1} \leq 1$ (which constitutes practically the entire range of their concentrations), a linear correlation takes place, because magnetic impurities in a dirty superconductor (13) do not directly affect its kinetic properties. In this case, the quantity λ^{-2} can be written as [13]

$$\lambda^{-2}(\tau_1, \tau_2) \approx (2\pi)^2\sigma_n\Delta(\tau_2, 0), \tag{14}$$

while both quantities $T_c(\tau_2)$ and $\Delta(\tau_2, 0)$ in the gap region $[\tau_2\Delta(\tau_2, 0)]^{-1} \leq 1$, as is known [11], are linear functions of $1/\tau_2$. It is clearly seen from Fig. 1 that the deviation from the linear dependence of $\lambda^{-2}(\tau_1, \tau_2)/\lambda^{-2}(\tau_0)$ on $T_c(\tau_2)/T_c(0)$ in a dirty superconductor is observed only in the "gapless" region at a high concentration of magnetic impurities (i.e., at small values of $T_c(\tau_2)/T_c(0))$. The upper curve describes the dependence of $\lambda^{-2}(\tau_2)/\lambda^{-2}$ on $T_c(\tau_2)/T_c(0)$ for a "clean" superconductor (i.e., in the absence of nonmagnetic scattering). The lower curve corresponds to the originally clean ($1/\tau_0 = 0$) superconductor with magnetic impurities, for which the ratio of potential- and exchange-scattering amplitudes is

$$\tau_2/\tau_1 = 10. \tag{15}$$

Thus, we see that various types of relations between the density of superconducting electrons and the superconducting transition temperature (including the Uemura diagram) are possible even in the simplest BCS model with s pairing.

Let us now consider a BCS d superconductor with impurities. The equations for functions $\tilde{\Delta}_\varphi(\omega)$ and $\tilde{\omega}_\varphi(\omega)$ appear in this case in a more complicated form [12], as compared to Eqs. (6) and (7),

$$\tilde{\Delta}_\varphi(\omega) = \Delta_\varphi + i\frac{1}{\tau_n}$$
$$\times \frac{\langle g_1(\varphi, \omega)\rangle}{\cos^2\delta_n + \sin^2\delta_n(\langle g_0(\varphi, \omega)\rangle^2 - \langle g_1(\varphi, \omega)^2\rangle)}, \quad (16)$$

$$\tilde{\omega}_\varphi = \omega + i\frac{1}{\tau_n}$$
$$\times \frac{\langle g_0(\varphi, \omega)\rangle}{\cos^2\delta_n + \sin^2\delta_n(\langle g_0(\varphi, \omega)\rangle^2 - \langle g_1(\varphi, \omega)^2\rangle)}, \quad (17)$$

where

$$g_0(\varphi, \omega) = \frac{\tilde{\omega}_\varphi(\omega)}{\sqrt{\tilde{\omega}_\varphi^2(\omega) - \tilde{\Delta}_\varphi^2(\omega)}}, \quad (18)$$

$$g_1(\varphi, \omega) = \frac{\tilde{\Delta}_\varphi(\omega)}{\sqrt{\tilde{\omega}_\varphi^2(\omega) - \tilde{\Delta}_\varphi^2(\omega)}}. \quad (19)$$

In Eqs. (16) and (17), $1/\tau_n$ is the reciprocal relaxation time on impurities in the normal state,

$$\frac{1}{\tau_n} = n_{imp}\frac{\pi N(0)V_{imp}}{1 + [\pi N(0)V_{imp}]^2} \equiv \frac{n_{imp}}{\pi N(0)}\sin^2\delta_n, \quad (20)$$

where n_{imp} is the impurity concentration, V_{imp} is the impurity scattering potential, and $\delta_n = \arctan[\pi N(0)V_{imp}]$ is the scattering phase. The self-consistent equation has the form
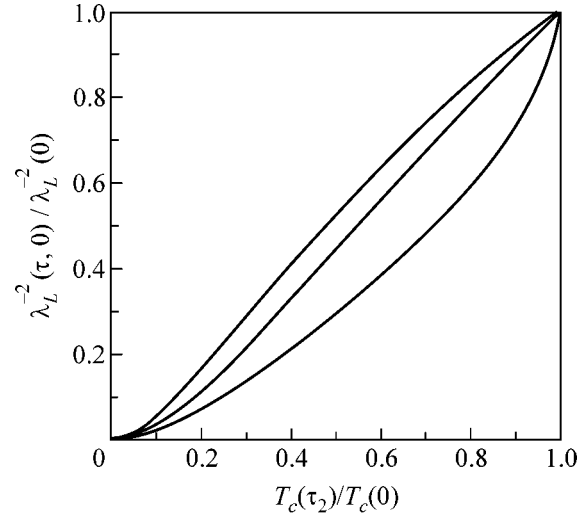
$$\Delta_\varphi = N(0)\int_0^{\omega_D} d\omega \tanh\frac{\omega}{2T}\mathrm{Re}\langle V(\varphi, \varphi')g_1(\varphi', \omega)\rangle. \quad (21)$$

In our calculations, we used the simplest expression for the electron–electron interaction resulting in the d pairing:

$$V(\varphi, \varphi') = \cos 2\varphi V\cos 2\varphi'. \quad (22)$$

In this case, we can seek the solution in the form $\tilde{\Delta}_\varphi(\omega) = \Delta\cos 2\varphi$; in this case, $\langle g_1\rangle = 0$ and Eqs. (15) and (16) have the form

$$\Delta = N(0)V\int_0^{\omega_D} d\omega \tanh\frac{\omega}{2T}\mathrm{Re}\langle g_1(\varphi, \omega)\cos 2\varphi\rangle, \quad (23)$$

Fig. 2. The density $\rho_s(\tau, 0) = \lambda^{-2}(\tau, 0)/\lambda^{-2}(0)$ of superconducting condensate at zero temperature vs. the superconducting transition temperature $T_c(\tau)/T_c(0)$ in a BCS superconductor with d pairing.

$$\tilde{\omega} = \omega + i\frac{1}{\tau_n}\frac{\langle g_0(\varphi, \omega)\rangle}{\cos^2\delta_n + \sin^2\delta_n\langle g_0(\varphi, \omega)\rangle^2}. \quad (24)$$

The results of our calculations for this model are illustrated in Fig. 2. The upper curve in this figure is obtained in the Born approximation. The lower curve corresponds to the unitary strong-scattering limit ($\delta_n = \pi/2$), while the middle curve describes the intermediate case. The correlation between $\lambda^{-2}(\tau)$ and $T_c(\tau)$ in a BCS superconductor with d pairing, in which superconductivity is suppressed by the ordinary nonmagnetic impurities, resembles, to a considerable extent, the situation in a conventional BCS s superconductor with magnetic impurities. In this case, various types of the dependence of $\lambda^{-2}(\tau)$ on T_c (including a near-linear dependence) are possible. Thus, the Uemura-type dependence of the density of superconducting condensate on T_c takes place in the simplest BCS systems and there is no need to invoke any exotic superconductivity mechanisms for its explanation.

Turning back to the discussion of the density of superconducting condensate in underdoped HTSC compounds, we can make the following remarks. First, the rather convincing experimental data obtained recently in [13, 14] indicate that the quasiparticle excitations in the HTSC systems can be described by the Bogoliubov combination of electron–hole pairs [15]. This, in turn, means that the superconducting state of cuprates differs only slightly from the state described by the BCS model. Second, there is convincing evidence, obtained by tunneling measurements [16], that the ratio $2\Delta/T_c$ remains virtually unchanged over a wide range of doping from underdoped to overdoped states. This may imply that the superconductivity mechanism

depends weakly on the doping level, but certain superconductivity suppression mechanisms arise or intensify in the system upon the deviation from the optimal doping level. We proved above, by the example of the effect of various impurities, that the processes of superconductivity destruction not affecting the pairing mechanism can lead to the T_c dependence of the density of superconducting condensate. This dependence can both coincide with the Uemura diagram and substantially differ from it. In recent publication [17], doubts were cast upon the experimental observation of the Uemura rule (i.e., a linear dependence of $\rho_s(0)$ on T_c) in underdoped systems. A similar conclusion was drawn recently in [18] on the basis of the direct measurements of the magnetic-field penetration depth in the HTSC systems over a wide doping range. The dependence of $\rho_s(0)$ on T_c obtained in [17] (see Fig. 1 in that paper) is similar, to a considerable extent, to the dependence obtained by us for the unitary limit of scattering from individual impurities.

Although the HTSC (in particular, underdoped) compounds belong to defect structures, we do not state that the Uemura diagram or any other dependence of $\rho_s(0)$ on T_c (see [17, 18]) is due to the destruction of superconductivity in HTSC systems as a result of the scattering from isolated impurities. Rather, as was emphasized in [14], the mechanism (or mechanisms) of pair breaking in such materials differs from the action of individual impurities and has a more complicated character associated with some nanoscale disorder. According to [17, 18], the T_c dependence of $\rho_s(0)$ can also be due to the superconductivity destruction upon a decrease in the doping level and appearance of a pseudogap in the system. It remains unclear whether the appearance of the pseudogap is associated with the nanoscale disordering observed in [14] or not.

In conclusion, it should be emphasized that the Uemura diagram (i.e., linear T_c dependence of $\rho_s(0)$) is not at all an indication of the existence of some exotic superconductivity mechanisms in the HTSC systems. A similar behavior can also be observed in the traditional superconductors described by the BCS model with s and d pairing. In our opinion, further detailed experimental investigation of this problem in various HTSC systems is highly important for establishing the possible similarity or difference in the behavior of $\rho_s(0)$ and T_c in these systems. This will give a clearer idea of the superconductivity destruction mechanisms in such systems upon a deviation from the optimal doping level and, probably, of the nature of high-temperature superconductivity itself.

REFERENCES

1. J. G. Bednorz and K. A. Müller, Z. Phys. B **64**, 189 (1986).
2. P. W. Anderson, *The Theory of Superconductivity* (Princeton Univ. Press, Princeton, 1997).
3. E. G. Maksimov, Usp. Fiz. Nauk **170**, 1033 (2000) [Phys. Usp. **43**, 965 (2000)].
4. P. A. Lee and X.-G. Wen, Phys. Rev. Lett. **78**, 4111 (1997).
5. Y. J. Uemura, G. M. Luke, B. J. Sternlieb, *et al.*, Phys. Rev. Lett. **62**, 2317 (1989).
6. Y. J. Uemura, L. P. Le, G. M. Luke, *et al.*, Phys. Rev. Lett. **66**, 2665 (1991).
7. M. Randeria, N. Trivedi, A. Morko, and R. T. Scalettar, Phys. Rev. Lett. **69**, 2001 (1992).
8. V. Emery and S. Kivelson, Nature **374**, 434 (1995).
9. Q. Chen, I. Kosztin, B. Janko, and K. Levin, Phys. Rev. Lett. **81**, 4708 (1998).
10. N. Nagaosa and P. A. Lee, Phys. Rev. Lett. **64**, 2450 (1990).
11. A. A. Abrikosov and L. P. Gor'kov, Zh. Éksp. Teor. Fiz. **39**, 1781 (1960) [Sov. Phys. JETP **12**, 1243 (1960)].
12. S. Hensen, G. Müller, C. T. Rieck, and K. Scharnberg, Phys. Rev. B **56**, 6237 (1997).
13. K. McElroy, R. W. Simmonds, J. E. Hoffman, *et al.*, Nature **422**, 592 (2003).
14. H. Matsui, T. Sato, T. Takahashi, *et al.*, Phys. Rev. Lett. **90**, 217002 (2003).
15. N. N. Bogolyubov, V. V. Tolmachev, and D. V. Shirkov, *A New Method in the Theory of Superconductivity* (Akad. Nauk SSSR, Moscow, 1958; Consultants Bureau, New York, 1959).
16. E. G. Maksimov and Ya. G. Ponomarev, Pis'ma Zh. Éksp. Teor. Fiz. **76**, 455 (2002) [JETP Lett. **76**, 394 (2002)].
17. J. L. Tallon, J. W. Loram, J. R. Cooper, *et al.*, Phys. Rev. B **68**, 180501 (2003).
18. M. R. Trunin, Yu. A. Nefedov, and A. M. Shevchun, Phys. Rev. Lett. **92**, 067006 (2004).

Translated by N. Wadhwa

Elemental Composition of Nanoclusters Formed by Pulsed Irradiation with Low-Energy Ions during Ge/Si Epitaxy

A. V. Dvurechenskiĭ*, Zh. V. Smagina, V. A. Zinov'ev, V. A. Armbrister, V. A. Volodin, and M. D. Efremov

Institute of Semiconductor Physics, Siberian Division, Russian Academy of Sciences, Novosibirsk, 630090 Russia
*e-mail: dvurech@isp.nsc.ru
Received February 24, 2004

Multilayer silicon structures with built-in layers of Ge nanoclusters were studied experimentally by Raman light scattering. The built-in layers were formed by the pulsed action of a low-energy beam of intrinsic ions during molecular-beam epitaxy. It is found that the ion-stimulated nucleation and the subsequent growth make it possible to obtain Ge nanoclusters almost free of Si. © *2004 MAIK "Nauka/Interperiodica"*.

PACS numbers: 81.15.Hi; 68.55.-a; 61.80.Jh; 81.07.-b

At present, the most promising method of quantum-dot (QD) array formation is based on the effects of self-organization of semiconductor nanostructures in heteroepitaxial systems [1–4]. The deposition of a material with a lattice constant differing substantially from the substrate lattice parameter induces elastic strains in the epitaxial film and in the islands on its surface. These strains are the key factor in both the morphological transition from a flat to the islanding film (Stranski–Krastanov mechanism) and the subsequent changes in sizes, shape, and spatial distribution of islands, providing, under certain conditions, the formation of an array of coherently strained nanometer-sized islands.

The problem of the controlled formation of QD arrays is associated with the necessity of creating new promising devices such as quantum transistors, high-speed memory elements, narrow-band light-emitting diodes, heterolasers with radiation of a required color, and infrared photodetectors. In order to realize the unique characteristics of new devices in practice, it is necessary to maintain a high density of QDs. In combination with the requirement for small QD sizes (<10 nm), the layer density must be on the order of 10^{12} cm^{-2} (at higher densities, QDs of the indicated size are joined together into a continuous layer).

The authors of [4] developed a method for the low-temperature molecular-beam epitaxy (MBE) of Ge on Si(100) that provides the formation of nanosized islands with a surface density of $(3–5) \times 10^{11}$ cm^{-2}. The average size of pyramidal Ge clusters was 15 nm (pyramid base), the pyramid height was 1.5 nm, and the size inhomogeneity was no worse than 17%. The typical conditions for the formation of Ge/Si structures included the processes of homoepitaxy on Si(100) at 700°C with a rate of 1–2 monolayers (MLs) per second,

Ge heteroepitaxy at 300°C (0.2 ML/s), and Si epitaxy over the Ge islands at 500°C. A sufficiently low temperature in the deposition of Ge and in the subsequent overgrowth of the Si layer ensured the suppression of the process of mixing between two materials; as a result, the Ge nanoclusters practically did not contain Si [5].

The method proposed by us for the controlled formation of a QD array consists in the pulsed irradiation by low-energy (~100 eV) intrinsic ions during the heteroepitaxy at certain instants of time according to the degree of monolayer filling [6–8]. We found that the irradiation with low-energy Ge ions during Ge heteroepitaxy on silicon led to the stimulated nucleation of Ge islands and to a decrease in the critical thickness of the pseudomorphic Ge film, at which a transition from two-dimensional layer-by-layer growth to three-dimensional growth takes place. In this case, the average size of three-dimensional (3D) Ge islands decreases, their density increases, and the mean-square deviation from the average value decreases as compared with the corresponding values for molecular-beam epitaxy (the effect of self-organization of an ensemble of Ge nanoclusters upon pulsed irradiation with low-energy ions during heteroepitaxy).

Because the ion irradiation can stimulate the mixing process for dissimilar materials [9], the final elemental composition of QDs in the formed Ge/Si nanostructures remained unclear.

This work is devoted to determining the elemental composition of QDs using Raman scattering in the structures formed as a result of the effect of self-organization of an ensemble of nanoclusters upon pulsed irradiation by low-energy ions during Ge heteroepitaxy on Si(100).
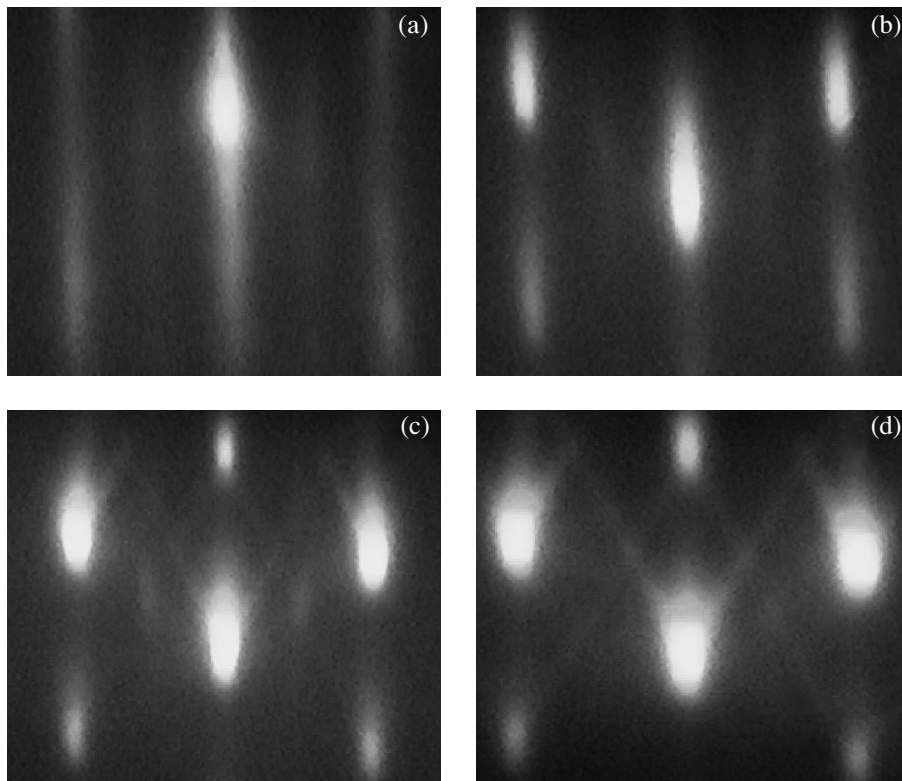
Fig. 1. Diffraction patterns obtained during (a) and (c) conventional Ge/Si(100) heteroepitaxy without ion irradiation and (b) and (d) heteroepitaxy with pulsed (0.5 s) irradiation by low-energy (≈100 eV) Ge⁺ ions; the substrate temperature was 350°C; two effective thicknesses of the deposited Ge were used: (a) and (b) 5 ML and (c) and (d) 7 ML.

The samples to be studied were grown in an MBE system with a built-in ion-molecular source of germanium (for more detail, see [6, 7]). The Ge/Si structures were formed by two methods: (1) Ge MBE on Si and (2) pulsed (with a duration of 0.5 s) irradiation with Ge^+ ions with an energy of about 100 eV during Ge MBE on Si. The pulses were supplied at instants of time corresponding to the deposition of each Ge monolayer. The Ge deposition rate was 0.1 ML/s (1 ML = 6.8 × 10^{14} atom/cm²), the Si deposition rate was 1.2 ML/s, and the substrate temperature was 350°C.

Each method was used to grow structures of two types differing in the amount of the deposited germanium (5 and 7 ML). A Si layer 50-nm thick was grown over the deposited Ge film, and this procedure of sequential Ge/Si growth was repeated ten times. The final capping Si layer was grown to a thickness of 100 nm at a temperature of 500°C.

The thickness and morphology of the deposited films was controlled by reflection high-energy electron diffraction (RHEED). The selection of the two values of the deposited Ge amount (5 and 7 ML) was based on the RHEED data. When 5 ML of Ge were deposited by MBE, three-dimensional Ge islands were not yet formed (Fig. 1a). Under the same growth conditions, pulsed ion irradiation leads to the formation of 3D islands on the Ge/Si surface (Fig. 1b). For thicker layers

of deposited Ge (7 ML), the islands form even in the conventional MBE. Therefore, the diffraction patterns from Ge films formed by both methods show virtually no difference, and, according to the RHEED data, a transition from the growth of 3D islands in the form of hut clusters to the growth of islands in the form of dome clusters is observed (Figs. 1c, 1d).

The samples were studied using Raman spectroscopy. The multilayer character of the Ge/Si structure provided a sufficient intensity of the Raman signal. The spectra were recorded at room temperature using an automated setup based on a DFS-52 spectrometer. An Ar^+ laser ($\lambda = 514.5$ nm) was used as the source of excitation. The Raman experiments were carried out in the quasi-backscattering geometry. The following polarization geometry was used in the scattering experiments: the polarization vector of the incident radiation was directed along the crystallographic ⟨100⟩ direction of the structures, and the scattered light was detected in the ⟨010⟩ polarization. This allowed us to avoid the complications in the interpretation of Raman spectra considered in [10].

The experimental Raman spectra are presented in Fig. 2. Each spectrum shows a peak positioned in the range from 307 to 315 cm⁻¹, which corresponds to the Raman scattering by the optical vibrations of the Ge–Ge bonds. A decrease in the thickness of the Ge layer

shifts this peak toward lower frequencies, whereas the mechanical compressions lead to a shift of the peak toward higher frequencies. All peaks exhibit a low-frequency wing due to the contributions from both the higher-order localized modes and the wetting Ge layer. The peaks observed in the range from 370 to 430 cm^{-1} correspond to the Raman scattering by the optical vibrations of the Ge–Si bonds [10, 11].

The characteristics of the Ge–Si nanostructures were determined on the basis of the Raman data using numerical calculations of the fundamental frequencies and modes in the Born–von Karman approximation. The Ge–Ge elastic constants were determined by comparing the experimental data with the calculated phonon dispersions in bulk germanium [12]. The Raman spectra were calculated from these data using the Wolkenstein model of additive bond polarizabilities [13]. The calculation was performed within the framework of a one-dimensional approximation, because the lateral sizes of three-dimensional islands formed during Ge/Si(100) heteroepitaxy are usually much larger than their height. It follows from the calculations that the Raman-active Ge–Ge frequencies decrease with decreasing thickness of the germanium layer. In the case of a flat (unstrained) Ge layer, the frequency of the main Ge–Ge peak is 290 cm^{-1} for a thickness of 5 ML, 294 cm^{-1} for a thickness of 7 ML, and 298 cm^{-1} for a thickness of 10 ML.

Mechanical strains were not considered in the calculation, but their effect can be taken into account by shifting all frequencies by a value proportional to the strains, as was done in [14, 15]. According to our estimates, the shift of the Ge–Ge Raman peak as a result of the mechanical strains in Ge islands elastically strained in Si (because of a difference of 4.2% in lattice constants) reaches 17 cm^{-1} with respect to the frequency of the optical phonon in the unstrained bulk Ge (302 cm^{-1}). In the structures with an effective Ge thickness of 5 ML grown by the conventional MBE, the peak is located at 307.5 cm^{-1} (Fig. 2). The vibrational frequency calculated for an unstrained Ge film uniform in depth equals 290 cm^{-1} for a thickness of 5 ML. The high-frequency shift of 17.5 cm^{-1} is in good agreement with the estimates given for a strained structure and with the RHEED data, which point to the absence of 3D Ge islands.

In the spectra of the samples with the same average thickness of the deposited germanium grown by MBE with pulsed ion irradiation, the peak of the Raman signal of the Ge–Ge bonds is located at 315 cm^{-1}. In this case, the difference between the experimental and calculated peak positions is 25 cm^{-1}. This is considerably larger than the highest possible shift caused by the effects of compression strains (17 cm^{-1}). Such a shift cannot be interpreted as the effect of mechanical strains. Evidently, the germanium layer in this case is not two-dimensional but contains 3D islands in which
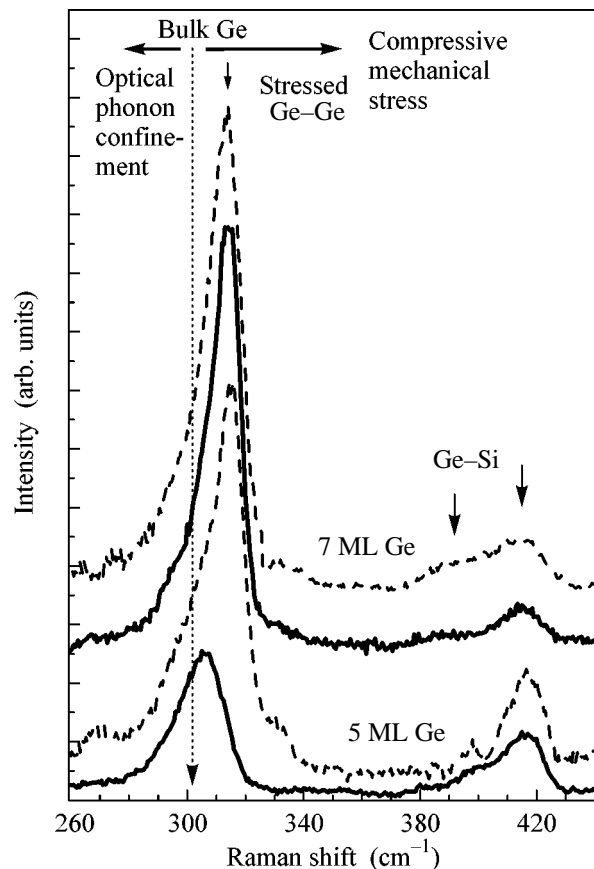
Fig. 2. Raman spectra of multilayer Ge/Si heterostructures for two thicknesses of the deposited Ge: 5 and 7 ML. The solid line corresponds to the structures obtained by the conventional MBE, and the dashed line corresponds to the structures obtained by the MBE with pulsed ion irradiation.

the thickness of germanium is much larger than the average thickness, in agreement with the RHEED data. The variation of the position and shape of diffraction reflections under conditions of growth with pulsed ion irradiation corresponds to the appearance of three-dimensional islands shaped as hut clusters (Fig. 1b).

In this case, according to the STM and RHEED data [8], the overall height of the 3D islands and the wetting Ge underlayer makes up about 10 ML. For the island structure of such sizes, the calculated peak position equals 298 cm^{-1}. The difference between the calculated and experimental peak positions is 17 cm^{-1}, which is close to the maximum possible shift due to mechanical strains. This result indicates that the plastic relaxation of mechanical strains is absent in the 3D islands obtained under the ion-irradiation conditions.

As the average thickness of the deposited germanium increases to 7 ML, the Raman spectral differences between the samples grown under conditions of pulsed irradiation by Ge^{+} ions and by the conventional MBE virtually disappear (Fig. 2), which agrees with the RHEED data (Figs. 1c, 1d). The small displacement of

the Raman peak from the Ge–Ge bonds toward the value corresponding to the bulk material, as compared to the Raman peak in the structures with a thickness of 5 ML grown under pulsed action, is, evidently, associated with a partial relaxation of strains by approximately 10–20% (Fig. 2).

The amounts of germanium in the structures under study were estimated from the ratio of peak intensities for the Si–Ge and Ge–Ge bonds. In the samples with an effective thickness of 5 ML grown by the conventional molecular-beam epitaxy, the ratio of integral peak intensities (I_{SiGe}/I_{GeGe}) equals 0.43. For the structures with the same average thickness of the deposited germanium obtained under pulsed ion-irradiation conditions, the I_{SiGe}/I_{GeGe} ratio decreases to 0.2. As the effective film thickness increases to 7 ML, the Raman intensities for the optical Si–Ge vibrations further decrease, compared to the peak intensities for the Ge–Ge bonds (Fig. 2). Based on the ratio of the Si–Ge and Ge–Ge peak intensities, the ratio of the amounts of the silicon and germanium bonds (N_{SiGe}/N_{GeGe}) in the layers is estimated as

$$\frac{I_{SiGe}}{I_{GeGe}} \simeq B \frac{N_{SiGe}}{N_{GeGe}}, \tag{1}$$

where $B \approx 3.2$ (see [11, 16]).

In the structures with an effective thickness of 5 ML grown under pulsed ion-irradiation conditions, the N_{SiGe}/N_{GeGe} ratio equals 0.64. In the structures with an effective thickness of 7 ML, this ratio decreases to 0.5. The fractional Ge content χ was estimated from the ratio of the number of bonds. For the structures grown from an ion-molecular beam, $\chi > 0.75$. The Ge islands reside in the Si environment, and the Si–Ge bonds at the phase boundary can contribute to N_{SiGe}; therefore, the above estimate is the lower limit of the Ge content. The obtained value of N_{SiGe}/N_{GeGe} can be compared with the ratio of the number of bonds in a model structure containing Ge islands ($\chi = 1$) shaped as hut clusters built-in in a silicon matrix. The lateral size of the islands was chosen equal to 10 nm, the height was 1 nm, the effective thickness of the Ge layer was 5 ML, the thickness of the wetting layer was 3 ML, and the island density was 10^{12} cm^{-2}. In this case, the N_{SiGe}/N_{GeGe} ratio equals 0.52. The obtained value for the chosen model structure proved to be rather close to the experimental values. Thus, the comparison of the experimental and calculated results allows the suggestion that the Ge nanoclusters in the heterostructures obtained by ion-molecular beam epitaxy contain almost no Si.

An important conclusion from the results obtained in this work is that the pulsed ion irradiation during the growth of Ge/Si structures does not lead to a significant mixing of the Ge and Si layers. The germanium content in the three-dimensional islands obtained by the conventional epitaxy and epitaxy with ion irradiation practically proved to be similar.

REFERENCES

1. Zh. I. Alferov, Fiz. Tekh. Poluprovodn. (St. Petersburg) **32**, 317 (1998) [Semiconductors **32**, 1 (1998)].

2. N. N. Ledentsov, V. M. Ustinov, V. A. Shchukin, *et al.*, Fiz. Tekh. Poluprovodn. (St. Petersburg) **32**, 385 (1998) [Semiconductors **32**, 343 (1998)].

3. N. V. Vostokov, S. A. Gusev, I. V. Dolgov, *et al.*, Fiz. Tekh. Poluprovodn. (St. Petersburg) **34**, 8 (2000) [Semiconductors **34**, 6 (2000)].

4. O. P. Pchelyakov, Yu. B. Bolkhovityanov, A. V. Dvurechenskiĭ, *et al.*, Fiz. Tekh. Poluprovodn. (St. Petersburg) **34**, 1281 (2000) [Semiconductors **34**, 1229 (2000)].

5. S. B. Érenburg, N. V. Bausk, A. V. Nenashev, *et al.*, Zh. Strukt. Khim. **41**, 890 (2000).

6. A. V. Dvurechenskiĭ, V. A. Zinov'ev, V. A. Kudryavtsev, and Zh. V. Smagina, Pis'ma Zh. Éksp. Teor. Fiz. **72**, 190 (2000) [JETP Lett. **72**, 131 (2000)].

7. A. V. Dvurechenskiĭ, V. A. Zinov'ev, and Zh. V. Smagina, Pis'ma Zh. Éksp. Teor. Fiz. **74**, 296 (2001) [JETP Lett. **74**, 267 (2001)].

8. A. V. Dvurechenskii, J. V. Smagina, A. V. Zinovyev, *et al.*, in *Proceedings of 11th International Symposium on Nanostructures: Physics and Technology*, Ed. by Zh. Alferov and L. Esaki (Ioffe Physicotechnical Inst., St. Petersburg, 2003).

9. J. Gyulai, in *Ion Implantation: Science and Technology*, Ed. by J. F. Ziegler, 2nd ed. (Academic, Boston, 1988), p. 93.

10. A. V. Kolobov, J. Appl. Phys. **87**, 2926 (2000).

11. P. H. Tan, K. Brunner, D. Bougeard, and G. Abstreiter, Phys. Rev. B **68**, 125302 (2003).

12. G. Nelin and G. Nilsson, Phys. Rev. B **5**, 3151 (1972).

13. M. Wolkenstein, C. R. Acad. Sci. USSR **32**, 185 (1941).

14. F. Cerdeira, C. J. Buchenauer, F. H. Pollak, and M. Cardona, Phys. Rev. B **5**, 580 (1972).

15. J. Groenen, R. Carles, S. Christiansen, *et al.*, Appl. Phys. Lett. **71**, 3856 (1997).

16. P. M. Mooney, F. Dacol, J. C. Tsang, and J. O. Chu, Appl. Phys. Lett. **62**, 2069 (1993).

Translated by A. Bagatur'yants

Superconductivity on the Localization Threshold and Magnetic-Field-Tuned Superconductor–Insulator Transition in TiN Films[¶]

T. I. Baturina[1], *, D. R. Islamov[1], J. Bentner[2], C. Strunk[2], M. R. Baklanov[3], and A. Satta[3]

[1] *Institute of Semiconductor Physics, Novosibirsk, 630090 Russia*
[2] *Institut für Experimentelle und Angewandte Physik, Universität Regensburg, D-93025 Regensburg, Germany*
[3] *Independent Microelectronic Center, B-3001 Leuven, Belgium*
*e-mail: tatbat@isp.nsc.ru
Received September 11, 2003; in final form, February 25, 2004

Temperature- and magnetic-field-dependent measurements of the resistance of ultrathin superconducting TiN films are presented. The analysis of the temperature dependence of the zero-field resistance indicates an underlying insulating behavior, when the contribution of Aslamazov–Larkin fluctuations is taken into account. This demonstrates the possibility of the coexistence of the superconducting and insulating phases and of a direct transition from the one to the other. The scaling behavior of magnetic field data is in accordance with a superconductor–insulator transition (SIT) driven by quantum phase fluctuations in two-dimensional superconductor. The temperature dependence of the isomagnetic resistance data on the high-field side of the SIT has been analyzed, and the presence of an insulating phase is confirmed. A transition from the insulating to a metallic phase is found at high magnetic fields, where the zero-temperature asymptotic value of the resistance is equal to h/e^2. © 2004 MAIK "Nauka/Interperiodica".

PACS numbers: 74.78.Db; 74.40.+k; 71.30.+h; 74.25.-q

The interplay between superconductivity and localization is a phenomenon of fundamental interest, and the question of the nature of superconductivity and its evolution in two-dimensional disordered systems and a perpendicular magnetic field continues to receive a great deal of theoretical and experimental attention. Two-dimensional systems are of special interest as two is the lower critical dimensions for both localization and superconductivity. Two ground states are expected to exist for bosons at $T = 0$: a superconductor with long-range phase coherence and an insulator in which the quantum-mechanical correlated phase is disjointed. The zero-temperature superconductor–insulator transition (SIT) is driven purely by quantum fluctuations and is an example of a quantum phase transition [1]. The superconducting phase is considered to be a condensate of Cooper pairs with localized vortices, and the insulating phase is a condensate of vortices with localized Cooper pairs. Between these two states, there is only the metallic phase point, and this metal has a bosonic nature as well. The theoretical description based on this assumption was suggested in [2]. At finite temperatures, a quantum phase transition is influenced by the thermal fluctuations, and according to the theory, (i) the film resistance R near the magnetic-field-induced SIT at low temperature T in the vicinity of the critical field B_c is a function of one scaling variable $\delta = (B - B_c)/T^{1/\nu z}$,

with the critical exponents ν and z being constants of order of unity, and (ii) at the transition point, the film resistance is of the order $h/(2e)^2 \approx 6.5$ kΩ (the quantum resistance for Cooper pairs). Although much work has been done, and in many systems the scaling relations hold [3–8], the magnetic-field-induced SIT in disordered films remains a controversial subject, especially concerning the insulating phase and the bosonic conduction at $B > B_c$. There is experimental evidence [7] that, despite the magnetoresistance being nonmonotonic, and in the magnetic fields above the critical one, the derivative of resistance dR/dT is negative, the phase can be insulating as well as metallic. The behavior of the resistance in this region discussed in [5, 6] in terms of the magnetic-field-induced SIT (which is essentially *bosonic* in nature) can actually be explained on the basis of a *fermionic* approach, namely, in the frames of the theory of the quantum corrections to the conductivity in disordered metals. The possibility of such interpretation is shown in [9] based on the recent calculation of the quantum corrections due to superconducting fluctuations [10]. As a usual thermodynamic superconductor–normal metal transition, provided that the behavior of this metal is controlled, to a considerable degree, by the quantum corrections and a superconductor–insulator transition may have very similar experimental manifestations, some clear criteria are needed to enable one to tell which of the two underlies the behavior observed experimentally. Supposing the SIT to be
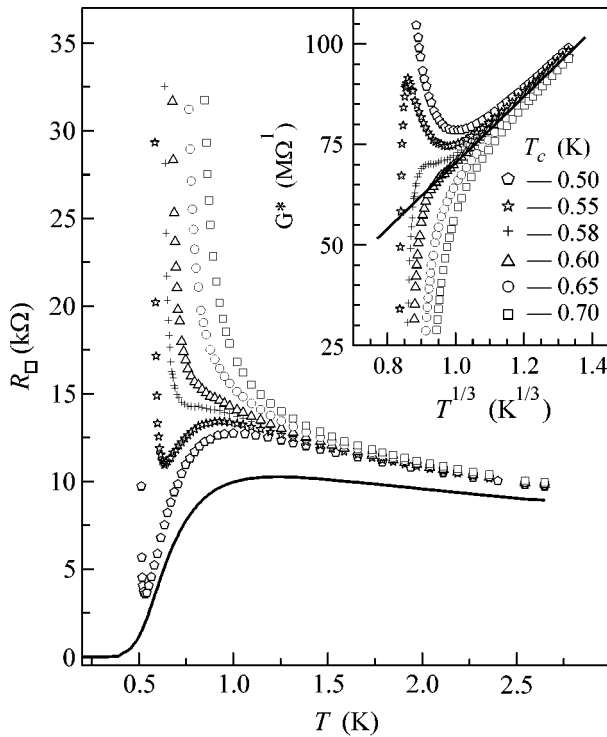
Fig. 1. Temperature dependence of the resistance per square for sample 1 (solid line). Curves depicted by symbols correspond to $R^*(T_c)$ (see text) and are obtained after subtraction of the Aslamasov–Larkin correction (1) with different T_c, which are listed in the inset. These curves are presented as $G^* = 1/R^*$ vs. $T^{1/3}$ in the inset.
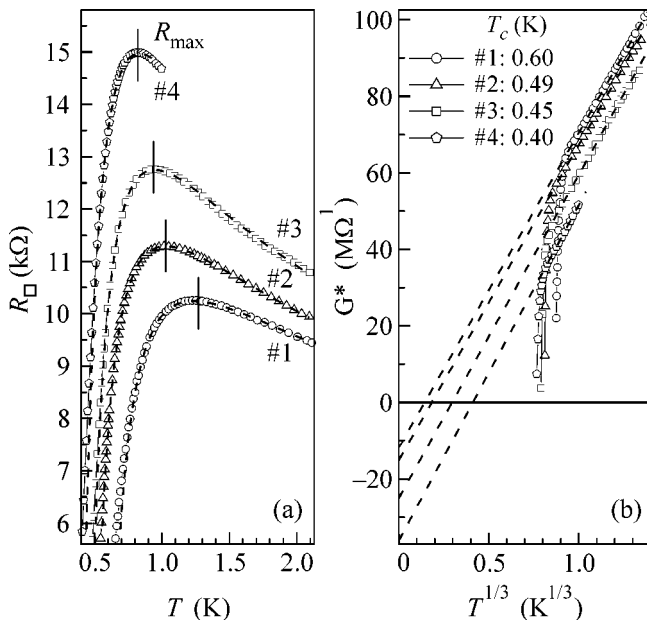
Fig. 2. (a) Temperature dependence of the resistance per square for four samples (symbols) and corresponding calculated curves $R_{AA + AL}$ (dashed lines) at optimally fitted values of a and b (4) and T_c. (b) $G^* = 1/R^*$ vs. $T^{1/3}$ for the same samples at optimally fitted values of the critical temperature T_c listed in the figure.

the cause (e.g., the temperature dependence is found to be of an activated type), the question is then what effect the magnetic field may have on the bosonic insulator.

In this paper, we present the results of measurements and detailed analysis of temperature and magnetic field dependence of the resistance of TiN films, devoting attention to a careful examination of the presence of the insulating phase and its alteration on the high-field side of the SIT.

A TiN film with a thickness of 5 nm was formed on 100 nm of SiO_2 grown on top of $\langle 100 \rangle$Si substrate by atomic layer chemical vapor deposition at 350°C [11]. Structural analysis shows that the formed TiN films are polycrystalline. The films exhibit low surface roughness and consist of a dense packing of the crystallites, with a rather narrow distribution of size and an average size of roughly 30 nm. The samples for the transport measurements were fabricated into Hall bridges using conventional UV lithography and subsequent plasma etching. Four terminal transport measurements were performed using standard low-frequency techniques. The resistance data were taken at a measurement frequency of 10 Hz with an ac current of 0.04–1 nA. The magnetic field was applied perpendicular to the film.

Four samples with the same thickness (5 nm) but different degrees of disorder were studied in the present work. We begin by showing the temperature dependence of the resistance $R(T, 0)$ at zero magnetic field. $R(T, 0)$ data are presented in Fig. 1 for sample 1 and in Fig. 2 for all samples studied in this work. The resistance is a nonmonotonic function of the temperature, as is seen more clearly in Fig. 2a. With a decrease of T, the increase of the resistance, which is observed from $T = 300$ K, is followed by a drop to the superconducting state. The transitions are significantly broadened. To explore the reasons for such behavior and to determine the main sample parameters, we apply an approach similar to the one used previously in [12]. As films under study are high-resistive, it should be expected that the dependence $R(T)$ is strongly affected by the contribution of superconducting fluctuations (the Aslamazov–Larkin correction [13]) even at temperatures far from the transition temperature T_c:

$$\Delta G_{AL} = \frac{e^2}{16\hbar} \left[\ln\left(\frac{T}{T_c}\right) \right]^{-1}. \qquad (1)$$

After extraction of this correction, with T_c being the only free parameter, we obtain the temperature dependence $R^*(T_c) = (1/R_\square - \Delta G_{AL}(T_c))^{-1}$, which is depicted by symbols in Fig. 1. The curves $R^*(T_c)$ obtained with $T_c < 0.6$ K are nonmonotonic, whereas the ones corresponding to $T_c > 0.6$ K give too strong a growth of the resistance. The choice of $T_c = 0.6$ K is confirmed by the further analysis of R^*, which is carried out for a start in terms of 3D "bad" metal in the vicinity of the metal–insulator transition (MIT) [14]. In the critical region of the MIT, the behavior of the system is governed by

electron–electron interaction and the temperature dependence of the conductivity is controlled by only temperature-dependent scale $L_T = \sqrt{\hbar D/k_B T}$:

$$\sigma = \frac{e^2}{\hbar}\frac{1}{L_T}. \tag{2}$$

Using Einstein's relation $\sigma = e^2 D(\partial N/\partial\mu)$, the conductivity can be rewritten as

$$\sigma = \frac{e^2}{\hbar}\left(T\frac{\partial N}{\partial\mu}\right)^{1/3}. \tag{3}$$

The representation of (3) in the form of

$$G_{AA}(T) = a + bT^{1/3} \tag{4}$$

is usually used to discriminate between a metal and an insulator by means of determination of the sign of the parameter a upon extrapolation to $T = 0$ (see, as an example, [15]). A positive value of a indicates the metallic state, whereas a negative value of a points to activated conductance at lower temperatures.

The inset of Fig. 1 shows the conductance $G^* = 1/R^*$ versus $T^{1/3}$. The dependence $G^*(T^{1/3})$ at $T_c = 0.6$ K is monotonic, and the temperature, to which the linear character of G^* is endured, is the lowest one. Determining in this way the values of a and b in (4) and T_c, we can fully describe the temperature dependence of the resistance film studied ($R_{AA+AL} = [G_{AA}(a, b) + \Delta G_{AL}(T_c)]^{-1}$). The outcome of the above procedure applied to all samples under study is illustrated in Fig. 2. At $T > T_c$, R_{AA+AL} closely follows the experimental data, justifying the validity of the above procedure and indicating that, with the deduction of the direct contribution of the superconducting fluctuations, the conductance of the film is reasonably described by Eq. (4). It is interesting to note that the slope of the dependences $G^*(T^{1/3})$ plotted in Fig. 2b (or the parameter b in Eq. (4)) is approximately the same for all samples studied, whereas the values $a \equiv G^*(0)$ differ significantly.

Additional information which can been extracted from the analysis is the estimation of parameters like the compressibility

$$\frac{\partial N}{\partial\mu} = \frac{1}{k_B}\left(\frac{b\hbar}{e^2 d}\right)^3, \tag{5}$$

the diffusion coefficient

$$D = \frac{k_B}{\hbar}\left(\frac{e^2 d}{b\hbar}\right)^2 T^{1/3}, \tag{6}$$

and $k_F l = 3Dm/\hbar$. Here, the value of b is determined from the linear approximation of G^* versus $T^{1/3}$ (Eq. (4)) and d is the thickness of the film. The following numbers are obtained: $\partial N/\partial\mu = 3.6 \times 10^{21}$ eV^{-1} cm^{-3},

$D = 0.29$ cm^2/s $(T/K)^{1/3}$, and $k_F l = 0.74(T/K)^{1/3}$, that is, $k_F l < 1$ at $T < 2.4$ K.

It should be noted that, in order to take into account the superconducting fluctuations, we have used Eq. (1), which is valid for the two-dimensional case. The condition under which a film may be considered two-dimensional with respect to superconducting fluctuations is

$$\ln\left(\frac{T}{T_c}\right) \ll \frac{\pi\hbar D}{8k_B T_c d^2}. \tag{7}$$

Physically, this inequality denotes that the time of diffusive motion across the film is less than the fluctuation Cooper pair lifetime (or Ginzburg–Landau time)

$$\tau_{GL}^{-1} = \frac{8k_B T}{\pi\hbar D}\ln\left(\frac{T}{T_c}\right). \tag{8}$$

Condition (7) can be rewritten as $d^2 \ll D\tau_{GL} = l_{GL}^2$. Using the estimation of the diffusion coefficient, we find that l_{GL} is larger than the film thickness at all temperatures under study.

One more relevant information can been received from the above analysis. Let us add Eqs. (3) and (1) and rewrite total conductance as follows:

$$G = G_{AA} + \Delta G_{AL} = \frac{e^2}{\hbar}\frac{d}{L_T} + \frac{e^2}{2\pi\hbar}\frac{l_{GL}^2}{L_T^2}. \tag{9}$$

Then, the temperature corresponding to the minimal value of G is determined by the condition

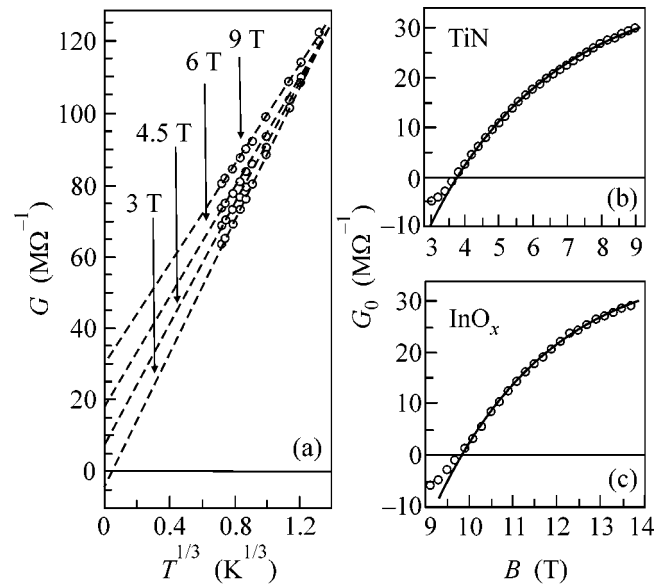$$L_T = l_{GL}\left(\frac{12}{\pi^2}\frac{l_{GL}}{d}\right)^{1/3}, \tag{10}$$

and, accordingly, the maximum of $R(T)$ (R_{max} in Fig. 2a) results from the condition $L_T \approx l_{GL}$. Thus, the nonmonotonic temperature dependence of the resistance is the consequence of a competition of two length scales: l_{GL} being responsible for Cooper pairing and L_T defining the electron–electron interaction. It should be stressed that the above estimations are rough, since the application of Eq. (3) implies that $a = 0$ in (4). There is nothing like this in our case, and, moreover, for the films under study, we get $a < 0$. It says that the underlying state is insulating.

We now turn to the evolution of the resistance with temperature for various magnetic fields. Figure 3a shows the isomagnetic temperature dependences of the resistance of sample 4. Not too high magnetic field ($B < 2$ T) destroys the long-phase coherence and reveals the underlying insulating state. The high-field data appear to be more metallic in character: the magnetic field results in a significant suppression of the insulating phase above 2 T. This is seen more clearly on a typical set of $R_\square(B)$ traces measured on sample 1 (see Fig. 3b). The main feature of this graph is the presence of an intersection point at B_c, R_c. Using the B_c, we plot
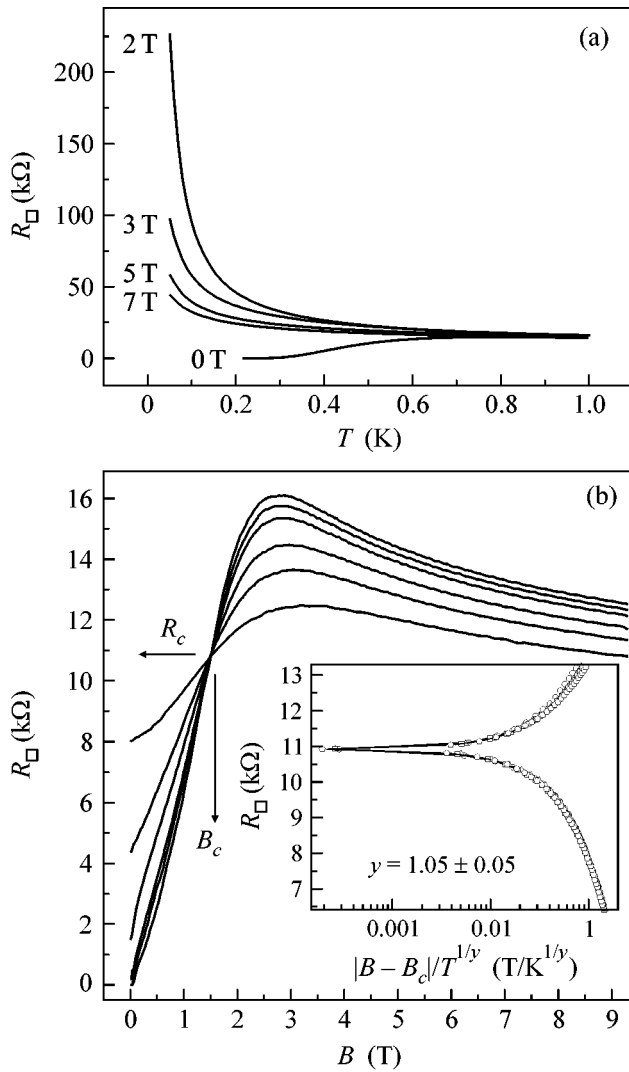
Fig. 3. (a) Dependences $R(T)$ at different B of sample 4. (b) Low-temperature isotherms of sample 1 in the (B, R) plane. Different curves represent different temperatures: 0.35, 0.38, 0.42, 0.51, 0.61, and 0.76 K. The point of intersection, $B_c = 1.52$ T, is the critical magnetic field, and $R_c = 10.9$ kΩ is the critical resistance. The inset shows a scaled plot of the same data with $y = \nu z = 1.05 \pm 0.05$.

Fig. 4. (a) Conductance $G = 1/R$ vs. $T^{1/3}$ at different magnetic fields on the high-field side of the SIT for sample 1. The magnetic field dependence of the zero temperature conductance determined from extrapolations in accordance with Eq. (4) are shown by symbols along with the dependences calculated from an empirical expression (11): (b) sample 1 (this work) and (c) InO_x [8].

the same data against the scaling variable $|B - B_c|/T^{1/\nu z}$ and adjust the product of the critical exponents νz to obtain the best scaling of the data (inset of Fig. 3b). However, such behavior, previously regarded as the main evidence of the existence of SIT, is actually not incontestable proof of the presence of the insulating phase at $B > B_c$ [9]. In order to ascertain the type of phase, we have analyzed the temperature dependence of the high-field conductance at different magnetic fields. In this regime, $G(T)$ is well described by Eq. (4), as indicated in Fig. 4a. As $G(0)$ is negative in fields higher than the critical field, we can conclude that this phase is insulating. With further increase of B, the sign of $G(0)$ changes, which points towards the transition to

the metallic state. The extrapolation to $T = 0$ allows us to determine not only the field of the insulator–metal transition (B_{IM}) but also the magnetic field dependence of the zero-temperature conductance. The result of this procedure is presented in Fig. 4b. Analysis of the zero-temperature conductance at $B > B_{IM}$ reveals that it is well described by the empirical expression

$$G(T = 0, B) = \frac{e^2}{h}\left(1 - \exp\left[\frac{B_{IM} - B}{B^*}\right]\right) \qquad (11)$$

shown by the solid line in Fig. 4b. The magnetic-field-induced insulator–metal transition on the high-field side of SIT was earlier observed in works of Gantmakher *et al.* on InO_x [7, 8]. Applying the same procedure to their data (see left panel of Fig. 1 of [8]), we find that the dependence $G(T = 0, B)$ is also well described by Eq. (11) (see Fig. 4c). The exponential dependence of $G(T = 0, B)$ may result from a broad dispersion of the binding energies of localized Cooper pairs. The most important result is the zero-temperature asymptotic value of the resistance, which is equal to the quantum resistance $R_Q = h/e^2$. The saturation of the low-temperature magnetoresistance to the quantum resistance was demonstrated on beryllium films [16]. Although the authors of [16] consider their films to be deep within the insulating phase, it is not improbable that they are superconducting at lower temperature, i.e., that the correlated insulating phase consists of localized Cooper pairs. We believe that observed behavior, namely, the

gradual approach of the low-temperature magnetoresistance towards the quantum resistance, is a very general feature of a bosonic insulator on the high-field side of the magnetic-field-tuned SIT.

In conclusion, we have studied the temperature and magnetic field dependence of the resistance of TiN films. We have demonstrated that the nonmonotonic temperature dependence of the resistance at zero magnetic field results from the concurrence of superconducting correlations and localization, with presumably the underlying insulating state having a bosonic nature. The destruction of the long-range phase coherence by a magnetic field highlights this insulating state. The further evolution of the system towards very high magnetic fields is in accordance with the breakup of such localized Cooper pairs and drives the system eventually into a metallic regime. The saturation of the low-temperature magnetoresistance near the quantum resistance seems to be a very general feature, occurring in several different materials. The nature of the insulating state and high-field metallic state requires further investigation.

REFERENCES

1. S. L. Sondhi, S. M. Girvin, J. P. Carini, and D. Shahar, Rev. Mod. Phys. **69**, 315 (1997).

2. M. P. A. Fisher, Phys. Rev. Lett. **65**, 923 (1990).

3. A. F. Hebard and M. A. Paalanen, Phys. Rev. Lett. **65**, 927 (1990).

4. N. Marcovic, C. Christiansen, A. M. Mack, *et al.*, Phys. Rev. B **60**, 4320 (1999).

5. A. Yazdani and A. Kapitulnik, Phys. Rev. Lett. **74**, 3037 (1995).

6. S. Okuma, T. Terashima, and N. Kokubo, Solid State Commun. **106**, 529 (1998); S. Okuma, T. Terashima, and N. Kokubo, Phys. Rev. B **58**, 2816 (1998).

7. V. F. Gantmakher, M. V. Golubkov, V. T. Dolgopolov, *et al.*, Pis'ma Zh. Éksp. Teor. Fiz. **68**, 337 (1998) [JETP Lett. **68**, 363 (1998)].

8. V. F. Gantmakher, M. V. Golubkov, V. T. Dolgopolov, *et al.*, Pis'ma Zh. Éksp. Teor. Fiz. **71**, 693 (2000) [JETP Lett. **71**, 473 (2000)].

9. V. F. Gantmakher, S. N. Ermolov, G. E. Tsydynzhapov, *et al.*, Pis'ma Zh. Éksp. Teor. Fiz. **77**, 498 (2003) [JETP Lett. **77**, 424 (2003)].

10. V. M. Galitski and A. I. Larkin, Phys. Rev. B **63**, 174 506 (2001).

11. A. Satta, G. Beyer, K. Maex, *et al.*, Mater. Res. Soc. Symp. Proc. **612**, D6.5.1 (2000).

12. V. F. Gantmakher and M. V. Golubkov, Pis'ma Zh. Éksp. Teor. Fiz. **73**, 148 (2001) [JETP Lett. **73**, 131 (2001)].

13. L. G. Aslamazov and A. I. Larkin, Fiz. Tverd. Tela (Leningrad) **10**, 1104 (1968) [Sov. Phys. Solid State **10**, 875 (1968)]; B. L. Al'tshuler, A. A. Varlamov, and M. Yu. Reizer, Zh. Éksp. Teor. Fiz. **84**, 2280 (1983) [Sov. Phys. JETP **57**, 1329 (1983)].

14. B. L. Al'tshuler and A. G. Aronov, Pis'ma Zh. Éksp. Teor. Fiz. **37**, 349 (1983) [JETP Lett. **37**, 410 (1983)]; B. L. Al'tshuler and A. G. Aronov, in *Electron–Electron Interactions in Disordered Systems*, Ed. by A. L. Efros and M. Pollak (North-Holland, Amsterdam, 1985).

15. M. C. Maliepaard, M. Pepper, R. Newbury, and G. Hill, Phys. Rev. Lett. **61**, 369 (1988); M. C. Maliepaard, M. Pepper, R. Newbury, *et al.*, Phys. Rev. B **39**, 1430 (1989).

16. V. Yu. Butko and P. W. Adams, Nature **409**, 161 (2001).

Nonequilibrium Acoustic Phonons in $Y_3Al_5O_{12}$-Based Nanocrystalline Ceramics

Yu. N. Barabanenkov[1], S. N. Ivanov[1], A. V. Taranov[1], E. N. Khazanov[1, *], H. Yagi[2],
T. Yanagitani[2], K. Takaichi[3], J. Lu[3], J. F. Bisson[3], A. Shirakawa[3],
K. Ueda[3], and A. A. Kaminskii[4]

[1] *Institute of Radio Engineering and Electronics, Russian Academy of Sciences, ul. Mokhovaya 18, Moscow, 125009 Russia*
e-mail: khazanov@nep.cplire.ru
[2] *Konoshima Chemical Co., Takuma Works, 769-1103 Kagawa, Japan*
[3] *Institute for Laser Science, University of Electro-Communications, 182-8585 Tokyo, Japan*
[4] *Shubnikov Institute of Crystallography, Russian Academy of Sciences, Leninskiĭ pr. 59, Moscow, 119333 Russia*
Received March 3, 2004

The phonon transport processes in high-transparency nanocrystalline laser ceramics based on cubic $Y_3Al_5O_{12}$ garnet oxide were investigated by the heat-pulse technique. The propagation kinetics of nonequilibrium acoustic phonons was studied in the range of helium temperatures (1.7–3.8 K). The structural model is suggested for the intergrain layers, and their thickness is estimated. © 2004 MAIK "Nauka/Interperiodica".

PACS numbers: 63.20.-e; 81.07.Bc

Today, many divisions of modern fundamental physics, including laser physics and quantum electronics, cannot be imagined without the use of nanocrystalline materials.

The first ceramics capable of generating stimulated radiation (SR) were synthesized on the basis of $CaF_2:Dy^{2+}$ flourite ($^5I_7 \longrightarrow {}^5I_8$ generation channel) in the mid-1960s [1] and Y_2O_3-$ThO_2:Nd^{3+}$ ($^4F_{3/2} \longrightarrow {}^4I_{11/2}$) in the early 1970s [2]. In 1995, $Y_3Al_5O_{12}:Nd^{3+}$-based ceramics were obtained [3] and used to fabricate a disk-shaped active element 8 mm in diameter and 2 mm in thickness. Its optical quality was sufficiently high for engineering a micron laser ($^4F_{3/2} \longrightarrow {}^4I_{11/2}$) with diode-laser (DL) excitation. Laser ceramics $Y_3Al_5O_{12}:Nd^{3+}$ synthesized by the modified, though traditional technologies [4] were used to fabricate only millimeter-sized active elements, and their generation parameters were at a considerable disadvantage in relation to the corresponding laser-crystal parameters.

In the last few years, size-unrestricted high-transparency $Y_3Al_5O_{12}:Nd^{3+}$ laser ceramics have been synthesized using the newest nanotechnology and vacuum caking in the absence of an external pressure [5] (see, e.g., [6, 7] and references cited therein). They were used to fabricate $Nd^{3+}:Y_3Al_5O_{12}$ lasers with DL pumping and an output power on the kilowatt level (from ≈370 mW in the year 2000 [8] to ≈1.5 kW in 2001 [9]). A high optical perfection of the new $Y_3Al_5O_{12}$ and $Y_3Al_5O_{12}:Nd^{3+}$ ceramics was confirmed by the excitation of high-order stimulated Raman scattering in them [10]. Even at the early stage of investigations, the gen-

eration parameters of lasers based on the large-sized nanocrystalline $Y_3Al_5O_{12}:Nd^{3+}$ ceramics [7] outperformed their crystal analogues [6]. The same technique was used to synthesize nanocrystalline laser ceramics based on cubic oxides Y_2O_3, Sc_2O_3, $YGdO_3$, and Lu_2O_3 activated with the Nd^{3+} and Yb^{3+} ions [11]. Due to the combination of the generation and some other physical properties, these ceramics are promising for use in femtosecond lasers [12] and powerful laser drivers in the experiments on controlled thermonuclear fusion [13].

Our studies have shown that the optical and lasing characteristics of all the aforementioned nanocrystalline ceramics cannot be improved without the knowledge of the properties and structure of the intergrain boundaries, their thickness, composition, etc., because the intergrain boundaries and pores in a ceramic material are responsible for the laser losses in it.

The analysis of the character and structure of the intergrain boundaries is a rather complicated problem. Within a limited volume, it is solved by the method of high-resolution transmission electron microscopy. The corresponding studies have confirmed the existence of nanometer-thick continuous intergrain layers in a ceramic material [14]. At the same time, the volume analyzed by an electron microscope is exceedingly small and does not allow any conclusion to be drawn about the practically important averaged or macroscopic properties of the intergrain material [15].

In this work, the heat-pulse technique was used as the main method for studying the propagation kinetics of nonequilibrium thermal phonons and their scattering efficiency at temperatures of 1.7–3.8 K in $Y_3Al_5O_{12}$-
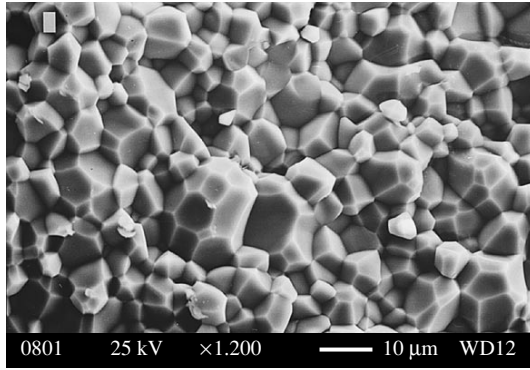
Fig. 1. Microstructure of the cleavage surface for sample 4.

Fig. 2. Time dependence of the amplitude of nonequilibrium phonon-radiation signal for ceramic sample 2.

and $Y_3Al_5O_{12}$:Nd^{3+}-based ceramics. At helium temperatures, the wavelength of phonons injected into the sample becomes comparable not only to the sizes of material-forming fragments (grains) but also to the sizes (thickness) of the intergrain boundaries, pores, etc. The diffusion data on the nonequilibrium phonons can be used to estimate, within the framework of certain models, the transparency of the boundaries between the fragments to predict the thermal and mechanical characteristics of material. A detailed description of the method can be found in [16–18].

The surface (cleavage) microstructure was examined for each sample using a JSM-840 (Jeol) scanning electron microscope. The photographs were processed on the basis of the Soft Imaging System program for the determination of the mean grain size R in ceramics and the standard deviation σ from the mean value.

An example of a microphotograph of the cleavage surface in a ceramic sample is shown in Fig. 1. The grains are close-packed crystallites (or single crystals), evidencing their high structural perfection. The mean grain sizes R and the standard deviations σ for the samples studied are given in the table.

Examples of heat-pulse propagation curves are presented in Fig. 2 for several temperatures. The bell-shaped bolometer signal has a well-defined maximum, typical of the diffusional propagation of injected nonequilibrium phonons. The time t_{max} at which the signal is maximal increases with the temperature of injected phonons. According to [18], the expression for the arrival time t_{max} of the maximal signal from the phonon-radiation pulse in the case of diffusional phonon propagation in a ceramic sample of thickness $L \gg R$ has the form (plane source):

$$t_{max} = L^2/2D_{eff}. \tag{1}$$

The diffusion coefficients D_{eff} at $T = 3.8$ K for the samples studied are given in the table.

The phonon transport mean free path l_{tr} was determined from the usual relation

$$D_{eff} = 1/3 v_s l_{tr}, \tag{2}$$

where v_s is the mean sound velocity in the grain at $T = 3.8$ K, and $l_{tr}/R \gg 1$ (see table). In all samples, the ratio l_{tr}/R increased with decreasing temperature. This result

Parameters of the $Y_3Al_5O_{12}$ samples studied in this work

Sample no.	Composition	Sample length L (mm)	Mean grain size R (µm)	Standard deviation σ from the mean size (µm)	Diffusion coefficient D_{eff} at 3.8 K (cm²/s)	l_{tr}/R ratio	$\Psi = 0.6 R/l_{tr}$	$q l_{gb}$	l_{gb} [Å]
1	$Y_3Al_5O_{12}$	1.45	13.5	4.85	0.85×10^3	3.4	0.176	0.175	3.6
2	$Y_3Al_5O_{12}$	1.60	11.0	5.3	0.55×10^3	2.7	0.222	0.22	4.6
3	$Y_3Al_5O_{12}^{a}$	9.0	7.0	–	2×10^3	15.3	0.04	0.082	1.7
4	$Y_3Al_5O_{12}^{a}$	3.1	6.5	3.25	1.45×10^3	12.0	0.05	0.09	1.85
5	$Y_3Al_5O_{12}^{b}$	5.7	11.4	5.85	2.6×10^3	12.2	0.05	0.09	1.85

[a] Activated with Nd^{3+} ions ($C_{Nd} \approx 1$ at. %).
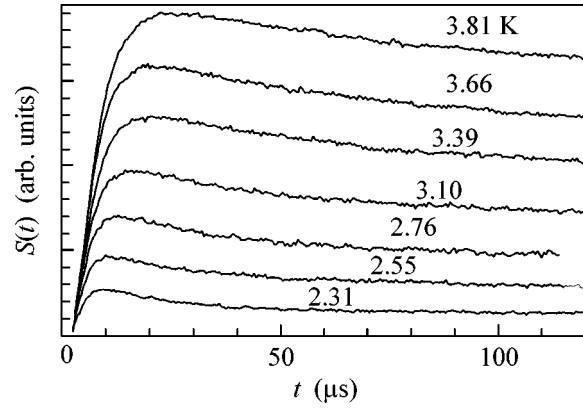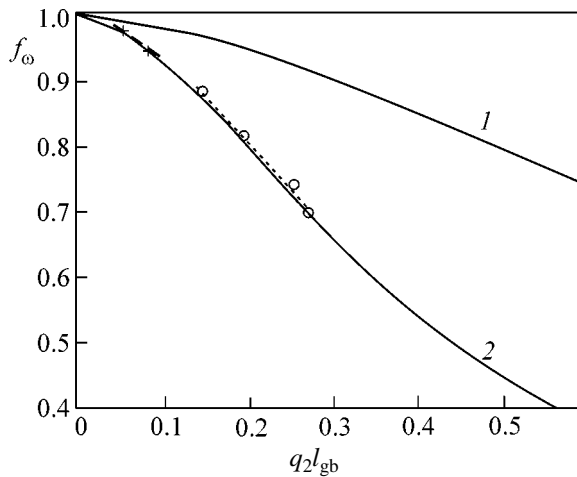[b] Activated with Nd^{3+} ions ($C_{Nd} \approx 2$ at. %).

Fig. 3. The probability f_ω of phonon transition from grain to grain through a plane boundary layer of thickness l_{gb}, calculated as a function of $q_2 l_{gb}$, where $q_2 = \omega/v_2$ is the phonon wave vector in the boundary level. The parameters for the grain material are $\rho = 4.55$ and $v = 5.6 \times 10^5$ cm/s (data for $Y_3Al_5O_{12}$). Curve *1*: $\rho_2 = 2.65$ and $v_2 = 4.7 \times 10^5$ cm/s (data for crystalline SiO_2). Curve *2*: $\rho_2 = 2.2$ and $v_2 = 4.05 \times 10^5$ cm/s (data for SiO_2 in glassy phase). Points on curve *2* are experimental; (o) sample 2 and (+) sample 4.

allows the conclusion to be drawn that $Y_3Al_5O_{12}$ and $Y_3Al_5O_{12}$:Nd^{3+} ceramics are perfect from the standpoint of low-temperature phonon kinetics and that phonons are scattered only by the grain boundaries, with the probability of phonon transition from grain to grain being close to unity.

Let us turn to the quantitative analysis of the obtained results. Earlier, the relation $l_{tr}/R > 1$ was observed in the experiments with high-density α-Al_2O_3 ceramics [19]. The authors of that work explained these results on the assumption that phonons are scattered by the orientationally disordered grains, while the interlayers between them are absent. It was assumed that

$$l_{tr} = \frac{l}{1 - \langle \cos\varphi \rangle}, \qquad (3)$$

where $l \sim R$ is the mean free path before the scattering event at the grain boundary, and that the mean cosine $\langle \cos\varphi \rangle$ of single-scattering angle corresponds to the wave elastic scattering at the grain boundaries with different crystallographic orientations.

In our case of a highly isotropic material, the scattering is determined by the grain-boundary thickness l_{gb} and structure. A simplified model of this mechanism was considered in [17], where, following the method of acoustic matching of media [20], phonon scattering upon the transition through a plane boundary layer was estimated with allowance for all possible incidence and transition angles. The computational results for a number of sets of structural parameters and a thin grain boundary $q_2 l_{gb} < 1$ are presented in Fig. 3. First of all, one can see from the curves in Fig. 3 that the probability f_ω of phonon transition from grain to grain is close to unity and decreases with a rise in temperature (i.e., frequency of injected phonons), in line with our experimental results. This suggests that the quantity f_ω is analogous to $\langle \cos\varphi \rangle$ in Eq. 3. Using the curves in Fig. 3 and the experimental values of l_{tr} and $l \approx 0.6R$ [19], one can determine f_ω and estimate the thickness of intergrain layers for our samples. The results are presented in the table for the intergrain parameters corresponding to fused quartz. Such a choice of interlayer material is dictated by the fact that SiO_2 is used as an additive in the synthesis of $Y_3Al_5O_{12}$ ceramics [21]. Using the value of l_{gb} at temperature $T = 3.8$ K and the experimental data, one can construct f_ω as a function of $q_2 l_{gb}$, i.e., of temperature. These curves are presented in Fig. 3 for two samples with the maximal (sample 4) and minimal (sample 2) diffusion coefficients. The calculations agree well with the experiment. For the intergrain transparency corresponding to the crystalline quartz (Fig. 3, curve *1*), the values of l_{gb} are approximately a factor of 2 larger, though smaller than the quartz lattice parameters, which, considering the complex structure of quartz, renders this model unrealistic. Note also that curve *1* in Fig. 3 does not take into account the loss caused by the orientational disorder of grains and SiO_2 interlayers in $Y_3Al_5O_{12}$; otherwise, curves *1* and *2* in Fig. 3 would be closer to each other.

The main result of this work is that the grain-boundary thickness l_{gb} is smaller than the estimates made in [13] and the lattice parameter of $Y_3Al_5O_{12}$. The grain boundary is formed from the additive materials used in synthesis, and among them fused quartz is the most probable.

We now turn to the results obtained for the YAlG samples with Nd additives, where the diffusion coefficients are appreciably greater. With the above model of phonon flow through the intergrain layer, one should expect that f_ω (i.e., diffusion coefficient) increases with an increase in the layer density due to the implantation of the Nd^{3+} ions. It is conceivable that this occurs because of the "drain" of the excess Nd^{3+} ions into this layer, whose chemical and physical structures are far from those of the ideal model used in this work.

In summary, the approach applied in this work to the propagation of nonequilibrium phonons in ceramic samples has made it possible to draw the conclusion about a high perfection of the grains in $Y_3Al_5O_{12}$ ceramics, estimate the thickness of intergrain boundaries, and make the suggestion as to the material of intergrain layer and the influence of Nd doping on the structure of this layer. The model suggested for the structure of boundary layer is clearly inconclusive, and its development is the subject of our further experiments with $Y_3Al_5O_{12}$:Nd^{3+}-based ceramics with a broad set of

neodymium contents, grain sizes, and other technological parameters.

REFERENCES

1. E. Carnall, S. E. Hatch, and W. E. Parsons, *Material Science Research* (Plenum, New York, 1966), p. 165.

2. C. Greskovich and J. P. Chernoch, J. Appl. Phys. **44**, 4599 (1973).

3. A. Ikesue, T. Konoshita, K. Kamata, *et al.*, J. Am. Ceram. Soc. **78**, 1033 (1995).

4. T. Taira, A. Ikesue, and K. Yoshida, in *Advanced Solid-State Lasers* (OSA, Washington, DC, 1998), p. 430.

5. Jpn Appl. Nos. 10-101333 and 10-101411 (1998).

6. K. Ueda, J. Lu, K. Takaichi, *et al.*, Rev. Laser Eng. **31**, 465 (2003).

7. A. A. Kaminskii, Phys. Status Solidi A **200**, 215 (2003).

8. J. Lu, M. Prabhu, J. Song, *et al.*, Appl. Phys. B **71**, 469 (2000).

9. J. Lu, T. Murai, K. Takaichi, *et al.*, Laser. Phys. **11**, 1053 (2001); J. Lu, K. Ueda, H. Yagi, *et al.*, J. Alloys Compd. **341**, 220 (2002).

10. A. A. Kaminskiĭ, H. J. Eichler, K. Ueda, *et al.*, Pis'ma Zh. Éksp. Teor. Fiz. **72**, 717 (2000) [JETP Lett. **72**, 499 (2000)]; A. A. Kaminskii, K. Ueda, H. J. Eichler, *et al.*, Laser Phys. Lett. **1**, 4 (2004).

11. J. Lu, J. F. Bisson, K. Takaichi, *et al.*, Appl. Phys. Lett. **83**, 1101 (2003); J. Lu, T. Murai, K. Takaichi, *et al.*, Jpn. J. Appl. Phys., Part 2 **41**, L1277 (2001); J. Lu, K. Takaichi, T. Uematsu, *et al.*, Appl. Phys. Lett. **81**, 4324 (2002).

12. A. Shirakawa, K. Takaichi, H. Yagi, *et al.*, Opt. Express **11**, 2911 (2003).

13. K. Ueda, J. Lu, K. Takaichi, *et al.*, Rev. Laser Eng. **31**, 465 (2003).

14. D. R. Clarke, J. Am. Ceram. Soc. **70**, 15 (1987).

15. P. Ernst, O. Kienzle, and M. Ruhle, J. Eur. Ceram. Soc. **19**, 655 (1999).

16. C. N. Ivanov and E. N. Khazanov, Zh. Éksp. Teor. Fiz. **88**, 299 (1985) [Sov. Phys. JETP **61**, 172 (1985)].

17. Yu. N. Barabanenkov, V. V. Ivanov, S. N. Ivanov, *et al.*, Physica B (Amsterdam) **316–317**, 269 (2002).

18. S. N. Ivanov, A. G. Kozorezov, A. V. Taranov, *et al.*, Zh. Éksp. Teor. Fiz. **102**, 600 (1992) [Sov. Phys. JETP **75**, 319 (1992)].

19. A. A. Kaplyanskiĭ, M. B. Mel'nikov, and S. P. Feofilov, Fiz. Tverd. Tela (St. Petersburg) **38**, 1434 (1996) [Phys. Solid State **38**, 792 (1996)].

20. W. A. Little, Can. J. Phys. **37**, 334 (1959).

21. J. Lu, M. Prabhu, J. Xu, *et al.*, Appl. Phys. Lett. **77**, 3767 (2000).

Translated by V. Sakun

Electrophysical Properties of Calcium at High Pressures and Temperatures

V. E. Fortov[1], *, A. M. Molodets[1], V. I. Postnov[1], D. V. Shakhrai[1], K. L. Kagan[1],
E. G. Maksimov[2], A. V. Ivanov[2], and M. V. Magnitskaya[3]

[1] *Institute of Problems of Chemical Physics, Russian Academy of Sciences, Chernogolovka, Moscow region, 142432 Russia*
*e-mail: fortov@ras.ru
[2] *Lebedev Physical Institute, Russian Academy of Sciences, Leninskiĭ pr. 53, Moscow, 119992 Russia*
[3] *Vereshchagin Institute of High-Pressure Physics, Russian Academy of Sciences, Troitsk, Moscow region, 142190 Russia*
Received March 3, 2004

Electrical resistivity of two crystal phases of shock-compressed calcium and its melt was measured in a range of high pressures (10–50 GPa) and temperatures (800–1600 K). The thermodynamic equilibrium curves were constructed for different calcium phases and the shape of Hugoniot adiabat was determined in the region where it intersects the equilibrium curves. It is shown that sharp kinks observed earlier in the Hugoniot adiabat in shock experiments were caused not by the jumplike electronic transitions but by the intersections of the adiabat and the phase-equilibrium and melting curves. The electronic spectra of the calcium crystal phases were calculated using the electron-density functional method; the computational results are used to explain the observed behavior of the Ca resistivity under compression. © 2004 MAIK "Nauka/Interperiodica".

PACS numbers: 62.50.+p; 64.30.+t; 64.70.-p; 71.30.+h; 81.40.Vw

In the last years, the attention of experimenters and theorists has been drawn to the properties of elementary metals, in particular, alkali and alkaline-earth metals at high pressures. This is caused by some factors, e.g., by the fact that, under pressure, many polymorphic transitions in elementary metals are accompanied by the unexpected symmetry reduction and a decrease in packing density upon compression [1, 2]. Interest in these inquiries has quickened in connection with Ashcroft's assumption [3] about the possible lithium metal transition to the semiconducting state with the low-symmetry crystal structure oC8 at pressures above 100 GPa. The subsequent experimental and theoretical studies [4] did not confirm this assumption. As was shown in [6], the increase in the resistivity of shock-compressed Li [5, 6] can be explained by the sequential structural transformations observed in [4]. A dramatic increase in the resistivity was also observed for the shock-compressed bismuth [7] and sodium [8].

The behavior of alkaline-earth metals Ba, Sr, and Ca under pressure has drawn attention of researchers beginning in the 1960s (see, e.g., [9–11]). The study of the electronic structure of these metals within the framework of the pseudopotential theory has shown [10] that, at certain pressures, metals in the FCC phase become insulators or, more precisely, narrow-gap semiconductors. The experimental studies of the calcium resistivity ρ [12, 13] have shown that ρ is maximal at pressures on the order of 18 GPa. Moreover, it was found that the temperature resistivity coefficient near this maximum is negative; i.e., Ca in this pressure range behaves like a semiconductor.

The room-temperature phase diagram of Ca was studied in detail in [14] up to pressures of ≈80 GPa. At normal conditions, Ca crystallizes in the FCC phase and undergoes transition to the BCC phase at $P = 19.5$ GPa with a change of $\Delta V/V \approx 2\%$ in specific volume. Upon further compression, Ca undergoes transition at $P = 32$ GPa to the simple cubic (SC) structure with a volume jump of $\Delta V/V \approx 8\%$. The SC phase remains stable at least up to the pressures $P \approx 80$ GPa. In a more recent theoretical work [15], the total Ca energy at $T = 0$ was analyzed in detail on the basis of *ab initio* calculations of various crystal structures, and the pressures of the FCC–BCC–SC transition sequence were estimated. The theoretical value $P_{\text{calc}} \approx 15$ GPa calculated for the FCC–BCC transition proved to be underestimated, as compared to its experimental value, whereas the pressure $P_{\text{calc}} \approx 33$ GPa calculated for the BCC–SC transition coincided, to a good accuracy, with the experiment. In that work, gradual filling of the electron d band upon compression was considered as a physical reason causing the sequential structural transitions, especially the Ca BCC–SC transition.

In some experimental works [16, 17] on the shock compression of alkaline-earth, rare-earth, and transition metals, a jumplike increase in the slopes of Hugoniot adiabat was observed in the pressure range $P \approx 20$–100 GPa. For the particular case of Ca adiabats, these changes were assigned in [16, 17] to the electronic s–d transitions that result in low-compressible structures

under pressure. It should, however, be noted that the theoretical calculations of the Ca electronic structure (see, e.g., [11, 15]) show that no jumplike change in the character of electron wave functions (in other words, sharp electronic s–d transitions) occurs in calcium at any pressure. At zero pressure, Ca is a simple metal with valence s electrons and an almost empty d band, which lies above the Fermi level E_F though in close proximity to it, allowing calcium to be classified as a "pre-transition" metal. Upon compression, the d-band energy gradually goes down relative to E_F and the s band. Roughly speaking, the reason is that the high-pressure effect on the low-compressible d functions is weaker than on the spherical (and, hence, more compressible) s function and on E_F, whose position is determined by all valence electrons. Accordingly, the empty d states start to gradually fill (in the literature, this process is sometimes called "continuous s–d transition" [11]). It follows from the calculations that, upon compression to $V = 0.2V_0$, which, due to a high Ca compressibility, corresponds to a comparatively low pressure of ≈170 GPa, calcium has an electronic configuration close to $4sp^1 3d^1$ and displays the properties of a transition metal. The scenario described above allows the conclusion to be drawn that the kinks in the adiabats observed in [16, 17] have a different nature.

The purpose of this work was to study, both experimentally and theoretically, the behavior of shock-compressed calcium in the range of temperatures $T \sim 1000$ K and pressures $P \approx 10$–70 GPa. The diagnostics of phase transitions was carried out on the basis of conductivity measurements, and the temperature was calculated by the method of thermodynamic potentials.

Samples were calcium foils $0.1 \times 2 \times 8$ mm in size. Calcium was initially in the stable FCC phase. The shock compression and heating of the samples were accomplished by the impact of a metallic striker accelerated by detonation products to velocities of 2–3.5 km/s. The electrical resistivity and pressure in the shock-compressed sample were recorded simultaneously in the experimental arrangement described in [5–7]. The Ca sample and a manganin shock-compression pressure gauge were placed in the same plane between metallic screens in Teflon, which served as an insulator. Teflon also played the role of a material whose acoustic stiffness is lower than that of screens. Therefore, sample compression was performed by a sequence of one-dimensional plane shock waves [18, 19].

The Ca specific resistivity ρ was calculated as $\rho = \rho_0 (R/R_0)(V/V_0)$, where R is the measured resistance of the sample and V is its specific volume calculated by the method of thermodynamic potentials (see below). The reference data on ρ_0, R_0, and V_0 at atmospheric pressure and room temperature were taken as their initial values. The initial density of calcium was $1/V_0 = 1.55$ g/cm^3.

To interpret the compression-induced changes in the electric properties of Ca, *ab initio* microscopic calcula-

tions of the electronic structure and plasma frequency were carried out for various values of specific volume. Calculations were performed within the framework of the density functional theory by the full-potential linearized augmented plane wave (FP-LAPW) method using the WIEN2k program package [20]. It was shown that, in accordance with previous calculations [10, 11], calcium in the FCC phase undergoes transition to the semiconducting state in the range of compressions $0.75 \geq V/V_0 \geq 0.6$. It is significant, however, that the electron density of states $N(E_F)$ at the Fermi surface and the plasma frequency ω_{pl} decrease in the FCC phase in a much broader pressure range; i.e., metallic properties of Ca deteriorate and, correspondingly, the electrical resistivity increases (as known, $\rho \sim 1/\omega_{pl}^2$). These results are in compliance with the experimental data obtained in [12, 13] for the Ca resistivity under pressure. It should be noted that Ca in the BCC phase remains a good metal under any compression. Our calculations showed that a very narrow range, $0.55 \geq V/V_0 \geq 0.53$, of volumes where the Ca electronic structure has the semiconducting character also occurs in the SC phase. However, at $T = 0$, the BCC Ca is the stable phase in this region. Nevertheless, at a pressure corresponding to the BCC–SC transition, the metallic properties of Ca drastically deteriorate because of a decrease in $N(E_F)$ and ω_{pl} and, hence, in the number of charge carriers in the SC phase. Upon further compression, ω_{pl} increases in the SC phase, but it becomes equal to the BCC plasma frequency only at $V/V_0 \approx 0.3$.

We calculated the total crystal energy E_{tot} for all three phases and various values of specific volume V. The resulting $E_{tot}(V)$ dependence was used to construct the equation of state for $T = 0$ in the form $P(V) = -\partial E_{tot}(V)/\partial V$. In our calculations, as almost in all theoretical works on calcium (see, e.g., aforementioned work [15]), the FCC–BCC transition pressure $P_{tr} = 17$ GPa proved to be underestimated. The reason for such an understatement of P_{tr} remains to be clarified. To calculate the calcium temperature in shock waves and the phase-equilibrium curves at $T \neq 0$, the method of thermodynamic potentials was used. The Helmholtz free energy $F(V, T)$ served as the main thermodynamic potential. The expression for $F(V, T)$ was taken in the semiempirical form [21, 22]

$$F(V, T) = E_x(V)$$
$$+ 3R(\theta/2 + T\ln(1 - \exp(-\theta/T))) - a_s RT + E_m. \quad (1)$$

In Eq. (1), the standard notation is used. The fitting parameter a_s is zero for a solid body and nonzero for a melt. The parameter E_m specifies the reference level for the total energy $E_{tot}(V)$ of each phase. It is introduced to eliminate the aforementioned understatement of the FCC–BCC transition pressure in the *ab initio* calculations. The computational procedure for determining the thermal contribution to the Helmholtz free energy and
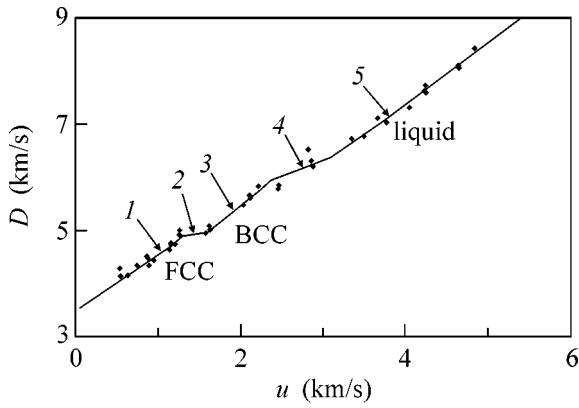
Fig. 1. Hugoniot adiabat for calcium in the "shock-wave velocity (*D*)–mass velocity (*u*)" coordinates. Points are for the experiment [8, 18]. Solid lines are the Hugoniot adiabats calculated in this work for (*1*) the FCC phase, (*2*) a mixture of the FCC and BCC phases, (*3*) the BCC phase on the basis of the *ab initio* calculations of the total energy $E_{tot}(V)$, (*4*) a mixture of the BCC phase and Ca melt, and (*5*) the Ca melt.
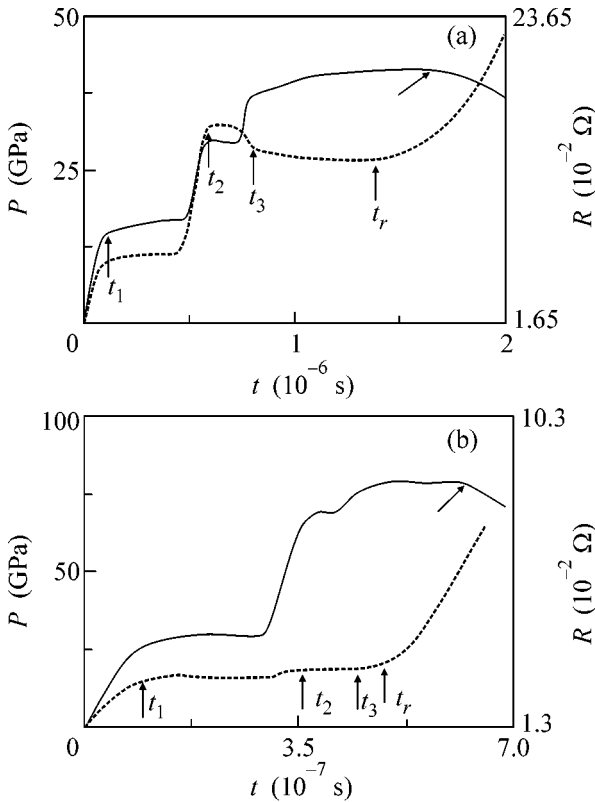
Fig. 2. Pressure *P*(*t*) (solid lines) and resistance *R*(*t*) (dashes) profiles in the case of the step shock-wave loading of the calcium sample: (a) shock-compressed solid Ca and (b) calcium melted upon shock compression. The vertical arrows indicate the instants of time t_1, t_2, and t_3 at which the quantities suffer jumplike changes under the action of sequential shock waves and the times t_r of the onset of a smooth increase in resistance. The skew arrows indicate the instants of time at which pressure starts to decrease due to the arrival of a rarefaction wave from the striker rear side.

the method of constructing the potential energy $E_x(V)$ and characteristic temperature $\theta(V)$ as functions of *V* are described in detail by one of us in [21]. The free parameters (excepting E_m) in Eq. (1) were determined from the Hugoniot adiabats obtained in [17, 23] and from the reference data on thermal properties of materials.

The Hugoniot curves were set off from the common array of experimental data for different calcium phases [17, 23] using the fact that, at low (compared to $P = -\partial E_{tot}/\partial V$) thermal pressures, the location of the calculated adiabat in the "shock-wave velocity (*D*)–mass velocity (*u*)" coordinates is virtually independent of the constant term E_m in Eq. (1). In this approximation, the Hugoniot curve of the BCC Ca can be calculated using only the *ab initio* total energy of this phase and expression (1) with key functions $\theta(V)$ and $E_x(V) = E_{tot}(V)$ taken in the form proposed in [21]. The results of this calculation are shown in Fig. 1 (straight line *3*).

One can see in Fig. 1 that straight line *3* coincides with only a part of the experimental points [17, 23]. Consequently, the remaining points belong to the other calcium phases and their mixtures: (*1*) FCC, (*2*) FCC + BCC mixture, (*4*) BCC + melt, and (*5*) melt. This subdivision allowed us to construct the thermodynamic potentials for the cited phases and calculate the equilibrium curves between these phases together with their Hugoniot adiabat in the vicinity of the equilibrium curves and to identify the calcium thermodynamic states obtained in our experiment on measuring the calcium electrical resistivity at high pressures and temperatures.

The typical experimental profiles with jumps (time dependences) in calcium resistance *R*(*t*) were of two types. Figure 2a shows the first type, characterized by a nonmonotonic increase in the resistance with pressure. The first jumplike increase in *R* at t_1 accompanies the pressure jump in the first shock wave. The second increase in *R* at t_2 occurs in the second shock. There is no surprise in the very fact that the sample resistance increases under the action of a shock wave, because it results in the rise of both the sample temperature and the number of various defects in the sample. However, the sample resistance drops jumpwise at the instant of time t_3. This drop in *R* in the third shock seems to be nontrivial. Because of the limited number of experimental data on electrical resistance, a detailed quantitative analysis of the temperature and pressure dependences of *R* cannot be carried out. However, based on the theoretical calculations and experimental data on the static Ca compression (at *T* = 300 K) and heating of Ca to the temperatures *T* on the order of melting temperature (at *P* = 0), one can suggest some scenarios for the explanation of the obtained experimental results.

The calcium phase diagram and the thermodynamic states arisen upon multiple shock compression are shown in Fig. 3. The calculations of the FCC–BCC equilibrium curve with allowance for temperature

(curve *2*) indicate that none of the thermodynamic states attained in the experiment fall within the FCC stability region. The thermodynamic state in the first shock wave is most likely in the BCC stability region. This state is depicted in Fig. 3 by the black square, and the temperature and the reciprocal specific volume $1/V$ calculated for this state are presented in the table.

The situation with the identification of the thermodynamic states in the second shock is much more complicated. As is seen in Fig. 3, the experimentally measured pressure $P = 28$ GPa lies to the left of the BCC–SC equilibrium curve (dashed curve *4*), i.e., in the stability region of the BCC phase. It should be noted that this equilibrium curve (taken from [24]) has only one experimental point measured at room temperature and pressure $P = 32$ GPa [14]. Because of the lack of thermal data, it is difficult to calculate this curve using the approach suggested in [21], as was done above for the FCC–BCC transition. It is only clear that the equilibrium curve should bend leftwards with increasing temperature, i.e., to the region of lower pressures. The corresponding behavior is clearly seen in the calculated equilibrium curve *2*. Of course, the bending of the BCC–SC curve may be appreciably smaller than for the FCC–BCC curve. On this basis, and also making allowance for the experimental uncertainties in measured pressure, we cannot state with certainty that the thermodynamic state in the second shock lies in the stability region of the BCC phase.

As to the calcium thermodynamic state in the third shock wave, the corresponding pressure $P = 36$ GPa is evidence that this phase is in the SC stability region. To estimate the temperatures in the second and third shock waves, we used the BCC free energy. Clearly, the kink caused by the heat of polymorphic transition at the BCC–SC equilibrium curve is not taken into account in this calculation. We assume that the ensuing overstatement of temperature is no less than the change (~150 K) in temperature in the interval where the Hugoniot curve coincides with the FCC–BCC equilibrium curve (Fig. 3). The thermodynamic states thus determined with a temperature error of ~150 K are given in the table and shown in Fig. 3. The state in the second shock is indicated in Fig. 3 by the centered square, and the SC states are indicated by the white squares. The data on $\rho(T, P)$ obtained for the BCC phase at $P = 18$ GPa in a separate experiment with a single wave are also presented in the table. The linear approximation of three ρ values corresponding to pressures of 14, 28, and 18 GPa

$$\rho(T, P) = A(T - T_0) + B(P - P_0) + C \qquad (2)$$

yields $A = -6.20 \times 10^{-10}$ Ω cm/K, $B = 7.05 \times 10^{-7}$ Ω cm/GPa, and $C = 2.17 \times 10^{-5}$ Ω cm.

Due to the uncertainty in the results of measurements and the lack of experimental points, one cannot confidently assert that $\rho(T, P)$ is described by linear dependence (2). However, despite the large error, one
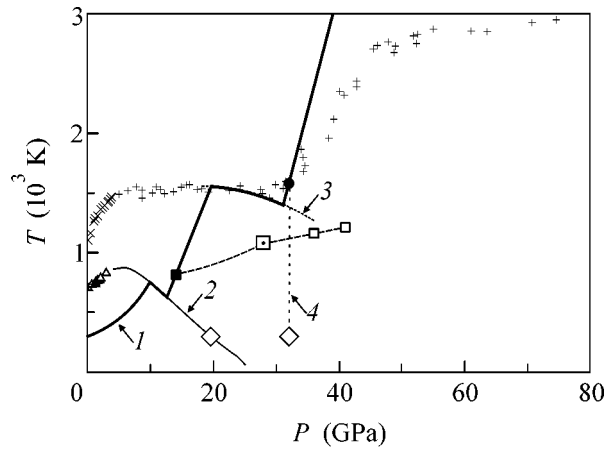
Fig. 3. Calcium phase diagram and thermodynamic states upon multiple shock compression: (Δ) experimental data [9] for the FCC–BCC equilibrium curve; (x) experimental data [9] for the melting curve of the BCC phase; (+) experimental data [24] for the Ca melting curve; and (◇) phase-transition pressures for calcium at room temperature [14]. Curve (*1*) is the Hugoniot adiabat calculated in this work for a one-shot compression of monolithic Ca; (*2*) calculated section of the FCC–BCC equilibrium curve; (*3*) calculated section of the BCC–melt equilibrium curve; (dashed lines) adiabats calculated for the step shock loading; (*4*) BCC–SC equilibrium curve from [24]; (■) thermodynamic state of BCC Ca in the first shock; (⊡) thermodynamic state in the vicinity of the BCC–SC equilibrium curve, where the crystal phase was not identified with certainty (see text); (□) estimates for the thermodynamic states in the SC phase; and (●) thermodynamic state of Ca melt in the first shock wave.

can state with certainty that the calcium temperature resistivity coefficient (TRC) $\sigma = (1/\rho)(\partial\rho/\partial T) = A/\rho$ at $T \approx 1000$ K is an order of magnitude lower than at normal conditions. This fact is not at all surprising. The matter is that, contrary to the majority of other simple metals, the TRC of alkaline-earth metals in the molten state is close to zero or is even negative [25]. Consider-

Resistivity $\rho(P, T)$ of various calcium phases at high pressures P and temperatures T

Ca phase	ρ, 10^{-5} Ω cm ($\pm5\%$)	P, GPa ($\pm8\%$)	T, K	$1/V$, g/cm³
BCC	1.20	14	810	2.346
	1.45	18	1325	2.476
?	2.17	28	1080	2.821
SC	1.66	36	1165	
	1.78*	41*	1210*	
Melt	1.18	32	1580	3.057

Note: A change in the specific volume V upon the BCC–SC phase transition was not taken into account in the calculation of $\rho(P, T)$ for SC Ca. Asterisked are the values of ρ, P, and T at time t_r corresponding to the onset of a smooth increase in resistivity. The question mark in the first column corresponds to a state in the vicinity of the BCC–SC equilibrium curve, where the crystal phase was not identified with certainty (see text).

ing that, apart from heating, crystal becomes strongly disordered in the shock wave, the low TRC values in the shock-compressed Ca seem to be quite admissible at high temperatures. A small or even negative TRC value at high temperatures is typical of many transition metals in the amorphous or disordered state [26]. Our *ab initio* calculations of the Ca electronic structure at high pressures, as also earlier calculations in [11, 15], suggest that *d* electrons in Ca play an important role in the pressure range studied and that Ca is very close to transition metals in its properties.

As was pointed out above, the resistance *R* of Ca samples changes nonmomotonically with the buildup of pressure (see oscillograms in Fig. 2a); the jump in pressure in the third shock at the instant t_3 is accompanied by a jumplike decrease rather than increase in *R*. If one assumes that the Ca thermodynamic states in the second and third shocks correspond to the BCC and SC phases, respectively, then it would be highly difficult to explain the jumplike decrease in resistance in the third shock wave. As was already noted, at pressures above the FCC–BCC transition pressure, the metallic properties of Ca in the SC phase are worse than in the BCC phase. However, if one assumes that the Ca thermodynamic state in the second shock also belongs to the SC phase, then the subsequent decrease in resistance in the third shock can be explained in a simple and natural way. As was pointed out above, the metallic properties of Ca in the SC phase improve with the buildup of pressure, so that the resistance in the third shock wave should decrease. Considering the uncertainties in the calculated temperatures and the experimental errors in measuring pressure and determining the BCC–SC phase boundary, one can believe that this may indeed be the case.

The experimental *R*(*t*) profiles of the second type are presented in Fig. 2b. These profiles are characterized by a monotonic pressure dependence of the resistance. Calculations show that the Ca thermodynamic state behind the front of the first shock wave corresponds to a calcium melt. The value of resistivity ρ obtained at time t_1 for the Ca melt in the first shock wave is given in the table together with the calculated temperature. The melt thermodynamic state is indicated in Fig. 3 by the black circle. The calculations of the calcium thermodynamic states in the second and subsequent shock waves were not carried out for the case shown in Fig. 2b.

The unusual thermal properties of the calcium melt are noteworthy. One can see in Fig. 1 that its Hugoniot adiabat (line *5*) lies to the right of the BCC adiabat (line *3*). This is evidence that the Ca specific volume decreases upon melting in the shock wave. This experimental fact correlates with the negative slope of the calculated equilibrium curve *3* in Fig. 3. The negative curve signifies that the calcium melt in this range of pressures and temperatures is more dense than the Ca crystal.

Note also that, according to our calculations, a jumplike increase in the adiabat slope at $u \approx 3–4$ km/s (Fig. 1) is due to a kink appearing in the adiabat upon its intersection with the equilibrium and melting curves (curves *2*, *3* in Fig. 3, respectively) rather than to the electronic transition, as was assumed in [16, 17].

Let us now comment the common property of the resistance profiles of calcium samples. One can see in Fig. 2 that, in the region of maximal pressures beginning at t_r, the *R*(*t*) profiles of both types contain a section with a smooth increase in *R*. It is worth noting that this increase occurs at a constant pressure *P*(*t*). Consequently, starting at t_r, the resistance of the Ca sample depends not only on pressure but also on time.

In summary, the resistivities of the calcium BCC and SC structures at pressures of 10–40 GPa and temperatures of 800–1400 K and the resistivity of the calcium melt at a pressure of 32 GPa and a temperature of 1580 K have been measured in this work. In the pressure range 10–30 GPa, the portions of equilibrium curves between the Ca BCC and SC phases and between the melt and the BCC phase have been calculated. The shape of Ca Hugoniot adiabat has been revealed in the region of its intersection with the equilibrium curves obtained for three phases. It has been found that the specific volume of calcium decreases upon melting in the shock wave.

The Ca resistivity ρ(*T*, *P*) has been estimated as a function of temperature and pressure in the pressure and temperature ranges 15–40 GPa and 800–1400 K, respectively. It has been shown that the temperature resistivity coefficient is much smaller than its value at normal conditions. The observed small (down to negative) values of this coefficient in the shock-compressed calcium is treated as the result of shock-induced defect formation and crystal disordering.

It is worth noting that the stability region of the FCC phase proved to be inaccessible to the step shock-loading technique used in this work. To explore this region, the amplitudes of the sequential shock waves should be reduced by several times or a quasi-isentropic compression without shock waves should be used. In this case, the region of calcium semiconducting state in the FCC structure can be attained due to a comparatively low quasi-isentropic compression temperature.

REFERENCES

1. T. N. Kolobyanina, Usp. Fiz. Nauk **172**, 1361 (2002) [Phys. Usp. **45**, 1203 (2002)].
2. K. Syassen, in *Proceedings of International School of Physics "Enrico Fermi" on High Pressure Phenomena, Varenna, Italy, 2001*, Ed. by L. Ulivi *et al.* (IOS Press, Amsterdam, 2002), Vol. 147.
3. J. B. Neaton and N. W. Ashcroft, Nature **400**, 141 (1999).
4. M. Hanfland, K. Syassen, N. E. Christensen, and D. L. Novikov, Nature **408**, 174 (2000).
5. V. E. Fortov, V. V. Yakushev, K. L. Kagan, *et al.*, Pis'ma Zh. Éksp. Teor. Fiz. **70**, 620 (1999) [JETP Lett. **70**, 628 (1999)].
6. V. E. Fortov, V. V. Yakushev, K. L. Kagan, *et al.*, J. Phys.: Condens. Matter **14**, 10809 (2002).
7. V. I. Postnov, S. S. Nabatov, A. A. Shcherban', *et al.*, Zh. Tekh. Fiz. **57**, 1181 (1987) [Sov. Phys. Tech. Phys. **32**, 694 (1987)].
8. V. I. Postnov, V. V. Yakushev, T. I. Yakusheva, *et al.*, in *Abstracts of XVII International Conference on Equations of State of Substance* (Elbrus, 2002), p. 50.
9. A. Jayaraman, W. Klement, J. Kennedy, *et al.*, Phys. Rev. **132**, 1620 (1963).
10. B. Vasvari and V. Heine, Philos. Mag. **15**, 731 (1967).
11. H. L. Skriver, Phys. Rev. Lett. **49**, 1768 (1982).
12. R. A. Stager and H. G. Drickamer, Phys. Rev. **131**, 2524 (1963).
13. K. J. Dunn and F. P. Bundy, Phys. Rev. B **24**, 1643 (1981).
14. H. Olijnyk and W. B. Holzapfel, Phys. Lett. A **100**, 191 (1984); N. Winzenick and W. B. Holzaphel, in *High Pressure Science and Technology*, Ed. by W. Trzecia-kowski (World Sci., Singapore, 1996).
15. R. Ahuja, O. Eriksson, J. M. Wills, and B. Johansson, Phys. Rev. Lett. **75**, 3473 (1995).
16. L. V. Al'tshuler, A. A. Bakanova, and I. P. Dudoladov, Pis'ma Zh. Éksp. Teor. Fiz. **3**, 483 (1966) [JETP Lett. **3**, 315 (1966)]; A. A. Bakanova and I. P. Dudoladov, Pis'ma Zh. Éksp. Teor. Fiz. **5**, 322 (1967) [JETP Lett. **5**, 265 (1967)].
17. L. V. Al'tshuler, A. A. Bakanova, and I. P. Dudoladov, Zh. Éksp. Teor. Fiz. **53**, 1967 (1967) [Sov. Phys. JETP **26**, 1115 (1968)].
18. S. S. Nabatov, A. N. Dremin, V. I. Postnov, *et al.*, Pis'ma Zh. Éksp. Teor. Fiz. **29**, 407 (1979) [JETP Lett. **29**, 369 (1979)].
19. V. I. Postnov, A. N. Dremin, S. S. Nabatov, *et al.*, Fiz. Goreniya Vzryva **19**, 160 (1983).
20. P. Blaha, K. Schwarz, G. K. H. Madsen, *et al.*, *WIEN2k. An Augmented Plane Wave + Local Orbitals Program for Calculating Crystal Properties* (Univ. of Technology, Vienna, 2001).
21. A. M. Molodets, Fiz. Goreniya Vzryva **34**, 94 (1998).
22. A. M. Molodets, M. A. Molodets, and S. S. Nabatov, Khim. Fiz. **18**, 67 (1999).
23. *LASL Shock Hugoniot Data*, Ed. by S. P. Marsh (Univ. of California Press, Berkeley, 1980).
24. D. Errandonea, R. Boehler, and M. Ross, Phys. Rev. B **65**, 012108 (2002).
25. A. R. Regel' and V. M. Glazov, *Physical Properties of Electronic Melts* (Nauka, Moscow, 1980), p. 296.
26. J. H. Mooij, Phys. Status Solidi A **17**, 521 (1973).

Translated by V. Sakun

Thermodynamically Stable Fractal-Like Domain Structures in Magnetic Films

F. V. Lisovskiĭ*, L. I. Lukashenko, and E. G. Mansvetova

Institute of Radio Engineering and Electronics, Russian Academy of Sciences (Fryazino Branch),
pl. Vvedenskogo 1, Fryazino, Moscow region, 141120 Russia
*e-mail: lisf@dataforce.net
Received March 4, 2004

A fractal-like structure of the domain boundaries was revealed in "overcritical" uniaxial Permalloy magnetic films. The fractal dimension of domain boundaries at the film surfaces was determined as a function of the film thickness. It is shown that the phase transition between the two possible types of fractal-like structures is accompanied by a jump in fractal dimension. © *2004 MAIK "Nauka/Interperiodica".*

PACS numbers: 75.70.Kw

In various fields of modern science and technology (mathematics, physics, radiophysics, astronomy, acoustics, chemistry, biology, computer engineering, radar, etc. [1–7]), an approach based on the use of the notion of fractals is finding increasing application in the study and modeling of various processes and phenomena. Fractals are hierarchically organized self-similar topological sets with the fractional dimension D_f defined as

$$D_f = \lim_{\epsilon \to 0} \frac{\log N_\epsilon}{\log(1/\epsilon)},\qquad(1)$$

where N_ϵ is the minimal number of hypercubes with edge length ϵ that are necessary for the fractal set to be completely covered. Although the priority of initiating this approach is unconditionally given to mathematicians [8], it is not undeniably so: the idea of the fractal nature of the critical state in condensed media was proposed almost simultaneously and independently by physicists [9] and subsequently has become the starting point for developing the renormalization group method [10]. This unjustice has arisen because one may make no mention of fractals in the practical use of the renormalization group theory.[1]

For good reasons, the experimental evidence for the fractal nature of critical fluctuations has an exclusively indirect character. Meanwhile, there are fractal objects in magnetism that are more accessible for observation and study. For instance, the familiar labyrinth domain structures (DSs) with multiple side laterals at the domain boundaries (DBs) in uniaxial magnetic films with a large positive anisotropy constant $K_u \gg 2\pi M^2$ (M is the saturation magnetization) and easy magnetic axis

oriented along the normal **n** to the surface (henceforth z axis) are the direct material analogues of the Peano–Gosper "winding snakes" [11]. An even more glowing example of the fractal objects is provided by the domain structures observed in the films with $K_u \leq 2\pi M^2$ (Fig. 1) that are discussed below.

Permalloy films (83% Ni, 17% Fe) of thickness L ranging from 1 to 170 μm were prepared by vacuum deposition (10^{-4} torr) on a polished duralumin substrate and studied. The uniaxial anisotropy constant K_u and the saturation magnetization M in the films were 5×10^4 erg/cm^3 and 800 G, respectively; i.e., the ratio $K_u/2\pi M^2$ was equal to 0.0124. The DS was visualized by the Akulov–Bitter method using a magnetic suspension prepared by the Elmor recipe.[2]
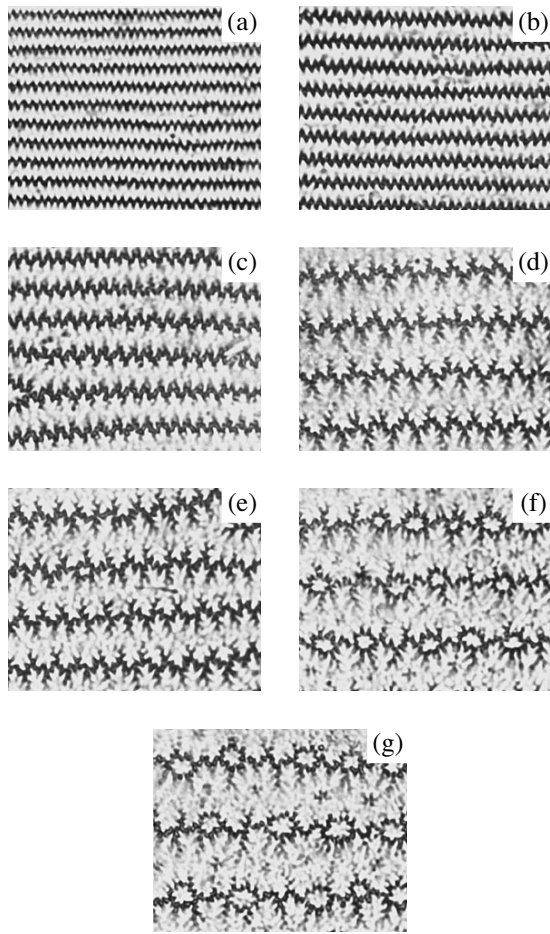
The photographs in Fig. 1 illustrate the DS evolution in the Permalloy films as their thickness increases from (a) 20 to (g) 170 μm. In thin films ($L < 3$ μm), simple (monoperiodic) stripe DSs (the corresponding photographs are not given) with the period d are present; at $L > 3$ μm, near-surface zigzag distortions with the period Λ appear in the DB profile; i.e., the structures become biperiodic (Fig. 1a). As the thickness increases, the amplitude of zigzag distortions increases, and the DB branching starts at $L > 50$ μm via the sequential splitting of zigzag tips or via the formation of laterals.[3] This process evolves in the interval of thicknesses from 50 to 130 μm (Figs. 1b–1e). Near the upper boundary of this interval (Fig. 1e), the contour of each serration

---

[1] The relation between the renormalization group theory and the fractal geometry becomes evident when the state diagrams of magnets are represented in the complex plane; see, e.g., the section "Magnetism and Complex Boundaries" in [4].

[2] For a detailed description of the film growth method and the procedures for measuring the film magnetic parameters and thickness, see [12].

[3] The black and white areas in Fig. 1 corresponding to the domains with $M_z > 0$ and $M_z < 0$, respectively, are asymmetric (with asymmetry of the Asher type). The appearance of an outward excursion at the boundary of black domain implies that an inward excursion appears at the boundary of white domain.
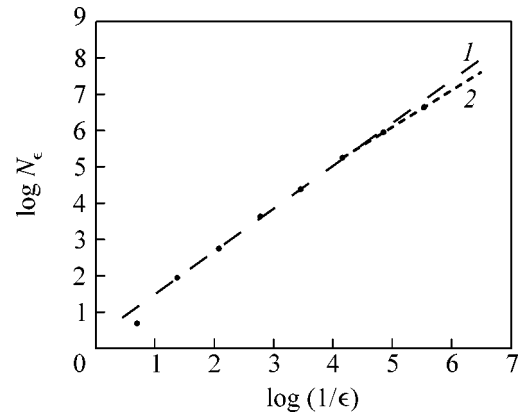
Fig. 1. Evolution of the domain structure in Permalloy films upon an increase in their thickness from (a) 20 to (g) 170 μm.

Fig. 2. Log–log plot of the number N_ϵ of squares covering the fractal domain boundary vs. their reciprocal side length $1/\epsilon$. (•) Experimental values; (dashed line) linear approximation for a truncated set of points; (dotted line) linear approximation for the points satisfying the condition $\epsilon < \min\{R_{\min}, t_{\min}\}$.

resembles the shape of an individual ray of Mandelbrot's square snow flake [1, 11] having the fractal dimension $D_f = 1.5$. In thicker films ($L > 130$ μm), the DB topology qualitatively changes as a result of the formation of the chains of oval DBs corresponding to the isolated near-surface cone-shaped domains penetrating into the film bulk at a depth not exceeding $L/2$ and having an M_z component with sign opposite to the band domains inside which these cones are situated (Figs. 1f, 1g).

The fractal dimension of the DBs at the film surface was determined as follows. At first, the "analog" DS photographs were digitized with a spatial resolution that provided the fulfillment of the condition $a \ll \min\{R_{\min}, t_{\min}\}$, where a is the pixel linear size, $R_{\min}$ is the minimal radius of the DB curvature, and $t_{\min}$ is the minimal domain width at the surface. Then, using the standard application program, the contours were detected according to the mean level of black, to obtain the domain boundary image corresponding to $M_z = 0$ at the film surface. Next, the boundary was covered (within the unit cell of a biperiodic DS of size $d \times \Lambda$) by squares with the edge length ϵ decreasing as 2^{-n}, where

n is the coverage number. Since the DBs are a real (physical) fractal with a finite number of hierarchy levels, the fractal dimension can be determined only after the linear approximation of the experimentally found dependence $\log N_\epsilon = f(\log(1/\epsilon))$ to use, instead of Eq. (1), the following relation [1]:

$$D_f = \frac{\log N_\epsilon^* - C}{\log(1/\epsilon)}, \tag{2}$$

where C is a constant depending on the choice of the unit of measurement ϵ and N_ϵ^* is the value of the approximating linear function at the point corresponding to the value of ϵ used for covering. It follows from Eq. (2) that the fractal dimension is equal to the slope of the straight line approximating the function $N_\epsilon = f(1/\epsilon)$ in the log–log coordinates.

The typical log–log plot of the experimental dependence $N_\epsilon = f(1/\epsilon)$ is presented in Fig. 2 for a film of thickness ≈ 80 μm (points). An analysis of the analogous dependences for all the studied films showed that, to obtain the adequate DB fractal dimension, one should use the linear approximation for a truncated data set (dashed line in Fig. 2). The deviation from the linearity at small $1/\epsilon$ values (large-square covering) is caused by the deviation of a large-scale distortions of the DB profile from self-similarity (Fig. 1); when covering with too small squares, the condition $\epsilon < \min\{R_{\min}, t_{\min}\}$ starts to be met at a rather small ϵ_{cr} value, as a result of which the number of covering squares for $\epsilon < \epsilon_{cr}$ increases inversely proportional to ϵ, and the slope of the curve approximating the set of these experimental points becomes equal to unity (line *2* in Fig. 2).

The fractal dimensions D_f of the domain boundaries at the surfaces of films of various thickness are shown in Fig. 3, where the abscissa is the Λ/d ratio rather than the thickness L. This was done because the local mea-
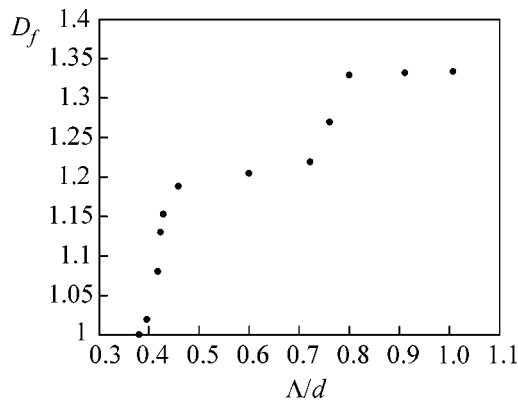
Fig. 3. The dependence of fractal dimension D_f of domain boundaries at film surface on the Λ/d ratio.

surement of L cannot be made with a sufficiently high accuracy, whereas the value of Λ/d can be determined with assurance for any film area from the photographs. In this case, there is also no need to measure the absolute values of the DS periods Λ and d. The Λ/d ratio increases monotonically with increasing film thickness; the extreme left point in Fig. 3 corresponds to a thickness of 50 μm, and the extreme right point corresponds to 170 μm.

It follows from Fig. 3 that the fractal dimension at the initial stage of DB branching increases rapidly with increasing film thickness, after which it becomes saturated at the level $D_f \simeq 1.2$. The appearance of the ring domain boundaries at $\Lambda/d > 0.75$ is accompanied by a drastic increase in the fractal dimension to a value of $\simeq 1.35$, which almost does not change afterwards. The jump in the fractal dimension is caused by a change in the fractal topology and observed in the interval of film thicknesses where a phase transition with doubling of the period Λ occurs between two DS types (cf. Figs. 1e and 1f).

The results of our study testify that DSs in thick films of uniaxial magnets are fractal-like objects whose dimension increases monotonically with an increase in thickness. The domain boundaries at the film surfaces are plane fractals, whereas the domains themselves are three-dimensional fractal objects. At the film center ($z = 0$), the domains have plane-parallel boundaries. They branch as the surfaces $z = \pm L/2$ are approached, as a result of which the domains acquire a tree-like structure. The lines $M_z = 0$ in the $z = \pm l/2$ planes, where $l < L$, have the same structure as the DBs at the surfaces of a film with thickness l.

A unique feature of the observed DSs is that they, first, are thermodynamically stable, i.e., correspond to the ground state of a magnet, and, second, appear in a homogeneous defect-free medium. Such structures were observed not only in Permalloy but also in other metallic (e.g., cobalt) films, as well as in single-crystal films and massive single crystals of magnetoplumbite, barium ferrite, ferrite garnets, and ferrite spinels (see, e.g., [13] and the bibliography cited therein). This dis-

tinguishes the DSs described above from the fractal-like structures formed in amorphous or granulated magnetic films in nonstationary magnetic fields [14–18].

Another unique feature of the aforementioned inhomogeneous distributions of magnetic moments is that they represent biperiodic fractal-like structures that are close to the ideal geometric fractals but exist in real material media.

The statement about the fractal nature of branched domain structures was earlier formulated in [19].

REFERENCES

1. B. B. Mandelbrot, *The Fractal Geometry of Nature* (Freeman, New York, 1982).
2. *Fractals in Physics*, Ed. by L. Pietronero and E. Tozatti (North-Holland, Amsterdam, 1985; Mir, Moscow, 1988).
3. A. Bunde and S. Halvin, *Fractals in Science* (Springer, Berlin, 1995).
4. H.-O. Peitgen and P. H. Richter, *The Beauty of Fractals: Images of Complex Dynamical Systems* (Springer, Berlin; Mir, Moscow, 1993).
5. A. I. Olemskoĭ and A. Ya. Flat, Usp. Fiz. Nauk **163** (12), 1 (1993) [Phys. Usp. **36**, 1087 (1993)].
6. V. V. Zosimov and L. M. Lyamshev, Usp. Fiz. Nauk **165**, 361 (1995) [Phys. Usp. **38**, 347 (1995)].
7. A. A. Potapov, *Fractals in Radiophysics and Radiolocation* (Logos, Moscow, 2002).
8. B. B. Mandelbrot, Science **155**, 636 (1967).
9. L. P. Kadanoff, Physics (Long Island City, N.Y.) **2**, 263 (1966).
10. K. G. Wilson, Phys. Rev. B **4**, 3174 (1971); Phys. Rev. B **4**, 3184 (1971).
11. M. Gardner, *Penrose Tiles to Trapdoor Cipher* (Freeman, New York, 1989; Mir, Moscow, 1993).
12. L. S. Palatnik, L. I. Lukashenko, Yu. V. Zolotnitskiĭ, and B. A. Avramenko, Zh. Éksp. Teor. Fiz. **59**, 1177 (1970) [Sov. Phys. JETP **32**, 643 (1970)].
13. F. V. Lisovskiĭ, E. G. Mansvetova, and Ch. M. Pak, Zh. Éksp. Teor. Fiz. **111**, 283 (1997) [JETP **84**, 156 (1997)].
14. B. E. Bernacki and M. Mansuripur, J. Appl. Phys. **69**, 4960 (1991).
15. G. V. Sayko, A. K. Zvezdin, T. G. Pokhil, *et al.*, IEEE Trans. Magn. **28**, 2931 (1992).
16. A. Kirilyuk, J. Ferre, and D. Renard, Europhys. Lett. **24**, 403 (1993).
17. V. G. Kleparskiĭ, N. I. Karmatskiĭ, and M. Kiselevskiĭ, in *Proceedings of XVII International School–Seminar on New Magnetic Materials of Microelectronic* (URSS, Moscow, 2000), p. 710.
18. T. A. Pisarenko, A. M. Frolov, G. S. Kraĭnova, *et al.*, in *Proceedings of XVIII International School–Seminar on New Magnetic Materials of Microelectronic* (URSS, Moscow, 2002), p. 593.
19. I. E. Dikshteĭn, D. V. Kuznetsov, F. V. Lisovskiĭ, and E. G. Mansvetova, in *Proceedings of XVI International School–Seminar on New Magnetic Materials of Microelectronic* (URSS, Moscow, 1998), Part 2, p. 510.

Translated by V. Sakun

Diagrammar and Metamorphosis of Coset Symmetries in Dimensionally Reduced Type IIB Supergravity¶

A. J. Nurmagambetov

Akhiezer Institute for Theoretical Physics, National Scientific Center, Kharkov Institute of Physics and Technology, Kharkov, 61108 Ukraine
e-mail: ajn@kipt.kharkov.ua
Received March 2, 2004

Studying the reduction of type IIB supergravity from ten to three spacetime dimensions, we describe the metamorphosis of the Dynkin diagram for gravity line "caterpillar" into a type IIB supergravity "dragonfly" that is triggered by the inclusion of scalars and antisymmetric tensor fields. The final diagram corresponds to type IIB string theory E_8 global symmetry group, which is the subgroup of the conjectured E_{11} hidden symmetry group. Application of the results for getting the type IIA/IIB T-duality rules and for searching for type IIB vacua solutions is considered. © *2004 MAIK "Nauka/Interperiodica".*

PACS numbers: 04.65.+e; 04.50.+h; 11.25.Mj

One of the problems which has been actively studied lately is to identify the underlying superstring/M-theory symmetry group [1–3]. Knowing the group is the essential step in passing from higher energies and dimensions to phenomenologically relevant vacua of M theory and is the bypass for bringing to light the hidden but essential ingredients of higher-dimensional theory that might help uncover its true nonperturbative structure. The evidence on the possible group-theoretical ground of M theory comes from studying the coset symmetries in dimensionally reduced $D = 11$ supergravity as the M-theory low-energy limit. It was realized long ago [4] that the global symmetry groups of $D = 11$ supergravity toroidally compactified down to four spacetime dimensions fall into the class of exceptional groups E_n with $n \leq 7$. Subsequent reduction of $D = 11$ supergravity to three- [5] and to two-dimensional [6] spacetimes (see also [7]) revealed E_8 and E_9 global symmetry structure. The role of E_{10} as the hidden symmetry group of $D = 11$ supergravity compactified onto a ten-dimensional torus was emphasized in [8], and this conjecture was proved in [7].

The important step in relating the global symmetry groups of toroidally reduced $D = 11$ supergravity to the true but hidden symmetry group of the theory in eleven dimensions was done made [9]. There, the exceptional geometry of $D = 3$ maximal supergravity that made it possible to reformulate $D = 11$ supergravity in an E_8 invariant way was discovered. Together with the previously obtained results of [10, 11], this observation gave strong evidence in favor of searching for the exceptional geometry of M theory based on a symmetry group which will contain as a subgroup the E_n sequence

of global low-dimensional symmetries with $n \leq 10$. Following previous experience, it could be naively expected to have, after "compactifying" the time, a hidden symmetry group whose algebra is of rank eleven and includes E_9 and E_{10} as subalgebras. Since E_{10} is the hyperbolic Kac–Moody algebra [12] which contains E_8 and its affine extension $E_9 \sim E_8^+$ as subalgebras and is called the overextension of E_8, i.e., $E_{10} \sim E_8^{++}$, an M-theory hidden symmetry group should also be an extension of hyperbolic Kac–Moody algebras. Such a generalization studied in [2, 13–15] has been christened the "very extension" of E_8 or $E_{11} \sim E_8^{+++}$ (see also [16, 17]).

The relevance of E_{11} to the nonlinear realization of supergravities has been demonstrated for the bosonic subsectors of higher-dimensional maximal supergravities [1, 18]. A curious result is that the global hidden symmetry group of type IIB theory turns out to be the same as for M&A theories related to each other by dimensional reduction. Since the type IIB theory is not related to M theory via straightforward dimensional reduction on a circle, the validity of E_{11} as the type IIB theory global symmetry group can be established in studying the coset structure of dimensionally reduced type IIB supergravity. Substantial fragments of this structure were found in [14, 19–22].

The aim of the present paper is to re-collect the fragments in a systematic way during the application of the "antioxidation" strategy of [23] and to emphasize the points that were omitted from previous considerations. We start with the ten-dimensional theory, compactifying it to three spacetime dimensions. The special role of three-dimensional spacetime in establishing the hidden symmetries of higher-dimensional supergravities has

---

¶ This article was submitted by the author in English.

been emphasized for a long time, since there is no gravity degrees of freedom in $D = 3$ and, dualizing gauge fields, we get a theory whose dynamics is completely determined by scalar degrees of freedom. Depending on the original higher-dimensional subsectors of fields, the scalars parametrize different G/H coset spaces. Identifying the global group G for different subsectors of type IIB supergravity is our main task.

Let us begin our quest of the hidden symmetry group of type IIB superstring theory with the following action describing dynamics of the bosonic subsector of fields entering the type IIB supergravity multiplet

$$S = \int_{\mathcal{M}^{10}} \left[R * \mathbf{1} + \frac{1}{2} d\phi_0 * d\phi_0 + \frac{1}{2} e^{2\phi_0} d\chi_0 * d\chi_0 \right.$$

$$\left. -\frac{1}{2} e^{-\phi_0} H^{(3)} * H^{(3)} - \frac{1}{2} e^{\phi_0} \tilde{H}^{(3)} * \tilde{H}^{(3)} + \frac{1}{4} \tilde{H}^{(5)} * \tilde{H}^{(5)} \right. \quad (1)$$

$$\left. + \frac{1}{2} A^{(4)} dB^{(2)} dA^{(2)} + \mathcal{L}_{PST} \right].$$

The first term of (1) corresponds to the Einstein–Hilbert term, $\int_{\mathcal{M}^{10}} * \mathbf{1} \equiv \int d^{10} x \sqrt{-g}$, and ϕ_0 and χ_0 are the dilaton and axion scalars. $H^{(3)}$ and $\tilde{H}^{(3)}$ are the field strengths of NS and RR gauge fields $B^{(2)}$ and $A^{(2)}$:

$$H^{(3)} = dB^{(2)}, \quad \tilde{H}^{(3)} = dA^{(2)} - H^{(3)} \chi_0. \quad (2)$$

As well as the scalars, they cast the doublet under $SL(2, R)$ global symmetry group of type IIB theory. $\tilde{H}^{(5)}$ is the self-dual field strength of the $SL(2, R)$ singlet RR field $A^{(4)}$:

$$\tilde{H}^{(5)} = dA^{(4)} - H^{(3)} A^{(2)}, \quad \tilde{H}^{(5)} = *\tilde{H}^{(5)}. \quad (3)$$

The last term, which is not important for the discussion in what follows, encodes the self-duality condition [24, 25]. Since we have made the choice of differential form notation, the wedge product between forms has to be assumed.

The first step in completing our task is to recover the following structure of action:

$$S = \int_{\mathcal{M}^3} \left[\frac{1}{2} d\phi * d\phi + \frac{1}{2} \sum_{\alpha} e^{\alpha \cdot \phi} d\chi_\alpha * d\chi_\alpha \right] + \dots, \quad (4)$$

which is obtained from (1) after performing dimensional reduction on T^7. Here, $\phi = (\phi_0, \phi_1, \dots, \phi_7)$ is the dilaton vector comprised of the original dilaton ϕ_0 and those appeared during dimensional reduction. The α are constant eight-vectors which label additional (axionic) scalar fields χ_α. The difference between two types of scalars consists in sources of their appearance due to dimensional reduction and the different types of interactions they possess [26]. The axions come from

the nondiagonal part of the Kaluza–Klein metric and from dualizing the higher-rank tensor fields. They possess only derivative interactions. On the contrary, the scalars associated with dilatons come from the diagonal part of the metric and can have nonderivative interactions as in (4). The form of action (4) is a sign that the scalars parametrize a G/H coset space if, of course, one can identify the axion counting vectors as positive roots of a group G. The global symmetry group G is uniquely defined by the Cartan matrix constructed out of the simple roots [26].

To reach action (4), we will use the same strategy as in [23]. To this end, one has to take into account the standard rules of step-by-step toroidal reduction [27]:

$$\int d^D xeR \longrightarrow \int d^{D-1} xeR + \int_{\mathcal{M}^{D-1}} \left[\frac{1}{2} d\phi_1 * d\phi_1 \right.$$

$$\left. + \frac{1}{2} e^{-2(D-2)\alpha_{D-1}\phi_1} F_1^{(2)} * F_1^{(2)} \right] \quad (5)$$

with

$$\sqrt{2(D-2)(D-3)} \alpha_{D-1} = 1, \quad (6)$$

and

$$\int_{\mathcal{M}^D} \frac{1}{2} F^{(n)} * F^{(n)}$$

$$\longrightarrow \int_{\mathcal{M}^{D-1}} \left[\frac{1}{2} e^{-2(n-1)\alpha_{D-1}\phi_1} F_1^{(n)} * F_1^{(n)} \right. \quad (7)$$

$$\left. + \frac{1}{2} e^{2(D-1-n)\alpha_{D-1}\phi_1} F_1^{(n-1)} * F_1^{(n-1)} \right].$$

The effects of transgression consisting in the appearance of new terms in the reduced field strength $F_1^{(n)} = dA_1^{(n-1)} + \dots$ and of having the Chern–Simons term in type IIB supergravity action are denoted by the ellipsis in (4) and may be safely ignored [23], since they do not influence the results in what follows.

Let us get started with the pure gravity case. Performing the reduction in step-by-step manner, one can recover six seven-dimensional simple root vectors α_k having the following structure [23]:

$$\alpha_k$$
$$= (0, \dots, 0, -2(8-k)\alpha_{9-k}, 2(6-k)\alpha_{8-k}, 0, \dots, 0) \quad (8)$$

with α's from (6), $k = 0, \ldots, 5$ zeroes on the left and $(5 - k)$ zeroes on the right. It is easy to verify that

$$\boldsymbol{\alpha}_i \cdot \boldsymbol{\alpha}_k = \begin{cases} 4, & i = k \\ -2, & |i - k| = 1 \\ 0, & |i - k| \geq 2. \end{cases} \quad (9)$$

All other roots coming from this subsector of type IIB supergravity are not simple and can be expressed as a linear combination of simple roots with nonnegative coefficients.

One more simple root vector comes from dualizing the Kaluza–Klein vector field which appeared in the first step of reduction from ten to three and has the following form:

$$\boldsymbol{\delta} = (16\alpha_9, 2\alpha_s, 2\alpha_7, \ldots, 2\alpha_3). \quad (10)$$

One can check that

$$\boldsymbol{\delta} \cdot \boldsymbol{\alpha}_k = \begin{cases} 0, & k \neq 0 \\ -2, & k = 0, \end{cases} \quad \boldsymbol{\delta} \cdot \boldsymbol{\delta} = 4, \quad (11)$$

and other roots that come from dualizing the rest of the Kaluza–Klein vectors are not simple. Denoting $\boldsymbol{\delta}$ as $\boldsymbol{\alpha}_{(0)}$, one can construct the Cartan matrix

$$A_{ij} = 2 \frac{\boldsymbol{\alpha}_i \cdot \boldsymbol{\alpha}_j}{\boldsymbol{\alpha}_i \cdot \boldsymbol{\alpha}_i}, \quad i = (0), 0, \ldots, 5 \quad (12)$$

which corresponds to the A_7 Dynkin diagram. This diagram is that of the $SL(8)$ group and is called the gravity line.

Let us extend our analysis to include the dilaton–axion sector of type IIB supergravity. Since we have ϕ_0 from the beginning, we shall extend our simple root vectors (8), (10) with one additional column with zero on the left, i.e.,

$$\boldsymbol{\alpha}_{(0)} = (0, 16\alpha_9, 2\alpha_8, 2\alpha_7, \ldots, 2\alpha_3),$$

etc. Hence, we should deal with eight-dimensional simple root vectors. And since we have axion χ_0 from the beginning, we have also one additional eight-dimensional root vector

$$\boldsymbol{\epsilon} = (2, 0, \ldots, 0). \quad (13)$$

Clearly,

$$\boldsymbol{\epsilon} \cdot \boldsymbol{\epsilon} = 4, \quad \boldsymbol{\epsilon} \cdot \boldsymbol{\alpha}_k = 0, \quad \forall k. \quad (14)$$

The Cartan matrix extended by the new root corresponds to the following Dynkin diagram that encodes the $SL(8) \otimes SL(2, R)$ group structure of this sector of fields of type IIB supergravity. In the language of Dynkin diagrams, the first node on the right corresponds to the $SL(2, R)$ group.

The next step is to extend our system of roots with the inclusion of $H^{(3)}$ and $\tilde{H}^{(3)}$ tensor fields. One more
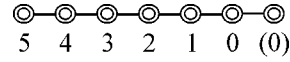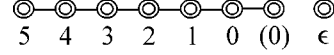
Fig. 1. Gravity line "caterpillar" of A_7.
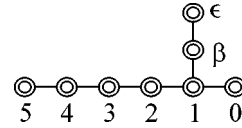

Fig. 2. Beginning of the "caterpillar's" metamorphosis.

Fig. 3. End of metamorphosis. "Dragonfly" is fully fledged.

simple root comes from the reduction of the NS field kinetic term [23]:

$$\boldsymbol{\beta} = (-1, 12\alpha_9, 12\alpha_s, 0, \ldots, 0). \quad (15)$$

It is easy to check that

$$\boldsymbol{\beta} \cdot \boldsymbol{\alpha}_k = \begin{cases} 0, & k \neq 1 \\ -2, & k = 1 \\ +2, & k = (0), \end{cases} \quad (16)$$

$$\boldsymbol{\beta} \cdot \boldsymbol{\beta} = 4, \quad \boldsymbol{\beta} \cdot \boldsymbol{\epsilon} = -2.$$

As such, the root $\boldsymbol{\alpha}_{(0)}$ is not simple anymore, since the off-diagonal entries of the Cartan matrix are negative integers or zero. It is merely a technical point to establish the absence of other simple roots which could possibly come from the dualization of the NS 2-form gauge field and the rest of the fields of type IIB multiplet and their dualization. Therefore, at this stage of our study, we arrive at the following diagram.

This diagram is topologically equivalent to the E_8 Dynkin diagram, and, therefore, the latter is the global symmetry group of type IIB theory compactified to three spacetime dimensions.

Let us turn now to applying the results obtained so far. We will describe first the interpretation of T-duality rules in the language of Dynkin diagrams (see also [14, 21]). Doing the calculations outlined above, one arrives at the following diagram that encodes the coset structure of type IIA supergravity reduced to three spacetime dimensions. Here, we have chosen a slightly different notation to indicate the tensor fields from which the simple roots came.
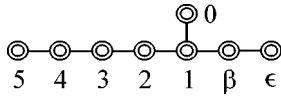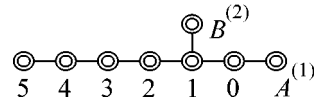
Fig. 4. Type IIB E_8-like diagram.
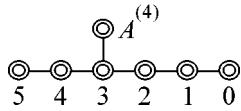

Fig. 5. Type IIA E_8 diagram.

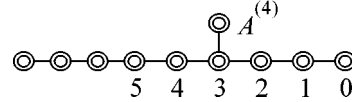

Fig. 6. Type IIB E_7 diagram.

Fig. 7. E_7^{+++} diagram.

Comparing Fig. 5 to Fig. 4, one can observe that two diagrams coincide along the gravity line from nodes 1 to 5. This is just an indication of having the same gravity subsector for two theories in the $D = 9$ spacetime dimension. To have the same theories in $D = 9$, we have to identify the node corresponding to type IIA NS 2-form $B^{(2)}$ with that of the type IIB gravity node, the type IIA gravity node with the node of type IIB NS 2-form field, and the one of the type IIA Kaluza–Klein vector field with that of the type IIB axion. This identification corresponds to seminal T-duality rules (cf., e.g., [28]):

$$i_z B_{IIA}^{(2)} \cong (i_Z g)_{IIB}, \quad (i_z g)_{IIA} \cong i_Z B_{IIB}^{(2)}, \quad i_z A^{(1)} \cong \chi_0. \quad (17)$$

Another important point in playing with Dynkin diagrams is the possibility of identifying the relevant $AdS \times S$ vacuum configurations [22]. A couple of years ago, it was a breakthrough in constructing the consistent nonlinear Kaluza–Klein ansätze for spherical dimensional reduction of supergravities (see [26, 29] for review). A systematic group-theoretical ground indicating the possibility of such reductions is still lacking, though the criterion of consistency of the reduction on S^n based on the possibility of enhancing the global symmetry group after T^n reduction due to "conspiracy" of scalars was formulated.

An essential step in searching for the nonlinear Kaluza–Klein ansätze for spherical reductions is figuring out the possibility of having the $AdS \times S$ vacuum configuration. Recently, a method of examining such a possibility based on considering the appropriate Kac–Moody algebras was proposed [22]. In the context of type IIB supergravity, the evidence of $AdS_5 \times S^5$ vacuum configuration is based on manipulations with the E_7 diagram extended with three additional nodes on the left, i.e., with the E_7^{+++} diagram (cf. Fig. 7).

The origin of the E_7 is easy to explain since the latter corresponds to a "larva" in the metamorphosis of Fig. 1 to Fig. 3. Such a diagram comes from the subsector of fields consisting of gravity and the self-dual 4-form gauge field. It is worth mentioning that the root $\boldsymbol{\xi}$ com-

ing from the reduction of $\tilde{H}^{(5)}$ field strength and the one coming from its dualization obey the following relations:

$$\boldsymbol{\xi} \cdot \boldsymbol{\alpha}_k = \begin{cases} 0, & k \neq 3 \\ -2, & k = 3 \\ +2, & k = (0), \end{cases} \qquad \tilde{\boldsymbol{\xi}} \cdot \boldsymbol{\alpha}_k = \begin{cases} 0, & k \neq 3 \\ -2, & k = 3 \\ +2, & k = (0), \end{cases} \quad (18)$$

$$\boldsymbol{\xi} \cdot \boldsymbol{\xi} = 4, \quad \tilde{\boldsymbol{\xi}} \cdot \tilde{\boldsymbol{\xi}} = 4, \quad \boldsymbol{\xi} \cdot \tilde{\boldsymbol{\xi}} = 4.$$

Hence, it is a matter of taste which one is selected to be the simple root that is the remnant of the $\tilde{H}^{(5)}$ self-duality. As soon as the choice is made, the other root is no longer simple.

Skipping the details of manipulations with the E_7^{+++} diagram that lead to the $AdS_5 \times S^5$ configuration (we refer the reader to the original paper [22]), it is worth mentioning that the subset of fields leading to the E_7^{+++} is precisely the one for which the existence of the nonlinear ansätze for the S^5 dimensional reduction [30] was proved! Another example of having the nonlinear ansätze for $AdS_{D-3} \times S^3$ and $AdS_3 \times S^{D-3}$ configurations was established for the bosonic string theory [31] which includes a graviton, dilaton, and 2-rank gauge field in the massless sector. This subsector enters the type IIB supergravity and corresponds to the D_8^{+++} Kac–Moody group. One can verify following the approach of [22] that such vacuum solutions are indeed the case.

To summarize, we have traced the metamorphosis of Dynkin diagrams representing the symmetries of different subsectors of dimensionally reduced type IIB supergravity. This provides a link to the results obtained in the framework of nonlinear realization of type IIB supergravity [18] and of searching for the M-theory hidden symmetry group [1–3, 14, 15], as well as to the results obtained by use of the oxidizing technique [20, 21]. The graphical representation of the coset symme-

tries in dimensionally reduced supergravities encodes a lot of information on the matter field content of a theory, the relevant low-dimensional vacua, and dualities between different supergravities and is, therefore, a very useful tool in studying the hidden symmetry structure of superstring/M theory.

REFERENCES

1. P. C. West, Class. Quantum Grav. **18**, 4443 (2001).
2. P. C. West, Class. Quantum Grav. **20**, 2393 (2003).
3. F. Englert, L. Houart, A. Taormina, and P. C. West, J. High Energy Phys. **09**, 020 (2003).
4. E. Cremmer and B. Julia, Nucl. Phys. B **159**, 141 (1979).
5. N. Marcus and J. H. Schwarz, Nucl. Phys. B **228**, 145 (1983).
6. H. Nicolai, Phys. Lett. B **194**, 402 (1987).
7. S. Mizoguchi, Nucl. Phys. B **528**, 238 (1998).
8. B. Julia, in *Proceedings of AMS–SIAM Summer Seminar on Application of Group Theory in Physics and Mathematics* (Chicago, 1982).
9. K. Koepsell, H. Nicolai, and H. Samtleben, Class. Quantum Grav. **17**, 3689 (2000).
10. B. de Wit and H. Nicolai, Nucl. Phys. B **274**, 363 (1986).
11. B. Drabant, M. Tox, and H. Nicolai, Class. Quantum Grav. **6**, 255 (1989).
12. R. W. Gebert and H. Nicolai, hep-th/9411188.
13. M. R. Gaberdiel, D. I. Olive, and P. C. West, Nucl. Phys. B **645**, 403 (2002).
14. A. Kleinschmidt, I. Schnakenburg, and P. West, hep-th/0309198.
15. A. Kleinschmidt, hep-th/0304246.
16. H. Nicolai and D. I. Olive, Lett. Math. Phys. **58**, 141 (2001).
17. H. Nicolai and T. Fischbacher, hep-th/0301017.
18. I. Schnakenburg and P. C. West, Phys. Lett. B **517**, 137 (2001).
19. E. Cremmer, B. Julia, H. Lü, and C. N. Pope, Nucl. Phys. B **535**, 242 (1998).
20. E. Cremmer, B. Julia, H. Lü, and C. N. Pope, hep-th/9909099; Nucl. Phys. B **535**, 73 (1998).
21. A. Keurentjes, Nucl. Phys. B **658**, 303 (2003).
22. I. Schnakenburg and A. Miemiec, hep-th/0312096.
23. N. D. Lambert and P. C. West, Nucl. Phys. B **615**, 117 (2001).
24. G. Dall'Agata, K. Lechner, and D. P. Sorokin, Class. Quantum Grav. **14**, L195 (1997).
25. G. Dall'Agata, K. Lechner, and M. Tonin, J. High Energy Phys. **9807**, 017 (1998).
26. C. N. Pope, http://faculty.physics.tamu.edu/pope/.
27. H. Lü, C. N. Pope, E. Sezgin, and K. S. Stelle, Nucl. Phys. B **456**, 669 (1995).
28. E. Eyras, B. Janssen, and Y. Lozano, Nucl. Phys. B **531**, 275 (1998).
29. M. Cvetič, G. W. Gibbons, H. Lü, and C. N. Pope, Class. Quantum Grav. **20**, 5161 (2003).
30. M. Cvetič, H. Lü, C. N. Pope, *et al.*, Nucl. Phys. B **586**, 275 (2000).
31. M. Cvetič, H. Lü, and C. N. Pope, Phys. Rev. D **62**, 064028 (2000).